Towards High Precision Mass Measurements of Short-Lived Exotic Isotopes Using Highly Charged Ions at the TITAN Penning Trap System.

by

Maxime Brodeur,

B.Sc., L'Université de Montréal, 2004

A THESIS SUBMITTED IN PARTIAL FULFILMENT OF
THE REQUIREMENTS FOR THE DEGREE OF

Master of Science

in

The Faculty of Graduate Studies

(Physics)

The University Of British Columbia

April 21, 2006

Abstract

The TRIUMF's Ion Trap for Atomic and Nuclear science (TITAN) experiment will use Penning trap (PT) for precise mass determinations on short-lived isotopes at ISAC. An Electron Beam Ion Trap (EBIT) is used to charge breed ions to a charge state q. The PT mass resolution is directly proportional to q, resulting in a significant increase in the achieved precision. This PT system will allow very accurate mass determination, via time-of-flight (TOF) measurements, on the order of $\delta m/m \approx 10^{-8}$ on isotopes with a half-lives of about 50 ms using highly charged ions (HCI). This thesis presents work on TITAN's PT design, as well as studies carried out at other PT experiments.

Since after the EBIT a beam of HCIs needs to be efficiently transferred into and out of the PT, additional complications arise, therefore, ion flight simulations of the injection and the extraction of ions from the PT were performed. Simulations have determined the optimal ion optics to minimize the diameter of the ion bunch entering the PT. Simulations of TITAN's Lorentz steerer, the first one for HCIs, have shown it is possible to inject the sample, such that additional preparation in the PT become obsolete. This reduces the required time and presents an important improvement for operation with short-lived species. TOF simulations to optimize the extraction geometry for HCI and singly charged ions were carried out. The resulting geometry for injection, PT structure, and extraction has been designed and is under construction.

In addition, two complementary projects were made on existing PT experiments. First, a magnetic field stability study of ISOLTRAP's PT has found a magnetic field-temperature correlation and a day-night temperature variation inside the magnet bore. This presents an important determination of a source of systematic uncertainty similar to what TITAN will have. Finally, a reference laser ablation ion source for the Canadian Penning trap experiment has been designed and is presented.

Maxime Brodeur. brodeur@physics.ubc.ca

Contents

List of Tables

List of Figures

Acknowledgements

There are several persons who support and helped me during my Master's thesis project. First, I want to express my gratitude to my supervisor J. Dilling for picking me as one of its graduate student and giving me the chance to learn more about other Penning trap experiments. My stays at the ISOLTRAP and CPT experiments were scientifically and culturally fruitful. Next comes V. Ryjkov who's help and guidance was determinant during my research. Thank for your patience and numerous advices. I want to thank M. Smith for its inputs and making my thesis readable. Many thanks also to R. Baartman, L. Blomeley, M. Good, J. Vaz and the numerous persons who participated in the TITAN experiment.

There are several persons I would like to thank at ISOLTRAP. Specially K. Blaum who gave me a fantastic short-term project and A. Herlert for its help and advices while I was writing and debugging my program. I also want to thank A. Kellerbauer, C. Yazidjian and the rest the ISOLTRAP experiment.

Many persons helped me during my stay at CPT specially, G. Savard who's patience and guidance were appreciated. My ion source would be non-existing without the advices of A. Levand and the hands of the "conductor" S. Cladwell. Thank J. Fallis for letting me crash at your place. Many thanks to J. Clark, S. Gulick, N. Scielzo, H. Sharma, I. Tanihata and Y. Wang for their help and inputs.

Finally, I would like to thank l'Union des Batisseurs de Condo (UBC) for providing such a great learning environment. Merci papa et maman pour toujours avoir cru en moi et pour votre presence malgres la distance. Merci aussi a Cédric, mon commentateur sportif préféré, pour me tenir au courant des deboires de la Sainte Flanelle. Thanks to my girlfriend Yung Ting for her support, innumerable encouragements and being my sun in the rainy days.

There once was a brainy baboon,
Who always breathed down a bassoon,
For he said, "It appears
That in billions of years
I shall certainly hit on a tune".
—Arthur Eddington. New Pathways in Science (Cambridge 1939)

Part I

Thesis

Chapter 1

Introduction

Since the beginning of the twentieth century, detailed atomic mass studies have had an important impact in all fields of physics. For example, in 1920 F.W. Aston [Ast20] discovered the "mass defect": while nuclei, like helium, have an integral masses (4.000 u), some like hydrogen, present non-integral mass values (1.008 u). The mass defect is the difference between the number of nuclei and the atomic mass in units of atomic mass u. In 1920, Sir Arthur Eddington interpreted the 0.008 u "mass defect" of hydrogen in term of a "binding energy" that is released when four hydrogen atoms form helium. This was the first suggestion that the sun obtain its energy from fusion reaction. Nowadays, an accurate determination of atomic masses is more than ever of high importance. Penning traps, which will be introduced in this thesis, represent the state-of-the art in high precision and accuracy mass spectrometry.

1.1 Motivation of this Thesis

The TRIUMF's Ion Trap for Atomic and Nuclear science (TITAN) [Dil03] at the TRI-University Meson Facility (TRIUMF) in Vancouver is dedicated to high accuracy mass measurement of unstable highly charge ions, by means of Penning trap mass spectrometry. Penning traps have been proven to be the most accurate devices for mass determination. The atomic mass is determined in those traps by measuring the cyclotron frequency ν_c of the ion in a magnetic field and employing

$$\nu_c = \frac{1}{2\pi}\frac{q}{m}B, \tag{1.1}$$

where q/m is the charge-to-mass ratio of the trapped ion and B the magnetic field strength. Since ions are measured the missing electrons and the binding energy have to be added. TITAN, shown in Figure 1.1, will be the first experiment for on-line produced ions that will use an Electron Beam Ion Trap (EBIT) to charge boost the ions from singly charged (A^{1+}) to highly charged (A^{n+}) and load them into the Penning trap. This novel approach allows mass measurements with relative accuracy of $\delta m/m \approx 10^{-8}$ on short-lived isotopes with half-lives of only $\sim$50 ms. When dealing with short-lived on-line produced ions, efficiency is of paramount importance. The production of the ions is often very difficult, and experiments are only possible when the ions can be transported with high efficiency to the measurement apparatus, hence the Penning trap. In this thesis, a study of mass spectrometry experiments using Penning

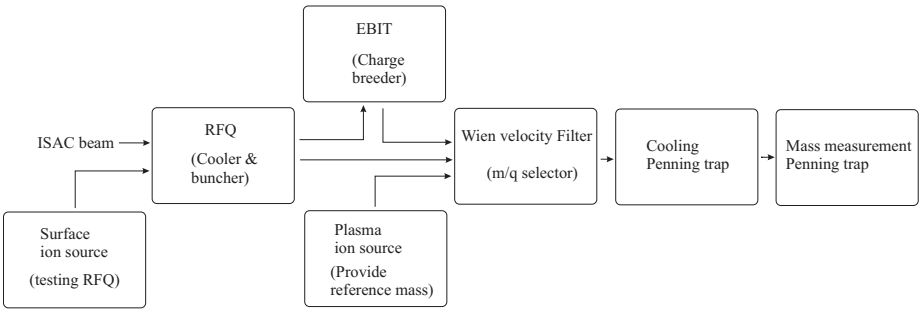

Figure 1.1: Block diagram of the TITAN experiment. See Section 2.1 for a detail explication of the different components.

trap is presented. First, the importance of ion optics is shown with simulations of the injection-extraction from TITAN's precision Penning trap. In addition, the design of Canadian Penning trap (CPT) calibration laser ablation ion source involved different ion optics devices in order to efficiently transfer the produced ion into the CPT beam line. Moreover, a study of the correlation between the variation of the magnetic field as function of the magnet bore temperature of ISOLTRAP's precision Penning trap shows the importance of systematic studies.

The thesis outline is: the first chapter gives the motivations for carrying out high accuracy mass spectrometry and shows the different mass measurement techniques. The basics principle of a Penning trap is explained together with the time-of-flight mass measurement technique. Also, an overview of the different existing Penning trap experiments is given. The second chapter explains the TITAN experimental set-up and in particular focuses on simulations of the injection and extraction optics of the TITAN mass measurement Penning trap. The third chapter reports on two projects done at existing Penning trap experiment: first, a study of magnetic field stability for the ISOLTRAP precision Penning trap and secondly a design of a calibration laser ablation ion source for the Canadian Penning Trap (CPT) experiment.

1.2 Motivation for High Accuracy Mass Spectrometry

High accuracy mass spectrometry experiments are versatile and have motivations stemming from several fields of physics. Examples include:

- Nuclear physics: Shell closure effects, existence and locations of magic numbers far from the valley of stability and binding energies for systematic studies for super-heavy nuclei.

- Particle physics: Unitary of the CKM matrix.

In the following, the examples are explained in more detail, and the relevance of mass measurements is put into context.

1.2.1 Shell closure effects

By adding a spin-orbit coupling term to the Hamiltonian of the Shell Model Mayer, Haxel, Jensen and Suess [May49, Hax49] managed to explain the existence of the so-called magic numbers. A magic number corresponds to the cumulative number of nucleons-filled energy states at the end of a shell. In this model, a shell corresponds to a group of states with similar energies compared to the energy of other shells. Each shell is separated by an energy gap called "shell gap". The shell gaps have a very large effect on the binding energy of the nucleus. The nuclear binding energy $B(N,Z)$ of a nucleus with N neutrons and Z protons, is a quantity that can be directly determined from mass measurements:

$$B(N,Z) = (Nm_n + Zm_p - M(N,Z))c^2, \tag{1.2}$$

where m_n is the neutron's mass, m_p is the proton's mass and $M(N,Z)$ is the nuclear mass. The effect of shell gaps on the nuclear binding energy can be seen by plotting the two-neutrons separation energy S_{2n}, which is defined as,

$$S_{2n}(N,Z) = B(N,Z) - B(N-2,Z). \tag{1.3}$$

Figure 1.2 shows two interesting features. First, the shell gap appear as a rapid decrease in S_{2n} after the magic number $N = 50$. Secondly, there is another sudden decrease in S_{2n} for the nucleus with $Z = 37$ to 44 between $N = 56$ and 61. At this point, the shell structure looses its spherical shape and becomes deformed causing an abrupt decrease in the nuclear binding energy of the nucleus.

In order to clearly observe effects such as shell gap or shell deformation, one needs to know the mass of the involved nuclei with a certain precision. For instance, the binding energy per nucleon for nuclei with an atomic mass of $A \sim 100$ is about $B_E/A \sim 5$ MeV. Therefore, in order to see shell gaps, the required resolution on the measured mass has to be $\delta m/m = 10^{-5}$.

1.2.2 Test of the unitary of the CKM matrix

The Standard Model (SM) of particle physics, which describes the interactions of elementary particles, is currently tested by many experiments. One of the tests of the Standard Model is the verification of the unitarity of the Cabibbo-Kobayashi-Maskawa (CKM) matrix [Cab63, Kob73]. The CKM matrix couples the quark's strong and weak eigenstates:

$$\begin{pmatrix} |d_w\rangle \\ |s_w\rangle \\ |b_w\rangle \end{pmatrix} = \begin{pmatrix} V_{ud} & V_{us} & V_{ub} \\ V_{cd} & V_{cs} & V_{cb} \\ V_{td} & V_{ts} & V_{tb} \end{pmatrix} \begin{pmatrix} |d_s\rangle \\ |s_s\rangle \\ |b_s\rangle \end{pmatrix}$$

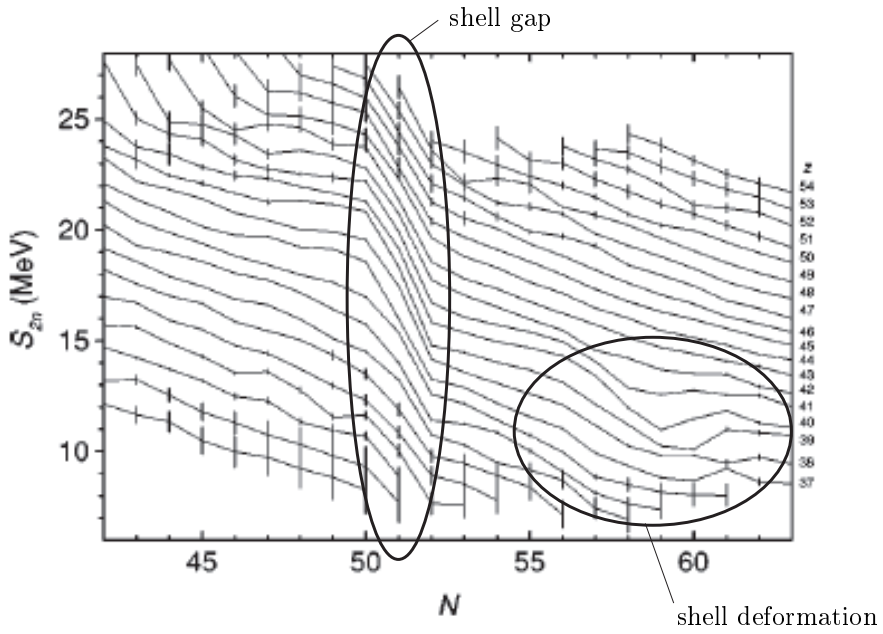

Figure 1.2: Two-neutron separation energies for nuclei close to the magic number N = 50. Note the decrease in S_{2n} due to shell gap and shell deformation (from [Lun03]).

The square of each V_{ij} term represents a probability of transition of a quark state under the weak interaction, for example V_{ud} is the probability of a u-quark mixed into a d-quark. Under SM assumptions, this implies that the CKM matrix would be unitary:

$$\sum_i V_{ui}^2 = V_{ud}^2 + V_{us}^2 + V_{ub}^2 = 1. \tag{1.4}$$

From the last compilation of all available experimental data, including all theoretical corrections, the unitary of the CKM matrix fails to meet unitary by about 2.4σ [Har05]:

$$\sum_i V_{ui}^2 = 0.9966 \pm 0.0014. \tag{1.5}$$

Measuring the V_{us} and V_{ub} terms is strictly in the domain of experimental particle physics, but since the V_{ud} term only involves quarks of the first generation, its value is experimentally accessible through nuclear physics experiments. V_{ud} can be determined from the measurement of the ft-values of super-allowed $0^+ \rightarrow 0^+$ β-decay. The ft-value, or "comparative half-life" is given by the product of the half-life of the decay with the phase-space factor f. A more physically

relevant quantity is the Ft-value that includes the nucleus-dependant radiative correction δ_R and isospin symmetry breaking correction δ_c:

$$Ft = ft(1 + \delta_R)(1 - \delta_c) \tag{1.6}$$

The experimental part of the Ft-value comes from the half-life $T_{1/2}$, the branching ratio R and most important, the Q-value of the $0^+ \rightarrow 0^+$ transitions [Har05]. The Q-value of a nuclear reaction is given by the difference of mass between the reactant and the product:

$$Q = m(reactant) - m(product). \tag{1.7}$$

The CVC hypothesis says that the vector current, i.e. the $W^{\pm}$ and Z^0 bosons, in the weak interaction is conserved. So these particles don't interact with the electro-magnetism nor strong fields, which are both spinor fields. A consequence of this is that all $0^+ \rightarrow 0^+$ decays have the same Ft-value. The correctness of the Conserved Vector Current (CVC) hypothesis can be verified and the value of V_{ud} is calculated from the average $\overline{Ft}$-value:

$$V_{ud}^2 = \frac{K}{2G_F^2(1 + \Delta_R^v)\overline{Ft}}, \tag{1.8}$$

where G_F is the Fermi constant, Δ_R^v is a transition independent radiative correction, K is a numerical constant and the average $\overline{Ft}$-value is taken from 12 well-known $0^+ \rightarrow 0^+$ transitions. The importance of high accuracy mass measurements comes from the calculation of the statistical rate function f, which is dependent on the Q-value of the transitions to the fifth power [Pre62]. Therefore, the direct mass measurements which lead to a precise determination of Q-values, play an important role in the determination of V_{ud}.

In 2005, after measuring the Q-value for the super-allowed $0^+ \rightarrow 0^+$ emitter ^{46}V [Sav05a], the Canadian Penning Trap (CPT) experiment found a 2.19 keV difference between their results and the last compilation of all available experimental data corresponding to a 5σ deviation. After further investigation, they discovered a set of seven measurements [Von77] which measured Q-values were off by 2-5σ from the rest of the compilation data (see Figure 1.3). After removing the inconsistent data, the new value of V_{ud} became: 0.9745(16), which brings the CKM matrix closer to unitary:

$$V_{ud}^2 + V_{us}^2 + V_{ub}^2 = 0.9985(12) \tag{1.9}$$

compared to the previous result of 0.9966(14).

The uncertainty level on the determination of V_{ud}^2 and $\overline{Ft}$ is about 10^{-3}. Since $Ft \propto Q^5$, the required uncertainty on the Q-value is $< 2 \times 10^{-4}$ [Har05]. Therefore, since the Q-value of the 12 best-known $0^+ \rightarrow 0^+$ β-transition are about a few MeV, the required accuracy on the mass measurement of nuclei with masses $A \sim 35$ is: $\delta m/m \approx 10^{-8}$ and as it will be shown in Section 1.3.2, only Penning trap experiments can achieve such accuracy.

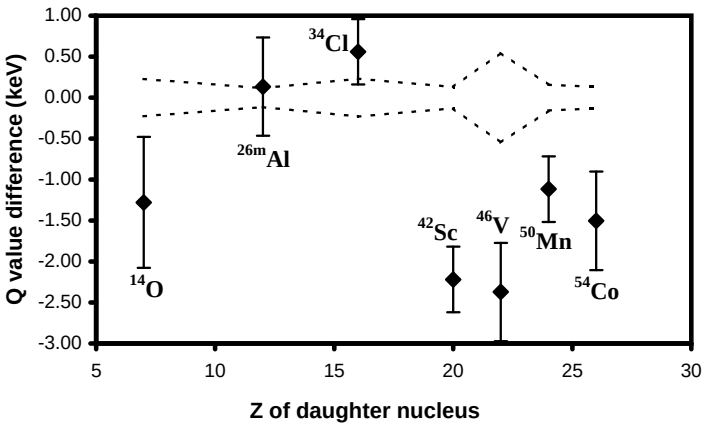

Figure 1.3: Q-value difference between [Von77] and the weighted average of all other data. The doted line represents the uncertainty (from [Sav05a]).

1.3 Comparison of existing mass measurement techniques

The two physical applications of mass spectrometry discussed in the previous section involve the use of radioactive isotopes. Interesting shell structure effects such as shell deformation, are characteristics of unstable nuclei with low binding energy. Thus, there is an important need to couple high accuracy mass measurement experiments with installations that produce radioactive nuclei.

1.3.1 Production and Separation of short-lived radioactive isotopes

The way an experiment is setup for precision mass measurement on short-lived radioisotopes greatly depends on the method by which the nuclei are produced. In general, the exotic nuclei are produced by the interaction of a primary beam with a target. There are two ways to produce and separate the desirable species: the on-line and in-flight method.

The Isotope Separation On-Line (ISOL) technique

In the ISOL method the exotic nuclei are created by spallation, fragmentation and fission reaction of the primary beam within a thick target (for ex. [Dom02]). The atoms diffuse out of the target, and are consequently ionized via various methods, such as resonant laser ionization, surface or plasma ionization. Then, the beam is accelerated up to 60 keV and mass-separated using a magnetic dipole. ISOL facilities around the world include: ISOLDE [Kug00] at CERN

in Swisserland, IGISOL [Pen97] in Finland and ISAC [Dom02] at TRIUMF in Canada. The ISAC facility is described in more detail in Chapter 2.

The In-flight technique

With the In-flight technique, the exotic nuclei are produced by collision of a primary beam with a thin target. Since the exotic nuclei are produced in the beam, a separation of the desirable species from the primary beam follows in flight, hence the name. General methods for this include the use of velocity and magnetic rigidity filters. Experiments using in-flight techniques are for example, presently at: GSI in Germany, GANIL in France, at the NSCL facility at MSU and at the Argonne National Laboratory (ANL), both in the USA. A specific example of an in-flight set-up is describe in Chapter 3.

1.3.2 Direct mass measurement techniques

This section will describe some of the most common mass measurement techniques. Conventional mass spectrometry, which involves deflection of an ion beam with a homogenous magnetic field for momentum analysis on rare isotopes, is no longer carried out. The final experimental program of this kind ended with the closure of the TASCC facility at Chalk-River (Canada) in 1996. Mass measurement techniques can be grouped into three groups that will be presented in this section: time-of-flight spectroscopy, storage ring mass measurement and cyclotron frequency measurements.

Time-of-flight technique

In the Time-Of-Flight (TOF) technique, the mass of the radioactive ion is determine by a precise measurement TOF of the ions through a magnetic field and its magnetic rigidity $B\rho$:

$$B\rho = \frac{\gamma m v}{q} \tag{1.10}$$

where γ is the Lorentz factor, m the mass, q the charge and v the speed of the ion. The speed is determined from the TOF of the ion and a known flight path length. TOF spectrometers exist in two different types: linear and circular. Linear TOF spectrometer like SPEG at GANIL [Sav05c] can achieve mass measurement of ion far away from the valley of stability, but have high relative uncertainty in the order of $\delta m/m \sim 10^{-5}$. On the other side, the CSS2 experiment also in GANIL [Lal01], uses a cyclotron to decrease the relative uncertainty ($\delta m/m$) in the mass measurement. By undergoing circular motion instead of linear, the ions can travel a longer path, which leads to a larger TOF and therefore a smaller relative uncertainty. Note that even with its higher uncertainty, SPEG still plays an important role in mass measurement, as being a sensitive experiment that can measure the mass of nuclei that are very far from stability.

Storage ring mass measurement

The Experimental Storage Ring (ESR) at GSI [Gei01] is an other type of multi-turn time-of-flight (TOF) mass measurement. The mass is measured from the frequency of revolution of the ions. The relative uncertainty $\delta m/m$ depends on the frequency resolution as well as the velocity $\delta v/v$ spread:

$$\left|\frac{\delta m}{m}\right| = \gamma_t^2 \left|\frac{\delta \nu}{\nu}\right| + (\gamma_t^2 - \gamma^2) \left|\frac{\delta v}{v}\right|, \tag{1.11}$$

where γ is the Lorentz factor $\gamma = (1 - v^2/c^2)^{-1/2}$ and γ_t^2 is the so-called transition point that depends on the optical setting of the storage ring. In order to have a direct relation between the revolution frequency ν and the m/q ratio, the second term in (1.11) needs to be equal to zero. For the ESR experiments two techniques have been developed to achieve this: the Schottky and isochronous mass spectrometry.

In the first technique, the ions are cooled with a dense electron beam, reducing their velocity spread $\delta v/v$. At each turn, the ions induce charges on the plates of the Schottky detector and the frequency ν is deduced by the Fourier transformation of that signal [Rad00].

In the second technique, the ion-optical parameters are set to have $\gamma = \gamma_t$. In this setting, the TOF of the ions with unknown masses is recorded by the interaction of the beam with a thin foil at every turn. The frequency of the unknown mass is given by comparing its TOF spectra with the TOF spectra of an ion of reference [Hau00].

The Schottky technique allows a determination to a precision of about 10 keV of up to 100 masses simultaneously. Due to the time required for the cooling process, this technique is limited to half lives of 1 s. The isochronous technique on the other side, which does not involve any cooling, can do measurements within 500 ns. This technique has a precision of 100 keV, but can measure the mass of very unstable nuclei with half-lives of few microseconds. The difference between the isochronous and Schottky techniques are illustrated in Figure 1.4.

Cyclotron frequency measurement

For these techniques the mass of the ions is extracted from the measurement of the cyclotron frequency of the ions inside a uniform magnetic field and employing:

$$\omega_c = \frac{qB}{m} \tag{1.12}$$

There are two methods for measuring the value of ω_c, by radio-frequency transmission spectrometer, or by using a Penning trap. The choice of which method depends on the required accuracy and the half-life of the ion.

In a radio-frequency transmission spectrometer like MISTRAL [Lun01], a bunched beam is transmitted in the system and undergoes two complete helicoidal turns before being measured by an electron multiplier. In order to make the mass measurement, a radio-frequency excitation is applied half way along

each turn. This modulation either accelerates or decelerates the ion, changing the radius of the trajectory. If the frequency of the rf-excitation is a half-integer of the cyclotron frequency:

$$\omega_{RF} = (n + 1/2)\omega_c \tag{1.13}$$

the effect of the modulation is cancelled after the two turns [Lun01] and the ion recovers its initial orbital radius. At MISTRAL, narrow exit slits (0.4 mm) allow the selection of the ions obeying (1.13). The mass is determined by comparing the obtained cyclotron frequency with a cyclotron frequency of a reference mass. With this technique one can measure the mass of ions with relatively short half-lives since the ions undergo only two rotations at their full injection energy of typically 60 keV. The disadvantage of this technique is the small acceptance of the apparatus due to the narrow slits. This leads to a decrease in sensitivity.

In Penning trap experiments, like ISOLTRAP, the ISOL beam is typically prepared before one can measure the cyclotron frequency accurately. The ion beam needs to be cooled and bunched before entering the Penning trap. Mass spectrometers using Penning traps achieve very high mass measurement accuracy on the order of $\delta m/m \sim 10^{-9}$, but at the cost of having to prepare the ion beam, which takes more time and puts constrains on the minimum half-life of the radioisotopes that one can measure. The difference in the relative uncertainty and relative isobaric distance from stability between radio-frequency transmission spectrometer and Penning trap experiments is shown in Figure 1.4. A detail description of how Penning traps works and an overview of the different existing Penning trap experiments at radioactive beam facilities follows in Section 1.4.

Limitations of the mass measurement techniques

The strengths and limitations of the different experiments discussed in the previous section regarding the relative uncertainty they achieve for different unstable nuclei half-life, is shown in Figure 1.4. The "relative isobaric distance from stability" gives a good indication on the limitations from the half-life and it is defined as the distance at constant atomic mass number (A) between the measured nuclei and a quadratic fit of all β-stable in the (Z, N) chart. This distance is normalized using $10/A^{2/3}$ [Lun03]. Time-of-flight experiments like SPEG for instance, can measure nuclear masses very far from stability compared to Penning trap experiments, but it is at the price of a limited accuracy. When it comes to high accuracy mass spectrometry experiments on unstable nuclei not too far from the valley of stability, i.e. for a half-life limitation of about 100 ms, Penning trap experiments such as ISOLTRAP, with their uncertainty of $\delta m/m = 5 \times 10^{-9}$, are the best choice.

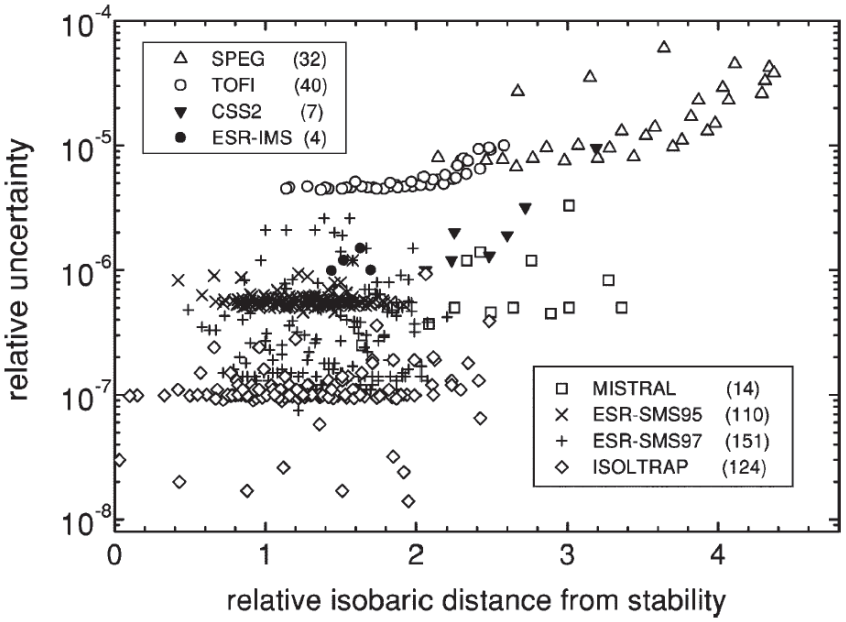

Figure 1.4: Relation between the relative uncertainty $\delta m/m$ on published mass measurements of unstable nuclei and the corresponding relative isobaric distance from stability (from [Lun03]) for: the time-of-flight experiments SPEG, TOF1 and CSS2, the storage ring experiments ESR-IMS/SMS and the cyclotron frequency measurement experiments MISTRAL and ISOLTRAP. In parenthesis is number of measurements made by the experiments until 2003. See text for more details.

1.4 Theoretical description of a Penning Trap

In general, in order to trap a particle in three dimensions, one needs a potential configuration that exerts a force toward the center of the trap:

$$\vec{F} = -e\vec{\nabla}V, \tag{1.14}$$

where a convenient choice of potential, that produces a central force, is a three dimensional potential of the form:

$$V = ax^2 + by^2 + cz^2 \tag{1.15}$$

In order to obey the Laplace equation:

$$\nabla^2 V = 0, \tag{1.16}$$

the sum of the different coefficients in (1.15) must be zero:

$$a + b + c = 0. \tag{1.17}$$

This means that one of the coefficients has to be negative. By having a cylindrical symmetry around the z-axis, one can simplify and set $a = b$, which leads to the condition a = -$c/2$ and:

$$V = c(z^2 - r^2/2), \tag{1.18}$$

where $r = \sqrt{x^2 - y^2}$ is the radial position of the particle. In order to have an equipotential electrode surface, (1.18) must satisfy:

$$V(surface) = c(z^2 - r^2/2) = constant \tag{1.19}$$

This is the equation of two hyperbolas: one pointing along the axial direction and the other along the radial direction as shown in Figure 1.5. The value of constant c can be set from the difference of potential between the two hyperbolas:

$$V_0 = V(z = z_0, r = 0) - V(z = 0, r = r_0) = c(z_0^2 + r_0^2/2) \tag{1.20}$$

$$c = \frac{V_0}{2d_0^2} \tag{1.21}$$

Where $d_0 = \sqrt{z_0^2/2 + r_0^2/4}$ is referred to as the characteristic length of the trap. Therefore, the potential produced by the trap is:

$$V = \frac{V_0}{2d_0^2}(z^2 - r^2/2) \tag{1.22}$$

As shown in Figure 1.6, the problem with such potential, is there is no absolute minimum: the ions are only attracted to the center of the trap along the axial direction. In order to trap the ions in three dimensions, two possible solutions can be employed:

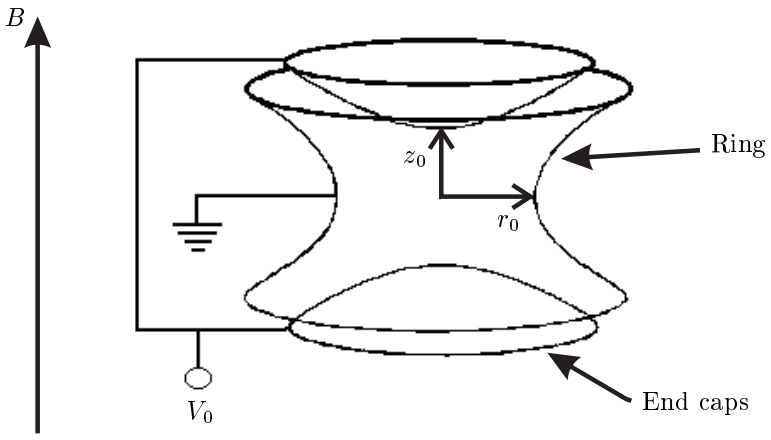

Figure 1.5: Schematic view of the hyperbolic structure of a Penning trap.

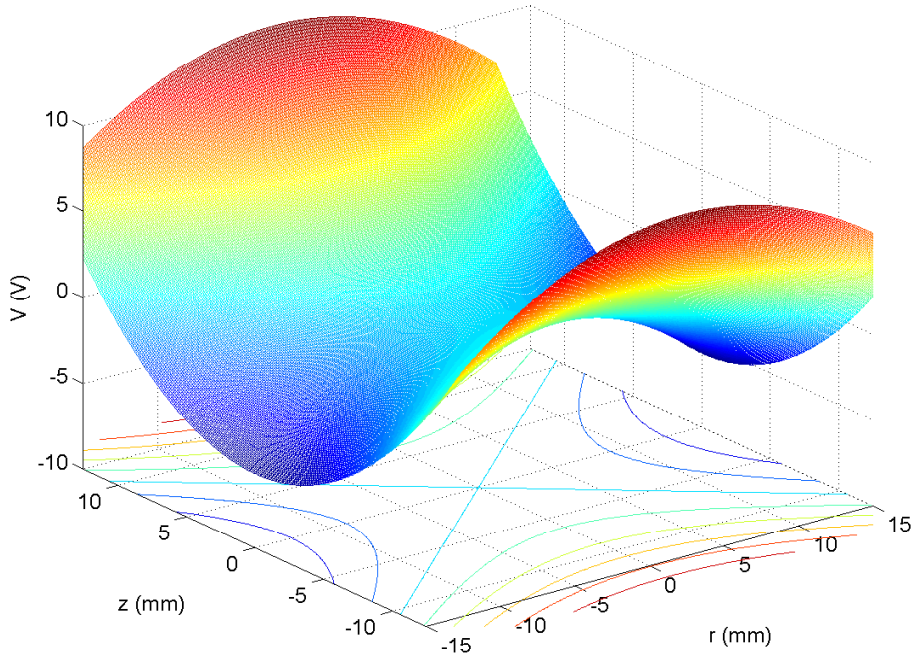

Figure 1.6: Theoretical electric potential of the TITAN mass measurement Penning trap with: $r_0 = 15$ mm, $z_0 = 12.5$ mm, $V_0 = 10$ V.

- Alternating the sign of V_0, so the ions experience an average central force. This is employed in the so-called Paul trap. For a detailed discussion about Paul traps, see for example [Gos95].
- By applying a magnetic field that provides a force to counter the defocusing force from the electrostatic field. This is used in a Penning trap.

In the next section will discuss in detail the motion of an ion in a Penning trap.

1.4.1 Ion motion in a Penning trap

In a Penning trap, the ions are effected by the force produced by the quadrupolar electric field $\vec{E}$:

$$\vec{F_e} = -q\vec{\nabla}V = -\frac{qV_0}{d_0^2}(\vec{z} - \vec{r}/2) \tag{1.23}$$

and the force produced by the homogenous axial magnetic field $\vec{B} = B\hat{z}$:

$$\vec{F_m} = -q\vec{v} \times \vec{B} = -q\dot{\vec{r}} \times B\hat{z} \tag{1.24}$$

The dot indicates temporal partial derivative. Since the magnetic field is along the z-axis, the magnetic component of the Lorentz force does not affect the axial ion motion.

The equations of motion for an ion in the trap are found using Newton's second law:

$$\sum \vec{F} = m\vec{a} = -\frac{qV_0}{d_0^2}(\vec{z} - \vec{r}/2) - qB\dot{\vec{r}} \times \hat{z} \tag{1.25}$$

In cylindrical coordinates, this leads to axial and radial equations of motion:

$$\ddot{z} = -\frac{qV_0}{md_0^2}z \tag{1.26}$$

$$\ddot{\vec{r}} = \frac{qV_0}{2md_0^2}\vec{r} - \frac{qB}{m}\dot{\vec{r}} \times \hat{z} \tag{1.27}$$

The first equation represents an axial harmonic motion of frequency:

$$\omega_z = \sqrt{\frac{qV_0}{md_0^2}}, \tag{1.28}$$

produced by the electric potential V_0. The second equation is more complex, but can be rewritten using the relation of the cyclotron frequency ω_c:

$$\omega_c = \frac{qB}{m} \tag{1.29}$$

$$\ddot{\vec{r}} = \frac{\omega_z^2}{2}\vec{r} + \omega_c\dot{\vec{r}} \times \hat{z}. \tag{1.30}$$

Table 1.1: Typical values for the different frequencies $\nu = \omega/2\pi$ for a particle with $m/q = 2$ inside a Penning trap with $B = 4\text{T}$ and $d_0^2 = 130\ \text{mm}^2$.

ω_z	307 kHz
ω_c	30.7 MHz
ω_+	30.7 MHz
ω_-	1.53 kHz

To solve for the radial motion of the ion, it is convenient to write the equation of motion in cartesian coordinates:

$$\ddot{x} - \omega_c \dot{y} - \frac{\omega_z^2}{2} x = 0 \tag{1.31}$$

$$\ddot{y} + \omega_c \dot{x} - \frac{\omega_z^2}{2} y = 0 \tag{1.32}$$

One can decouple (1.31) and (1.32) using: $u = x + iy$ such that:

$$\ddot{u} = -i\omega_c \dot{u} + \frac{\omega_z^2}{2} u. \tag{1.33}$$

With the ansatz:

$$u \propto e^{-i\omega_\pm t}, \tag{1.34}$$

one finds the eigenfrequencies:

$$\omega_\pm = \frac{\omega_c}{2} \pm \frac{\omega_c}{2}\sqrt{1 - \frac{2\omega_z^2}{\omega_c^2}} \tag{1.35}$$

The $\omega_\pm$ frequencies obey the following relationships:

$$\omega_c = \omega_+ + \omega_- \tag{1.36}$$

$$\omega_c^2 = \omega_+^2 + \omega_-^2 + \omega_z^2 \tag{1.37}$$

$$\frac{\omega_z^2}{2} = \omega_+ \omega_- \tag{1.38}$$

Table 1.1 gives the calculated values of the frequencies for a magnetic field of $B = 4$ T, for a highly charge ion with $m/q = 2$ and with $d_0^2 = 130\ \text{mm}^2$. From this, one observes that $\frac{2\omega_z^2}{\omega_c^2} = 2 \times 10^{-5} \ll 1$, fulfilling the condition for a Taylor expansion of (1.35). This gives:

$$\omega_+ \simeq \omega_c - \frac{\omega_z^2}{2\omega_c} \tag{1.39}$$

$$\omega_- \simeq \frac{\omega_z^2}{2\omega_c} \tag{1.40}$$

The frequency in (1.39) is called the reduced cyclotron frequency and it is a consequence of the repulsive radial electric potential: it reduces the strength of

the centrifugal force and reduces the cyclotron frequency by a small amount ω_- called the magnetron frequency. Before explaining where the magnetron motion comes from, it is important to remember that due to the attractive electric potential along the z-axis, the ion motion will be close to the z-axis, which means that the ion will move in a region in which the electric and magnetic field are mainly perpendicular to each other. Such a field configuration creates a velocity filter that selects only the ions with the velocity:

$$\vec{v} = \frac{\vec{E} \times \vec{B}}{B^2}. \tag{1.41}$$

By inserting the radial component of the electric field into (1.41) and with the use of relations (1.28) and (1.29), one gets:

$$\frac{\vec{v}}{r} = \frac{\omega_z^2}{2\omega_c} \widehat{r} \times \widehat{z} \tag{1.42}$$

This corresponds to a slow precession, of frequency ω_-, around the center of the trap. Together with the fast cyclotron motion, the overall radial ion motion

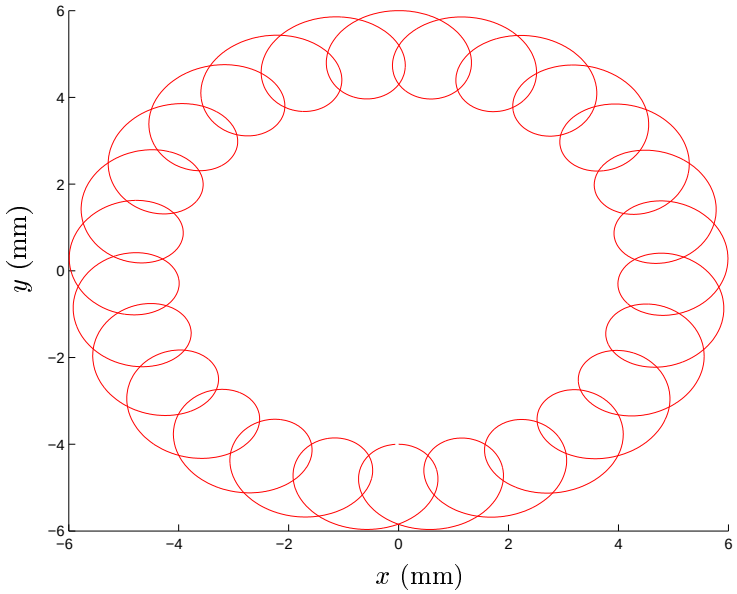

Figure 1.7: Epicycle motion of an ion inside a Penning trap, with parameters: $r_0 = 15$ mm, $z_0 = 12.5$ mm, $V_0 = 200$ V, $m = 74$ u, $q = 1$e, $r_+ = 5$ mm, $r_- = 1$ mm

forms epicycles as shown in Figure 1.7.

The total radial energy of an ion inside a Penning trap is given by the sum of its kinetic and potential energies. The radial potential energy corresponding

to the electric potential (1.22) is given by:

$$E_r^{pot} = -\frac{m}{2}\omega_+\omega_-(r_+^2 + r_-^2), \tag{1.43}$$

while the kinetic energy of the particle is given by the sum of the kinetic energy of the two eigenmotions:

$$E_r^{kin} = \frac{m}{2}\omega_+^2 r_+^2 + \frac{m}{2}\omega_-^2 r_-^2 \tag{1.44}$$

Where r_+ and r_- are the radii of the reduced cyclotron and magnetron motions respectively. Since $\omega_+ \gg \omega_-$, one observes that the energy of the reduced cyclotron motion is mainly kinetic, while the energy of the magnetron motion is mainly potential.

Penning trap experiments make use of relation (1.29) to make mass measurement, but since the cyclotron frequency ω_c is not a normal mode, one needs to couple the two normal modes ω_+ and ω_- via the application of an excitation frequency ω_{rf} in order to extract ω_c. The next section discusses how such mass measurements are achieved with a Penning trap experiment.

1.4.2 Time-of-flight technique

Penning trap mass spectrometry experiments employ an electrode configuration with a central ring electrode, which is segmented into four segments. This allows for the application of dipole and quadrupole radio-frequency (rf) excitation. The dipole excitation is used for the preparation phase when the ion enters the trap. A dipole excitation at frequency ω_- increases the magnetron motion radius of all ions and afterward, a second excitation at the mass dependant frequency ω_+ acts as a isobaric selector. This ensures that only the ions of a certain mass remain and removes all other unwanted species. After the separation phase, a quadrupole excitation of frequency ω_{rf} is applied [Kon95], creating an electric field:

$$\vec{E} = \frac{qV_{rf}}{2a^2}\cos(\omega_{rf} + \phi_{rf})(y\hat{x} + x\hat{y}). \tag{1.45}$$

Where V_{rf} is the amplitude of the voltage at a radial distance a from the axis of the trap and ϕ_{rf} is the phase of the rf-field. Once the quadrupole excitation is applied, the radius of the magnetron and reduced cyclotron motion evolves as [Kon95]:

$$\begin{aligned} r^{\pm}(t) \;=\; & \{r^{\pm}(0)\cos(\omega_B t) \mp \\ & (\frac{r^{\pm}(0)i(\omega_{rf} - \omega_c) + r^{\mp}(0)k_0 e^{\pm i\Delta\phi}}{2\omega_B})\sin(\omega_B t)\}e^{i(\omega_{rf}-\omega_c)t/2} \end{aligned} \tag{1.46}$$

With:

$$\omega_B = \frac{1}{2}\sqrt{(\omega_{rf} - \omega_c)^2 + k_0^2}, \tag{1.47}$$

$$k_0 = \frac{V_{rf}}{2a^2}\frac{q}{m}\frac{1}{\omega_+ - \omega_-}, \tag{1.48}$$

$$\Delta\phi = \phi_{rf} - \phi_+ - \phi_-. \tag{1.49}$$

The case of interest is when $\omega_{rf} = \omega_c$, then:

$$r^{\pm}(t) = \{r^{\pm}(0)\cos(k_0 t/2) \mp r^{\mp}(0)e^{\pm i\Delta\phi}\sin(k_0 t/2)\} \tag{1.50}$$

If the ion starts completely in a magnetron mode of radius $r^{-}(0) = r_0$, then Eq. (1.50) becomes:

$$\frac{r^{+}(t)}{r_0} = \sin(k_0 t/2) \tag{1.51}$$

$$\frac{r^{-}(t)}{r_0} = \cos(k_0 t/2) \tag{1.52}$$

As shown in Figure 1.8, there is a full conversion after an excitation period:

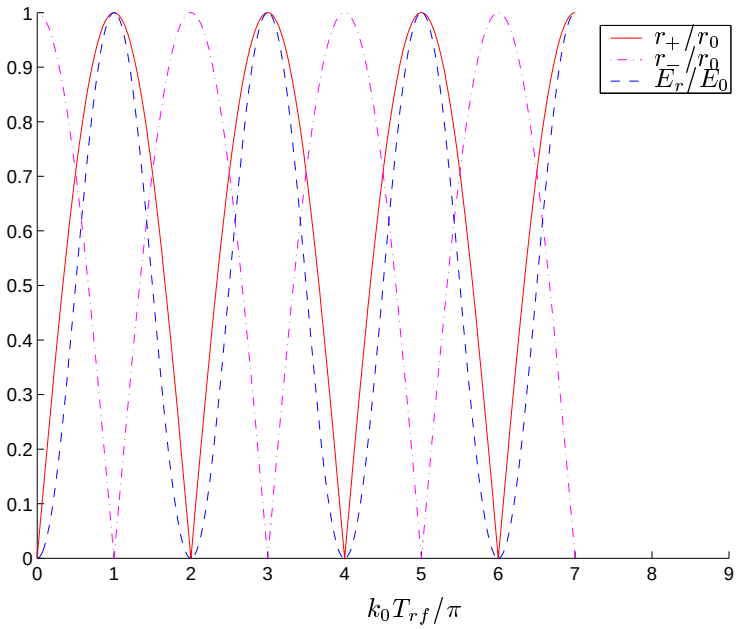

Figure 1.8: Evolution of the reduced cyclotron motion of radius r_+, magnetron motion of radius r_- and radial kinetic energy as a function of the time (given in dimensionless units of T_{rf}).

$$T_{rf} = \pi/k_0 \tag{1.53}$$

According to (1.44), the energy $E_r \propto \omega_+^2 r_+^2$. The radial kinetic energy of the ion is maximized for excitation period of:

$$T_{rf} = (2n-1)\pi/k_0, \tag{1.54}$$

where n is an integer. Therefore, with a quadrupolar rf-excitation of duration T_{rf}, a conversion of the magnetron motion into a pure reduced cyclotron motion is perfomed. The ions then have a radial energy of:

$$E_r = E_0 \frac{\sin^2(\frac{\pi}{2}\sqrt{(2\Delta\nu_{rf}T_{rf})^2+1})}{(2\Delta\nu_{rf}T_{rf})^2+1}, \tag{1.55}$$

where:

$$\Delta\nu_{rf} = \frac{\omega_{rf}-\omega_c}{2\pi}. \tag{1.56}$$

Figure 1.9 shows that the ions which are resonantly excited have maximum

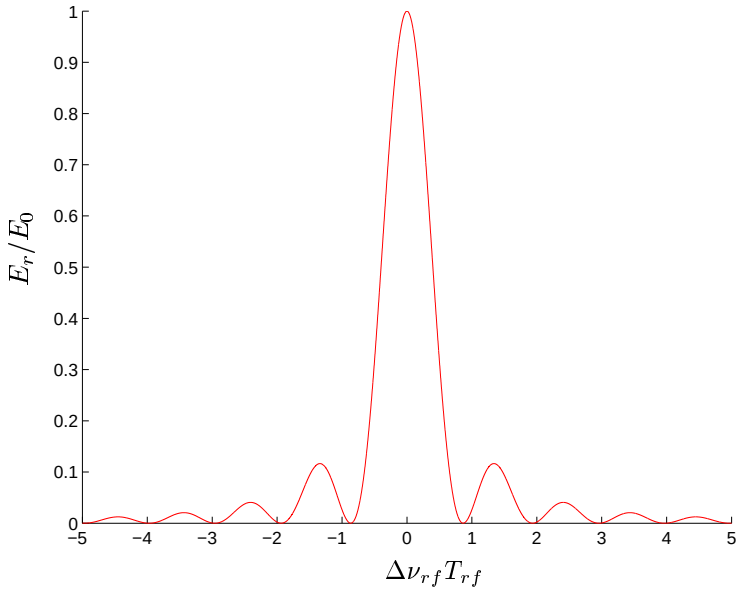

Figure 1.9: Radial kinetic energy as a function of the excitation frequency ν_{rf}.

radial energy after the conversion. After the quadrupolar excitation, the ions are ejected axially from the trap.

In the uniform magnetic field inside the trap, the ions have a magnetic moment:

$$\vec{\mu}(\omega_{rf}) = \frac{E_r(\omega_{rf})}{B}\hat{z} \tag{1.57}$$

As they approach the detector, the magnetic moment of the ions interacts with the magnetic field gradient of the fringe field (shown in Figure 1.10) and the ions experience an axial force:

$$\vec{F} = -\vec{\nabla}(\vec{\mu}(\omega_{rf},z)\cdot\vec{B}(z)) = -\mu(\omega_{rf})\frac{\partial B(z)}{\partial z}\hat{z}, \tag{1.58}$$

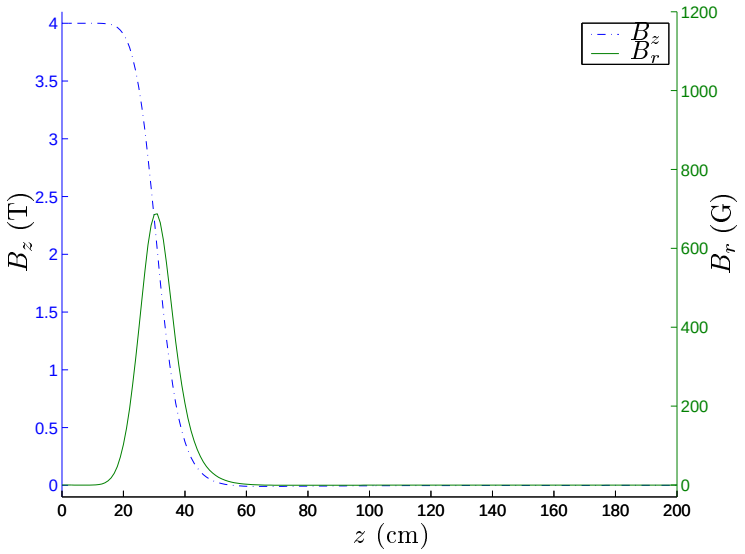

Figure 1.10: Axial B_z and radial B_r field component of the 4T magnet for the precision Penning trap at an off-axis distance of 0.5 cm. The origin is located at the magnet center.

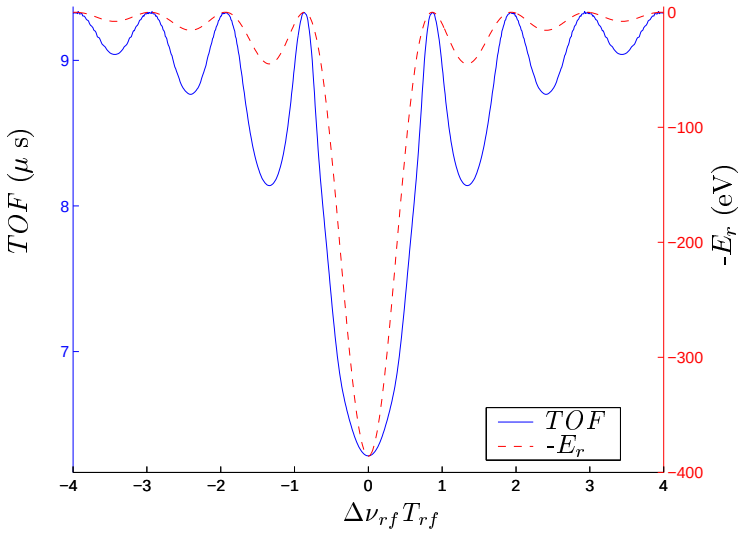

Figure 1.11: Comparison between the radial kinetic energy spectra and the corresponding Time-of-flight spectra for different excitation frequency ν_{rf}.

which converts the radial kinetic energy into axial kinetic energy. Thus, the ions which were excited at the frequency $\nu_{rf} = \nu_c$ gain the most axial kinetic energy and have, therefore, the shortest time-of-flight. The cyclotron frequency is determined with a scan of the frequency near the expected cyclotron frequency ν_c (Figure 1.11). The experimental data can be fitted with a function that describe the expected line shape [Kon95], which allows to determine the minimum. This correspond then to the cyclotron frequency.

1.5 Existing Penning trap experiment at facilities for radioactive nuclei

This section gives an overview of the existing and operational Penning trap facilities. The ISOLTRAP experiment was the first experiment in the early 90's to couple a Penning trap mass spectrometer to an on-line facility. Since then, the number of mass measurement experiments using Penning traps has steadily increased. There are currently six running experiments: ISOLTRAP at ISOLDE, Canadian Penning Trap at Argonne National Laboratory, JYFLTRAP at the Jyväskäla University IGSOL facility JYFL, LEBIT at MSU and SHIPTRAP at GSI. There are also four other experiments under construction or in the planning stage: TITAN at TRIUMF, MAFF-TRAP at the planned Munich Accelerator for Fission Fragments and HITRAP and MATS, both at GSI. Chapter two will give a detail description of the TITAN experiment, while chapter three will concentrate on the ISOLTRAP and CPT experiments. Here is a brief description of three of the above mentioned existing Penning trap experiments; in addition, the SMILETRAP experiment is presented. Although SMILETRAP is not for radioactive ions, it is coupled to an accelerator facility and is presently the only system that employs highly charged ions.

- SHIPTRAP at GSI: This experiment carries out mass measurement of nuclei that are produced at the SHIP facility [Hof00] and focuses on super heavy elements, which are produced by fusion-evaporation reactions [Dil01]. The experimental set-up consist of a gas-cell filled with noble gas for stopping and thermalization of the 5 MeV/u ion beam coming from SHIP, an extraction radio-frequency quadrupole (RFQ) that separate the extracted ions from the noble gas, a buncher RFQ to bunch the continuous beam and a doublet of Penning traps inside a 7 T magnet; one for isobaric separation and the other for mass measurement [Blo05].

- JYFLTRAP Jyväskäla University IGISOL facility: JYFLTRAP has an experimental set-up that includes three traps: an RFQ for cooling and bunching the 30 keV IGISOL beam and like SHIPTRAP, both a preparation and a precision Penning trap inside one magnet. First mass measurement from this new experiment have been carried out on nuclei Zr, Mo and Sr [Jok05].

- LEBIT at MSU NSCL facility: The LEBIT experiment is coupled via a

gas cell to the A1900 fragment separator where the fission fragments are produce. An RFQ is used for cooling and bunching the ion beam. The particularity of the LEBIT facility is the use of a 9.4 T magnet for the precision Penning trap. This allows for a decrease in the uncertainty by a factor of one-half compared to experiments using 6 T magnets. In 2005, LEBIT has carried out first Penning trap experiment by measuring the mass of ^{38}Ca [Bol05].

- SMILETRAP at the Manne Siegbahn Laboratory; This experiment located in Stockholm, is dedicated to the mass measurement of highly charged (HCI) stable ions. The CHORDIS ion source produces a beam that is sent to an Electron Beam Ion Source (EBIS) which increases the charge state of the ions. After an isobaric separation with a magnetic dipole, the beam is sent to a pre-trap that allows to adjust the typically 3.4 keV/q ion beam to an energy sufficiently low for trapping. Then, the beam enters the precision Penning trap where that mass measurement is performed [Ber02]. Over the period 1997-2002 SMILETRAP measured the mass of 21 stable species with a precision $\delta m/m < 10^{-9}$ [Ber02].

Chapter 2

The TITAN Penning Trap Experiment at TRIUMF

The TITAN experiment, based at TRIUMF, is an ion trap experiment that includes a Radio-Frequency Quadrupole (RFQ), an Electron Beam Ion Trap (EBIT), a cooling Penning trap and a precision Penning trap. One advantage that TITAN has over other Penning trap facilities is the use of an EBIT that will increase the charge state of the ions. This will ultimately allow a higher accuracy in the mass measurement for short-lived isotopes to be achieved. As shown earlier, in a Penning trap experiment, the mass of the ion is determined from the measured cyclotron frequency ν_c:

$$m = \frac{qB}{2\pi\nu_c} \tag{2.1}$$

The corresponding uncertainty in the mass measurement is given by:

$$\frac{\delta m}{m} = \frac{\partial m}{\partial \nu_c}\frac{\delta \nu_c}{m} \approx \frac{m}{T_{rf} qB\sqrt{N}} \tag{2.2}$$

Where T_{rf} is the duration of the radio-frequency excitation and N is the number of mass measurements. $1/T_{rf}$ and $1/\sqrt{N}$ are systematic and technique related uncertainty factors. Equation (2.2) shows that the uncertainty of a mass measurement decrease linearly with the charge state. Figure 2.1 shows that the use of highly charged ions (HCI) will bring the TITAN experiment into a new regime of accuracy that cannot be achieved using singly charge ions. The TITAN experiment will be able to accomplish very accurate mass measurements in the order of $\delta m/m \approx 10^{-8}$ on short-lived isotopes with a half-life of about 50 ms [Dil03]. This chapter will discuss the TITAN facility at ISAC in general. In particular, emphasis is given to the simulation of the injection and extraction optics of the mass measurement Penning trap.

2.1 Overview of the TITAN facility

This section gives a description of the four traps that will form the TITAN experimental apparatus:

- Radio Frequency Quadrupole (RFQ) for bunching and cooling the ISAC beam.

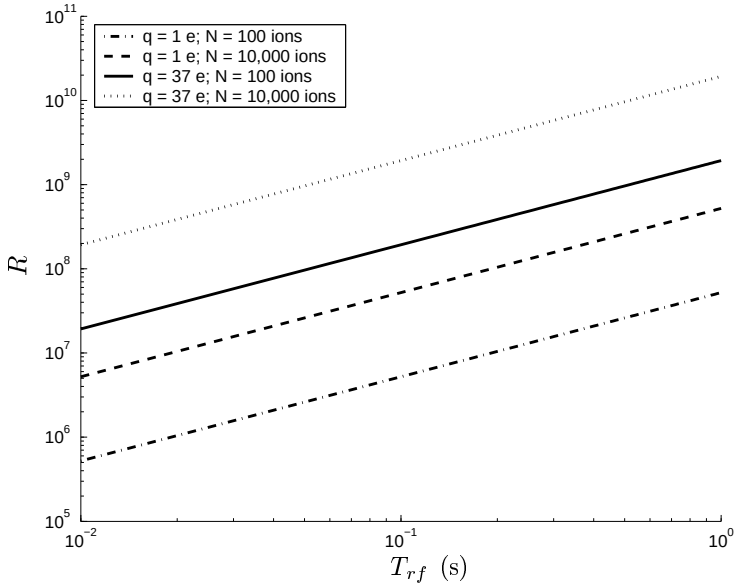

Figure 2.1: Variation of the mass measurement resolving power with the excitation time spent in the Penning trap for $^{74}Rb^{+}$ and $^{74}Rb^{35+}$.

- Electron Beam Ion Trap (EBIT) for charge breeding of the ion beam
- Cooler Penning trap to cool the ions coming from the EBIT
- Precision Penning trap to perform the mass measurement.

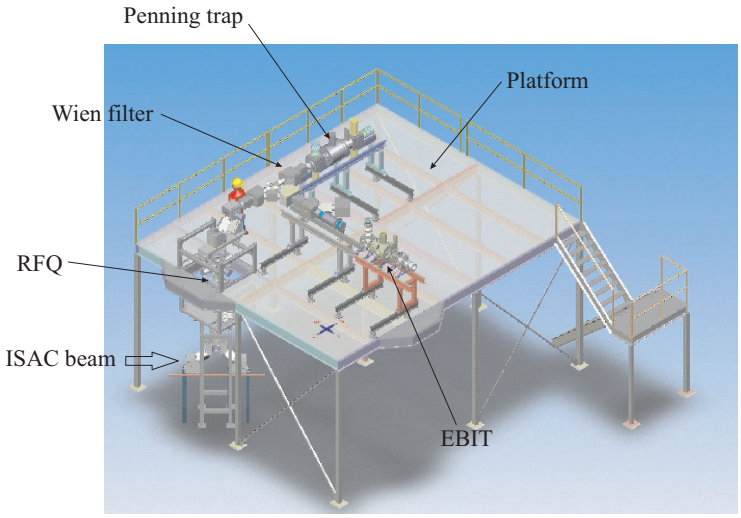

Figure 2.2: Schematic view of the TITAN experimental set-up. Shown are the ISAC beam, RFQ, Wien Filter, EBIT and the Penning trap. See text for more details.

Figure 2.2 shows the different components of TITAN's experimental set-up. Before going into a description of the different parts of the TITAN experiment, an overview of the ISAC facility will be given.

2.1.1 ISAC

The Isotope Separator ACcelerator (ISAC) at TRIUMF uses the ISOL method to produce radioactive beams. The unstable species are produced by bombarding a thick target with an up to 100 μA, 500 MeV proton beam produces by the TRIUMF cyclotron. Once produced, the different nuclei diffuse out of the target and are ionized by an ion source [Dom02]. The ions are electrostatically accelerated and formed into a continuous beam. This beam is guided through a dipole magnet separator, where the ions are selected and separated with a typical resolving power of $R = 3000$. This separated beam is delivered to the ISAC hall where various experiments are located. TRIUMF's ISAC facility produced several isotopes of 26 different elements [Dom06]. The ISAC facility also includes an RFQ accelerator and a DTL where ions with mass $A \leq 30$ are accelerated to energies of up to 1.5 MeV/u and delivered to experiments such as

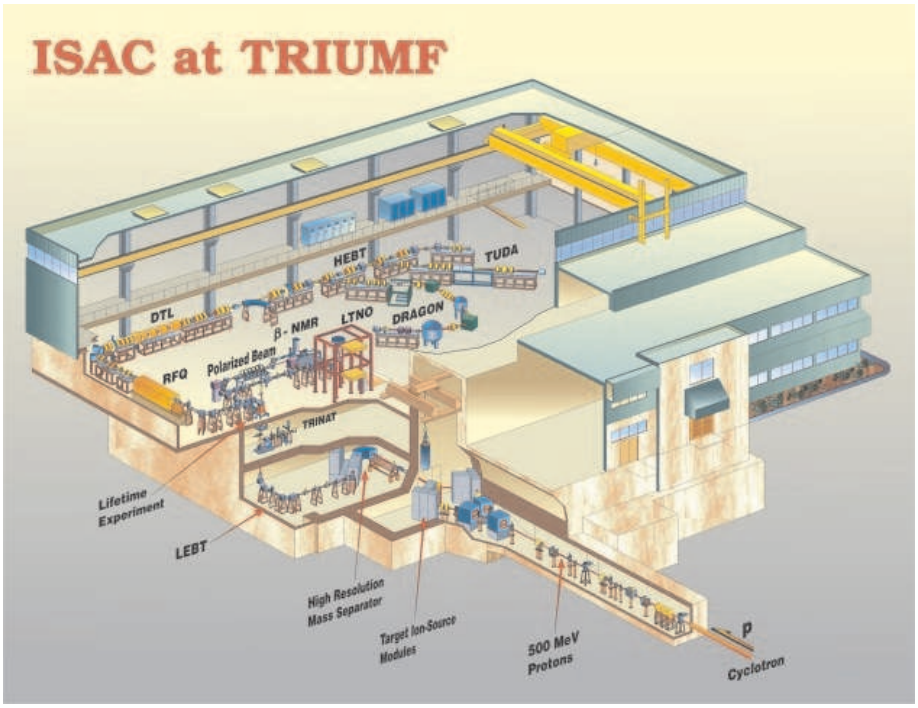

Figure 2.3: Schematic view of the ISAC experimental hall at TRIUMF

DRAGON [Hut03] and TUDA [Rui02]. Figure 2.3 shows the ISAC experimental hall at TRIUMF. The new ISAC II extension, will allow beams of energies up to 6.5 MeV/u to be produced. This is needed for experiments that probe the structure of nuclei produced in nuclear reactions such as TIGRESS [Sve03] and EMMA [Dav05].

2.1.2 The RFQ

The ISAC facility currently produces a continuous ion beam of typically 30-60 keV. In order to bring this ISAC beam into the EBIT and Penning traps, one needs to slow it down, cool and bunch it. The role of TITAN's radio-frequency quadrupole is to accept the energetic ion beam from ISAC and output a decelerated ion bunch without increasing the emittance. Such a process is called cooling and it corresponds to a decrease in the radial energy of the ion by the use of dissipative forces. To have effective cooling, the beam needs to:

- interact with a thermal bath
- enter a bath with a large enough acceptance and spend enough time inside to cool.

- be extracted from the bath without subsequent re-heating

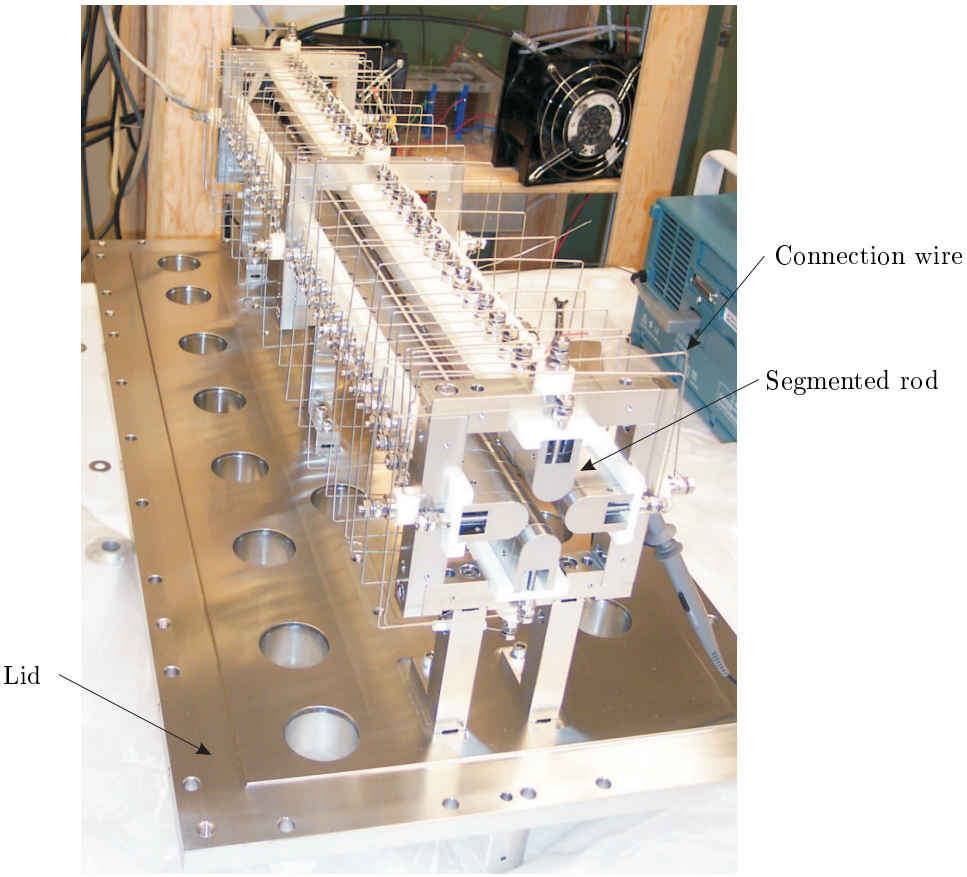

Figure 2.4: Photo of TITAN's RFQ installed on the lid of the vacuum vessel.

In the case of TITAN's radio-frequency quadrupole (RFQ) (see Figure 2.4), the cooling is provided by interaction of the continuous ISAC beam with a helium buffer gas. The large acceptance of the RFQ allows an acceptance of the ISAC beam without losses and the length of the RFQ structure allows sufficient interaction time. Without any application of radial force, the cooled ion beam would thermalize with the buffer gas and it would subsequently be lost. The radial focusing is provided by four cylindrical electrodes that create a radial harmonic potential by the application of a radio-frequency (RF) oscillations as shown in Figure 2.5.

The other important function of TITAN's RFQ is to bunch the continuous ISAC beam. Figure 2.2 shows that the beam enters and exits the EBIT through the same beam-line. To avoid any interaction between the forward and backward

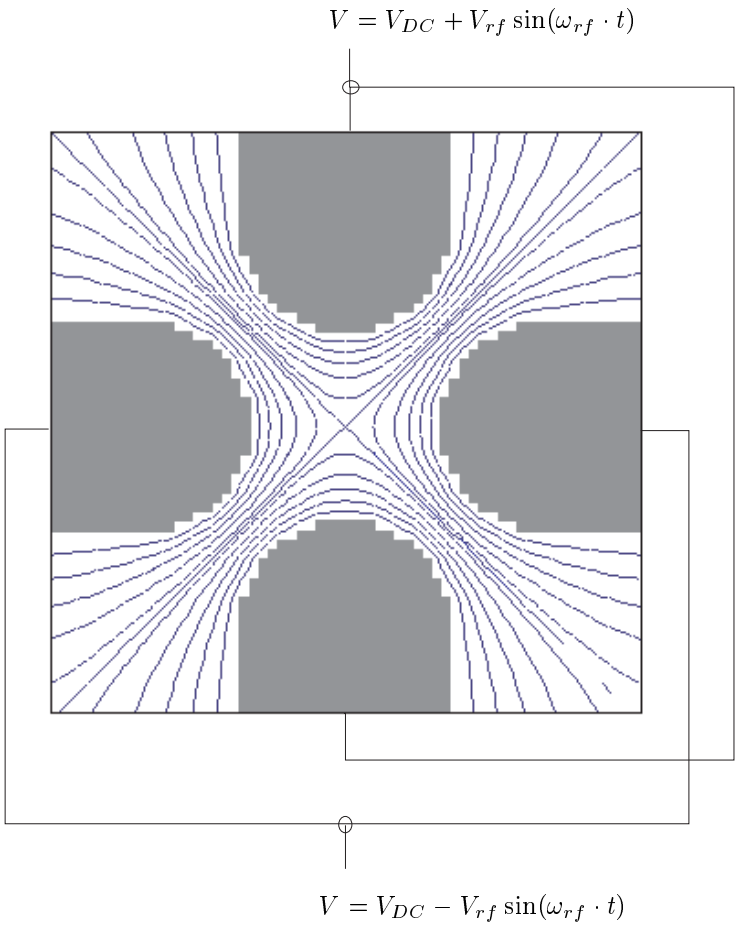

Figure 2.5: Basic scheme of a RFQ electrode structure. Shown are the applied RF-oscillation and the corresponding produced quadrupolar equipotential lines.

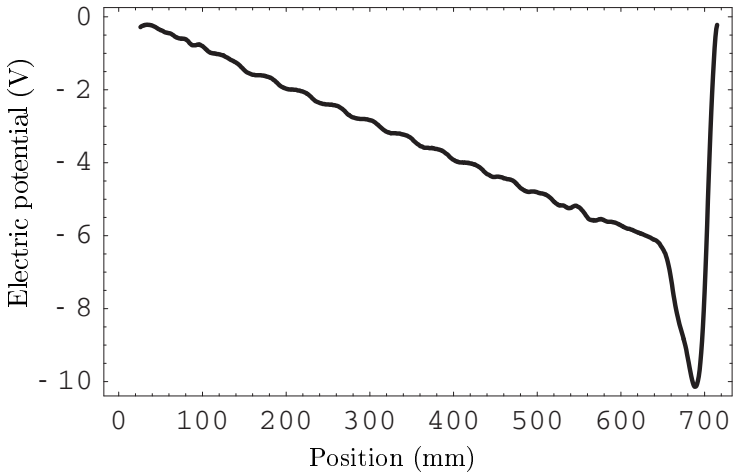

Figure 2.6: Simulation of TITAN's RFQ axial electrical potential as a function of the axial position.

directed beam, one needs to send the ions in a pulsed mode. This is possible by the application of a longitudinal trapping potential, as shown in Figure 2.6, possible by the segmenting RFQ electrode structure. The ion beam is stopped in the RFQ by floating the structure at beam potential. The ion bunches are extracted from the RFQ at energies of 2.5 keV [Smi05]. Once it leaves the floating RFQ structure, the ion bunch enters a drift tube which is switched from 30 kV - 2.5 kV to ground while the bunch is inside the tube. Then, the 2.5 keV cooled 3-10 π mm mrad ion bunch is brought into the EBIT via a transport beam line. For a more detailed description of TITAN's RFQ see [Smi05].

2.1.3 EBIT

The TITAN's Electron Beam Ion Trap (EBIT) is used to increase the charge state of the singly charged ions coming from the RFQ [Sik05]. Nine drift tube

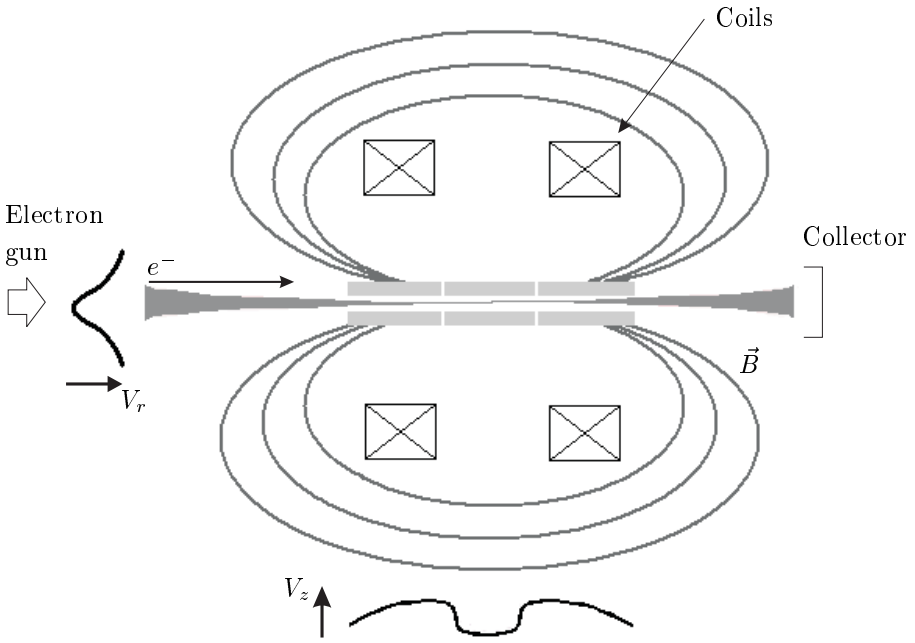

Figure 2.7: Schematic view of an EBIT. Shown are the longitudinal electric potential V_z, the potential V_r due to the electron beam, the magnetic field lines of the superconducting magnets coils in Helmholtz configuration and the compression of the electron beam produced by the electron gun due to the magnetic field.

sections allow for the application of a longitudinal trapping potential V_z, while a magnetic field produced by Helmholtz coil configuration provides the radial

confinement of the electron beam as shown in Figure 2.7. While the ions are trapped, an electron beam of width ϕ_e and current I_e increases the charge state of the ion by multiple, subsequent ionization. Several issues regarding EBIT design need to be considered, in order to fulfil the requirements for charge breeding of radioactive ions at TITAN.

- An electron beam entering a magnetic field behaves as a fluid undergoing a non-laminar flow. The beam encounters a radial compression according to Herrmann's theory [Her58] are possible. The decrease in the electron beam diameter results in a diminution of the electron impact cross section. A solution is to use an electron beam of higher intensity.

- Recombination from charge exchange with residual neutral atom gas or capture of free electrons [McL96]. This competing process of charge breeding makes it difficult to increase the charge state beyond a certain point. The electrons more strongly bounded to the nucleus can be removed by increasing the electron beam energy and chance of recombination with residual is decrease by having a very high vacuum.

- As the electron beam collides with the ions, the thermal motion of the in increases and this leads to an increase the axial energy spread of the ions. Evaporative cooling can be used to reduce the energy spread [Kin99]. In this cooling method, cold atoms with a lighter mass and lower number of protons are ejected into the trap and are immediately ionized by the electron beam. These light ions reach lower charge state than the ion of interest and are therefore less tightly bound since the trapping potential is directly proportional to the charge state. As a result, the light ions will spill out of the trap at a higher rate than the heavy ions. As they leave the trap, the light ions remove heat from the system, producing an overall cooling of the remaining trapped highly charged ions [Pen91].

Once they leave the EBIT, the ions are selected according to their mass-to-charge ratio with a Wien velocity filter.

2.1.4 Cooling Penning trap

The energy uncertainty of the ion beam entering the mass measurement Penning trap will be ultimately the limit of measurement precision that can be achieved. Hence, in order to carry out measurements with high precision, it is desired to inject a prepared and cooled beam ideally with a typical energy spread ΔE of less than 1 eV/q. However, due to the multiple electron impacts, the HCI bunches produced by the EBIT typically have a temperature of up to 50 eV/q [Ryj05a]. Experimentally, the evaporative cooling inside an EBIT, as described in Section 2.1.3, is a recent procedure and there is no evidence that it would decrease the TITAN's HCI temperature to the desirable level. Therefore, further cooling is necessary before sending the HCI to the mass measurement Penning trap. Buffer gas cooling as used in the RFQ, has to be avoided because of the high electron

capture cross section of HCI. Another possibility is electron cooling, as proposed by the HITRAP experiment at GSI [Bla05a]. It is proposed to cool the HCIs from typically 10 keV/q down to 100 eV/q by using nested electron clouds inside a cylindrical Penning trap [Bla05a]. This electron cooling process is not suitable at energies lower than 100 eV/q because of the high electron recombination cross section. Thus this method is not suitable for TITAN. TITAN proposed to cool their HCI with a novel technique using cooled protons [Ryj05a].

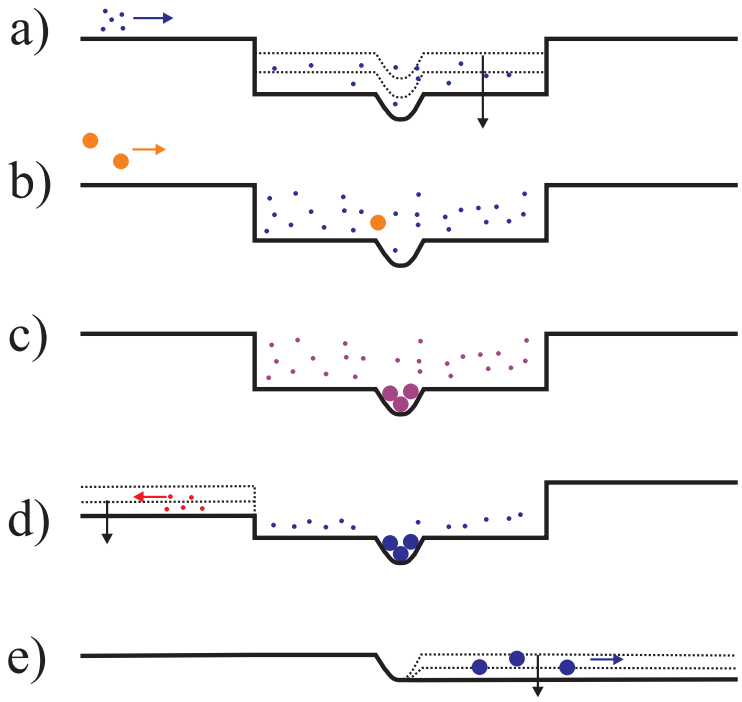

Figure 2.8: Schematic of the proposed TITAN HCI proton cooling scheme. a) the cooled protons are injected and trapped by lowering the axial potential b) the HCI bunch is ejected c) once thermalized, the cooled high charge state ions are segregated from the protons d) a gradual decrease of the entrance trapping wall releases the protons while the HCI remain trapped e) the HCI bunch is released (from [Ryj05a]).

The five phase proton cooling method is schematically shown in Figure 2.8. The proton cooling of the HCI will take place in a cylindrical Penning trap situated upstream of the mass measurement Penning trap. The protons are provided by an ion source situated upstream of the Penning trap's beam line. With their high charges, the HCI are more likely to accumulate in the bottom of the longitudinal electric potential than the protons. This is because the depth of the potential is proportional to the charge state of the confined particle. This

process permits a separate evacuation of the protons and to send pure cooled HCI bunches to the precision Penning trap.

2.1.5 Precision Penning trap

After ejection from the cooling trap, it is necessary to transport the ions into the hyperbolical precision Penning trap. The mass measurement using the TOF technique as described in Section 1.4.2 will take place in this trap.

Before entering the precision Penning trap, the 1-5 keV/q ion bunches are focused and decelerated as described later in Section 2.2.3. A dynamical capture process is applied in order to load the trap more efficiently. For the ion to enter

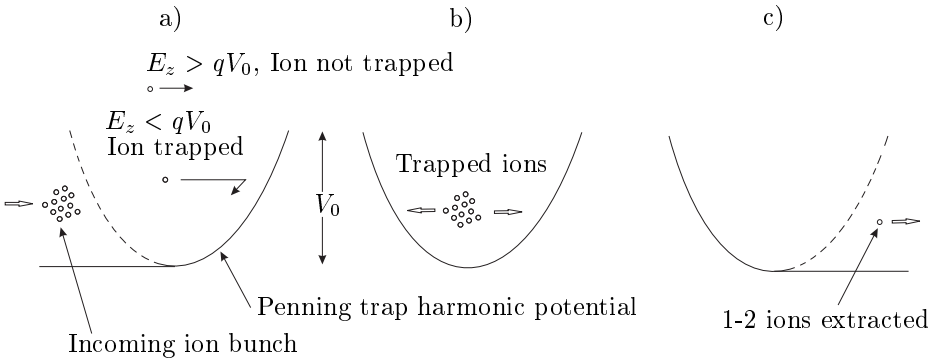

Figure 2.9: Schematic view of the injection/extraction process in a Penning trap. a) The entrance trapping potential is decreased for injecting the ions in the Penning trap b) The ion bunch is trapped after a first reflection by the trapping potential, followed by a reduction of the number of ions by dipole excitation c) Extraction of 1-2 ions from the Penning trap for TOF measurement.

the trap, a pulsed electrode configuration allows one to decrease the voltage at the trapping entrance, end cap and correction electrode is applied as shown in Figure 2.9. Depending on the potential depth V_0 and the energy spread of the beam, some ions will have too much kinetic energy to be trapped. The ions with lower energy will reflect off of the potential wall and once this first reflection is done, the entrance potential is raised back to its initial value to trap the ion bunch. The constraint on the duration of the pulse T_{pulse} depends on the axial oscillation of the ions in the trap:

$$T_{pulse} < \frac{2\pi}{\omega_z} = 2\pi\sqrt{\frac{md_0^2}{qV_0}}. \tag{2.3}$$

From Eq. (2.3), the use of HCI puts a stronger constraint on the maximum length of the pulse compared to singly charged ions since HCI have a higher axial frequency ω_z. Once the ions are trapped, the preparation of the TOF

measurement can proceed. First, as described in Section 1.4.1, the number of ions in the Penning trap is reduced by the application of two dipole excitations: an excitation of frequency ω_-, that increases the magnetron radius of all ion and a mass selective dipole excitation with frequency ω_+. This allows a selection of only the ion with the desired mass. These dipole excitations allows one to reduce the number of ions in the trap as little as one or two. This is important since the presence of several ions in the Penning trap, induces systematic errors in the TOF spectra due to the ion-ion interaction. In the TITAN experiment, the application of the first dipole excitation of frequency ω_- is not necessary because a Lorentz steerer situated upstream of the Penning trap will allow a preparation of the ion with a well defined magnetron radius before it enters the trap. A detailed description of TITAN's Lorentz steerer is given in Section 2.2.3.

After the isobaric-cleaning, the ion undergoes a quadrupole excitation ω_{rf} provided by the segmented guard electrodes. The advantage of applying the rf-excitation on the guard electrodes instead of the ring, as previously carried out at other experiments, is that it allows one to keep a constant and uniform DC voltage V_0 between the end caps and ring electrode while a quadrupole excitation is performed. Once the quadrupole excitation is completed, the ions are extracted from the trap following the same procedure as the injection show in Figure 2.9. In the TOF technique describe in Section 1.4.2, the mass of the ion can be deduced by determining the position of the minimum of the TOF spectrum. Section 2.2.3 will show that the applied potential on the extraction electrodes determines the amplitude and width of the cyclotron frequency TOF peak.

2.2 Ion optics simulations for the TITAN experiment

2.2.1 Definition of the emittance

The particles within a beam have a kinetic energy spread as well as an angular divergence with respect to its direction of propagation. A beam can be seen as a thermodynamic system that follows Liouville's theorem [Wol87]:

> For a cloud of moving particle, the particle density $\rho(x, p_x, y, p_y, z, p_z)$ in phase space is invariant.

Where x,y,z define the position and p_i its momentum. Assuming that the motions of the particles along each coordinates of the three dimensional space are independent, Liouville's theorem reduces to the conservation of the area enclose by all particles in the three position-momentum planes: x-p_x, y-p_y and z-p_z. The transverse emittance ε is define has the area in the transverse x-x' and y-y' planes, while the longitudinal emittance is the area in the axial energy-time plane. The primes denotes derivatives along the longitudinal direction z.

The emittance is a useful quantity that is deducted from Liouville's theorem: for a non-relativistic particle moving in free space, x' and y' are equal to:

$$x' = \frac{dx}{dz} = \frac{p_x}{p_z} \tag{2.4}$$

$$y' = \frac{dy}{dz} = \frac{p_y}{p_z}. \tag{2.5}$$

If there is no coupling between the x and y coordinates and if p_z does not change with z, the area occupied by all particle in the x-x' and y-y' planes, or the emittance of the beam, remains invariant. Since the trajectory of ion passing through a linear ion optic device in the x-x' and y-y' planes is elliptical, it is convenient to define the area enclose by the beam in phase-space as being elliptical. Emittance plots often involve the "diverging angle" θ between the axial and radial momentum of the ion. For a small angle the order of mrad, the small angle approximation can be used:

$$x' = \frac{p_x}{p_z} = \tan\theta_x \simeq \theta_x \tag{2.6}$$

$$y' = \frac{p_y}{p_z} = \tan\theta_y \simeq \theta_y. \tag{2.7}$$

For a uniform distribution of ions in phase-space, the emittance is the area of the ellipse englobing all ions. In the case of a Gaussian distribution, the emittance is the area of 90 % of the ions (2σ). The emittance is given in π mm mrad. It is important to mention that ε is not a conserved quantity if p_z is changing with z as is the case for a decelerating beam. The "normalized emittance" ε_N which is the product of the emittance ε with the axial momentum p_z is the invariant quantity [Law77].

2.2.2 General description of an Einzel lens

Before the discussions about ion optics simulations, a small overview about the Einzel lens is necessary. An Einzel lens is composed of a drift tube section operated at a different potential than rest of the beam line. The potential applied on the Einzel lens V_{EL} can be either smaller or greater than the beam line potential V_{float}. The first corresponds to an accelerating Einzel lens, while the second is a decelerating Einzel lens. In Figure 2.10 the effect of the accelerating and decelerating Einzel lens was simulated using SIMION 3D 7.0 [Dah00]. All the simulations presented in this thesis where carried out using SIMION 3D 7.0. In the first case, the beam entering the lens is initially focus due to the inward electric field. For a decelerating Einzel lens, the beam is initially defocused by the electric field, but since it is closer to the electrode, it is then more strongly refocused. Both types of Einzel lens can lead to an overall focusing of a diverging beam, but due to its initial defocusing, the decelerating Einzel lens presents bigger aberrations, as shown in Figure 2.10.

For an ideal Einzel lens, the focusing forces applied on the ions are directly proportional to the radial position of the ion, allowing all ions to focus at the

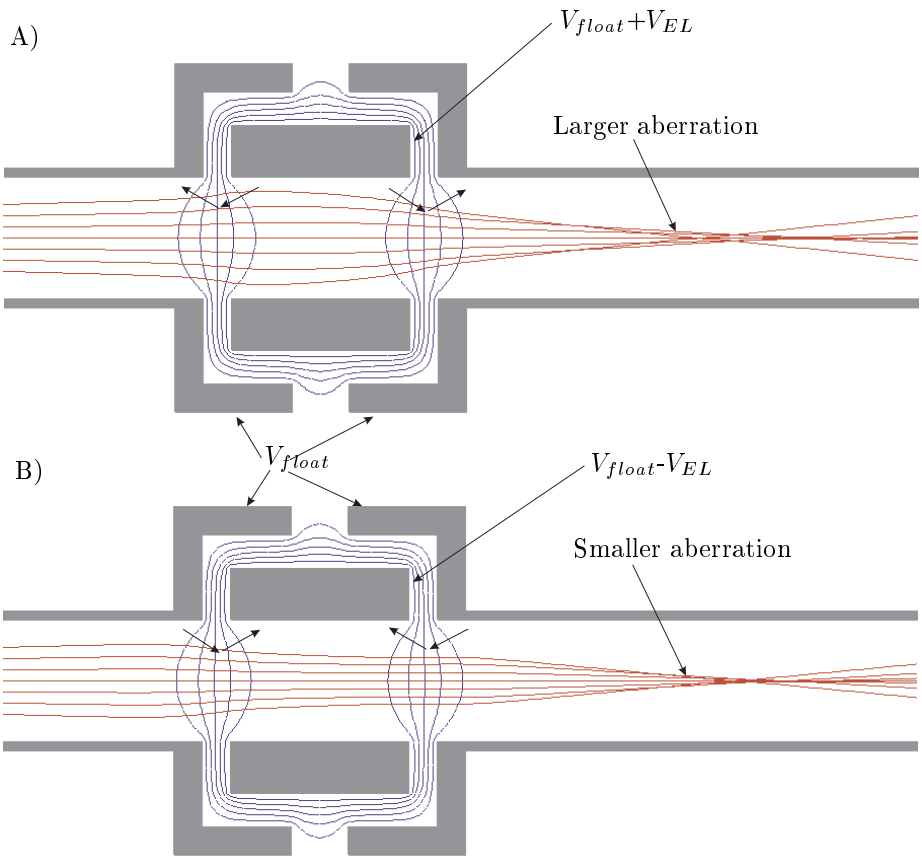

Figure 2.10: Comparison between a decelerating and accelerating Einzel lens. V_{float} is the beam line potential and V_{EL} is the Einzel lens offset potential. The arrows represent the direction of the electric field while the lines are the equipotential lines. A) Decelerating lens broadens the beam leading to bigger aberration at the focal point. B) Accelerating lens decreases the beam size and spherical aberration.

same point. On the other hand, for a real Einzel lens, such as the ones discussed above, the presence of the electrode causes a non-linear focusing of the ion bunch. This gives raise to the so-called "spherical aberrations": depending on their radial position inside the lens, the ions are focused at different axial positions, the ion from the envelope being more strongly focused than the ions from the central part of the beam, as shown in case B) of Figure 2.10. Spherical aberrations induce a "filamentation" of the beam in radial the phase-space y-θ_y planes due to the finite size of the Einzel lens. Since the contribution of the non-linear forces increase as the ions gets closer to the Einzel lens electrodes, the spherical aberrations can be reduced by increasing the inner diameter of the Einzel lens. In the next section, an Einzel lens is placed after the RFQ in order to focus the beam getting out of the RFQ into a 3mm diameter aperture. In order to decrease the effect of spherical aberration, this Einzel lens was chosen to have an inner diameter of about two times bigger than the drift tube.

2.2.3 Extraction optics from the RFQ

The beam line after the RFQ has the following features:

- To avoid re-acceleration of the beam as it passes from the RFQ linear trap which is located on high voltage potential, to the beam line on grounded potential, a pulsed drift tube is placed after the RFQ. When the ion bunch gets into the pulsed drift tube, the potential is switch from 30 kV - 2.5 kV to ground, without affecting the ion bunch size and kinetic energy.
- Two devices allow a separation of the RFQ beam line from the rest of the system: a gate valve that one closes when a part of the system is vented and a 3 mm diameter aperture that allows for differential pumping.
- In order to provide for efficient transfer through the 3 mm aperture, an Einzel lens is placed half way between the RFQ and this aperture.

Since the pulsed drift tube and Einzel lens have different diameters, a matching between the two that minimized spherical aberration needed to be done.

Two different matchings were tested: a 90° opening of the pulsed drift tube (see Figure 2.11 (A)) and a flaring of the pulsed drift tube (see Figure 2.11 (B)). Two factors where taken into account for this presented concept; the penetration of the Einzel lens electric field inside the pulsed drift tube and the spherical aberration produced by the lens.

To see clearly the effect of spherical aberration, the beam was defined as a point source with a 10 mrad divergence situated at the beginning of the pulsed drift tube. This beam was then refocused at the entrance of the 3 mm aperture. The spherical aberration due to the finite size of the Einzel lens creates a filamentation of the beam in the θ_x-x and θ_y-y phase-space as discussed in the previous section (see Figure 2.12). In the simulations, the length of the flaring (h) in case (B) was changed from 11 mm to 51 mm and the length of the filamentation was measured.

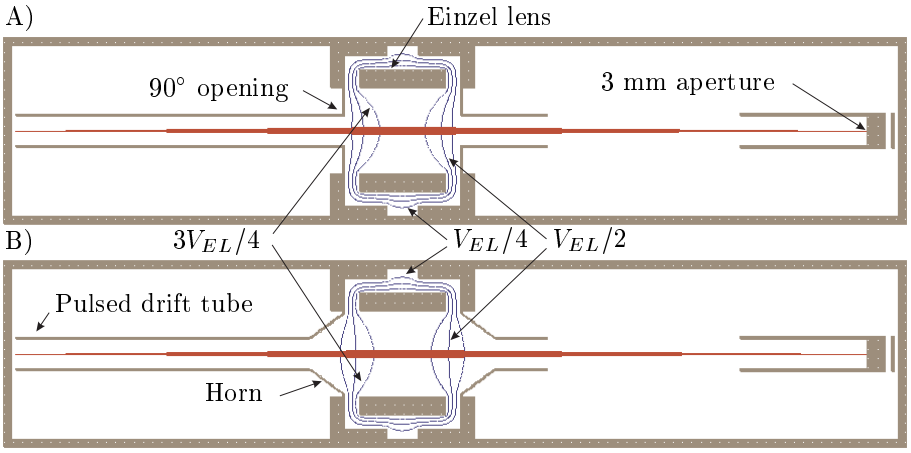

Figure 2.11: Comparison of the shape of the equipotential $V_{EL}/4$, $V_{EL}/2$ and $3V_{EL}/4$ produce by the Einzel lens for a pulsed drift tube that A) finish by a 90° opening, B) has a $h = 31$ mm horn.

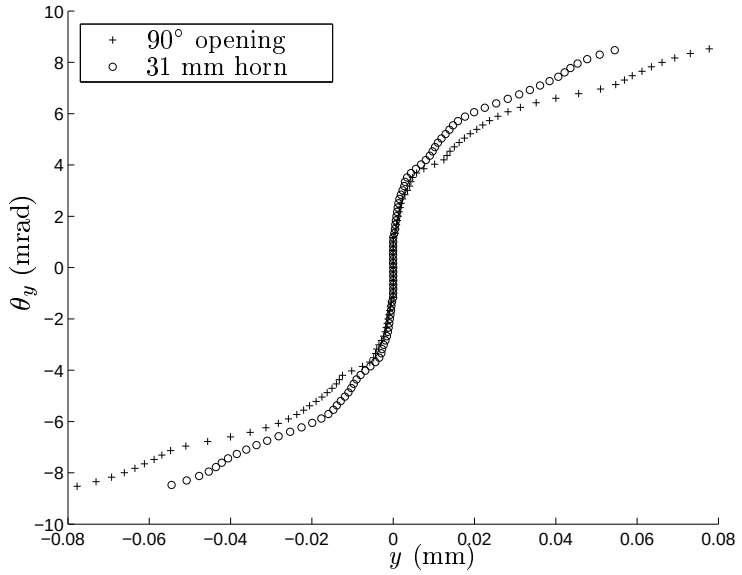

Figure 2.12: Filamentation of an initial 10 mrad point source situated at the beginning of the pulsed drift tube and refocused at the 3 mm aperture by an Einzel lens. Calculations for two different drift tubes are shown: 31 mm long horn and a 90° opening.

Table 2.1: Variation of the penetration p as a function of the distance from the end of the drift tube at which the potential is 0.1 V and the length of the filamentation tail Δx for different lengths of the horn h.

h (mm)	p (mm)	Δx (μm)
0	32	78
11	39	59
21	45	55
31	50	53
41	55	53
51	60	53

The electric field penetration from the RFQ and Einzel lens inside the drift tube when it is grounded determines its effective length, i.e. the part of the tube in which the kinetic energy of the ion bunch would be minimally affected during the pulsing. In Section 2.2.3. it will be shown that the average radial kinetic energy of the beam entering the Penning trap is about 4 eV, thus in order to minimize the energy spread of this beam, the penetration p was taken as the point where the potential had a value of 0.1 V. Therefore, the length of the flair h was determined from the size of the filamentation Δx and the penetration p of the Einzel lens electric field inside the pulsed drift tube.

Table 2.1 shows the results of the simulations. The case $h = 0$ mm is special since it is when the drift tube is connected with the Einzel lens ground electrode by a 90° opening and it presents the highest aberrations.

Table 2.1 also shows that increasing the flaring length beyond $h \geq 21$ mm, barely the size of the filamentation tails. This is because for $h \geq 21$ mm, the contribution from the horn geometry to the filamentation is negligible compared to the one from the finite size of the Einzel lens. At the same time, the effective length of the drift tube is reduced by 15 mm.

Therefore, is was founded that the best matching can be achieved by flaring the pulse drift tube after the RFQ. Since the spherical aberrations produced by the horn get negligible when $h \geq 21$ mm, the matching between the pulsed drift tube and the Einzel lens will be achieve with a 21 mm long flare.

2.2.4 Injection optics for the Penning trap

The injection of the beam into the precision Penning trap is critical and requires the diameter and radial kinetic energy of the ion bunch to be minimal since it will have an impact on the initial ion motion in the trap. This section is divided in four parts: motivation for the injection simulation, determination of the Einzel lens position, simulations using an Einzel lens, simulations of the Lorentz steerer and injection optics design.

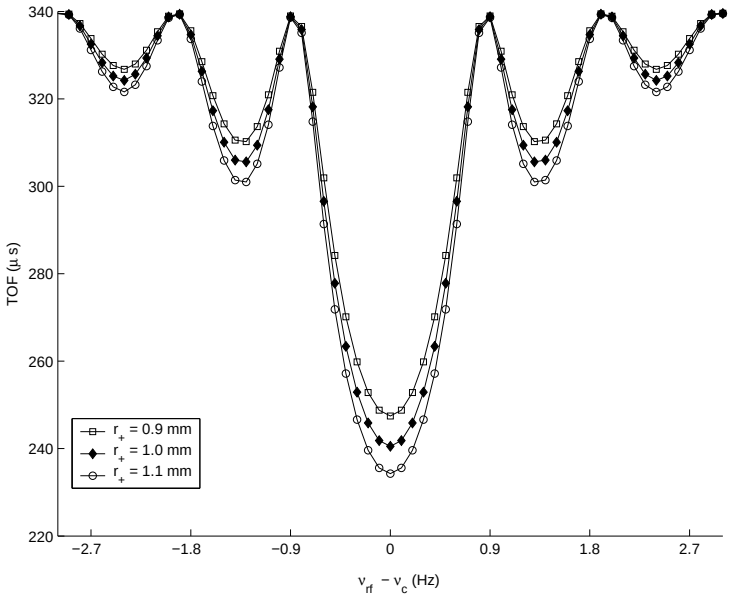

Figure 2.13: Time-of-flight spectra for different initial cyclotron radius. A variation of in the cyclotron radius affects the full-width-half-maximum and amplitude of the central peak, which translates into uncertainty in the determination of the cyclotron frequency ν_c. See text for more details.

Motivations for injection simulations

The spread of the radial diameter of the ion pulse that enters the Penning trap is a source of uncertainty in the TOF spectra, hence a systematic error in the mass determination. After the complete conversion into reduced cyclotron mode, the ions starting with different initial magnetron radius r_- will end up with different reduced cyclotron radius r_+ and thus different radial kinetic energies:

$$E_r = \frac{1}{2} m \omega_+^2 r_+^2. \tag{2.8}$$

This difference in E_r translates into an uncertainty in the TOF spectra. As an example, in Figure 2.13, the time-of-flight (TOF) spectra of singly charged ions of mass m = 74 u for different initial cyclotron radius was calculated. In this example, a variation of 10% in the cyclotron radius results in a 2% change in the full-width-half-maximum and of 7% in the amplitude of the TOF central peak.

Therefore, the beam diameter d_f entering the Penning trap needs to be minimized. Contrary to the previous section where the beam leaving the RFQ was focused in a 3 mm aperture by an Einzel lens, in the case of the Penning trap, the

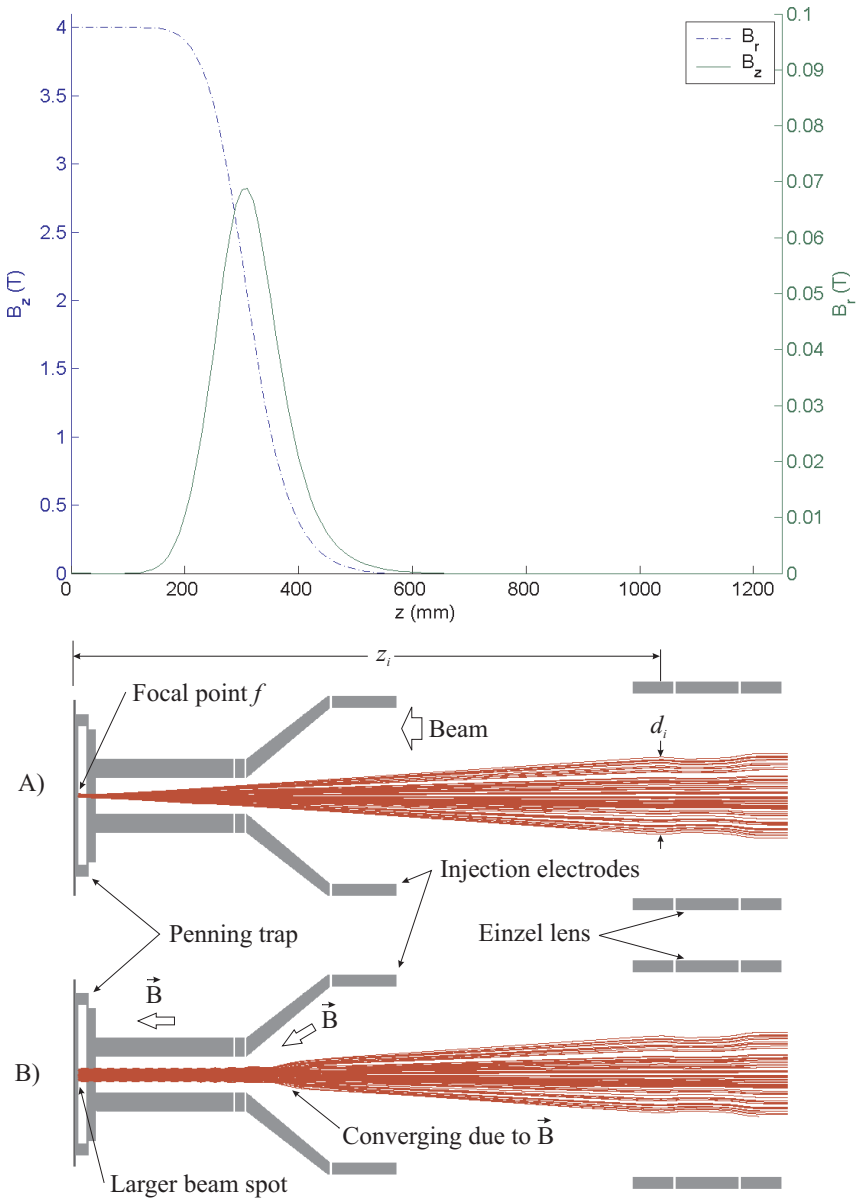

Figure 2.14: Injection of a 20 mm wide beam at the Penning trap entrance. A) Without any magnetic field, the Einzel focuses the beam at the Penning trap entrance. B) The presence of the strong axial magnetic field produced by the superconducting magnet, cancels the focusing effect of the Einzel lens leading to a bigger beam spot at the Penning trap entrance. The upper panel shows the the axial magnetic field B_z together with the radial magnetic field B_r. See text for more details.

strong magnetic field produced by the superconducting magnet will cause the ion beam to undergo a cyclotron along the magnetic field lines. Figure 2.14) shows that the size of the originally focused beam entering the Penning trap is increased by the presence of the strong magnetic field produced by the superconducting magnet. There is two important feature shown in Figure 2.14); between 250 mm and 400 mm, the beam size is decreased by the converging magnetic field present in that region. Between 0 and 250 mm, the beam diameter remains unchanged. Both features shows that for $z < 400$ mm, the ion motion is mainly determined by the direction of the magnetic field. Therefore, a determination of the focal point f that will minimized the beam diameter d_f entering the Penning trap is necessary.

The second parameter that must be determined is the beam diameter where the focusing starts d_i. For constant beam emittance, varying the beam diameter d_i will change the angular divergence of the beam. As shown in Section 2.2.1, the emittance of a beam can be approximated by the area of an ellipse enclosing all beam particles in the phase-space x-θ_x, where θ_x, is the angle between a radial component of the particle velocity and its axial velocity. Therefore, in order to conserve the emittance, a decrease of the beam diameter d_i, for instance, needs to be compensated by an increase in the angular divergence of the beam. If the angular divergence of the beam entering the magnetic fringe field is too large, it will cause the ions to be reflected by the magnetic field. The magnetic force applied on the ions that enters the magnetic field with a large angle $\vec{F} = q\vec{v} \times \vec{B}$ will reflected them perpendicular to the magnetic field, thus away from the trap entrance. Therefore, a determination of diameter of the beam when it start to get focused is necessary.

The last parameter to be varied is where the ion beam start to focus z_i, which will determine the position of the Einzel lens. The distance between f and z_i will set the strength of the focusing, which is an important factor in final size of the beam entering the trap. A small separation between f and z_i for instance, will give a very strong focusing at the focal point, leading to reflection of some ions by the magnetic field.

In the following section, the optimal position of the Einzel lens that will focus the beam before the strong magnetic field region has been determined.

Determination of the Einzel lens position

Following the previous discussion, the beam entering the trap can be described in the following way:

- its diameter d_i
- position of the beam focusing z_i
- the location of the focal point f
- its emittance ε
- its axial kinetic energy E_z

Simulations have been carried out to determine the required parameters of f, d_i and z_i to minimize the final beam diameter d_f.

The axial kinetic energy of the ions in TITAN's transport beam line is expected to go from 1 to 5 keV/q and the worse extracted emittance from the RFQ given by simulations is: 10 π mm mrad for a 2.5 keV/q ion bunches [Smi05]. Thus, assuming that no changes in the beam emittance occur in the transport from the RFQ, in the following simulations, the emittance of the beam entering the mass measurement Penning trap was set to 10 π mm mrad. To be more conservative, an axial beam energy of 5 keV/q was used in this simulation, which represents a beam of poorer quality than what is expected from the RFQ. Note that in order to cover the possible range of energy of TITAN's beam line, simulations with a 20 π mm mrad 1.25 keV/q beam are shown at the end of this subsection. The ion beam starts with an axial energy spread of 5 eV/q, which is the energy spread of the ISAC beam line. The ions have a mass of $m = 2$ u and a charge of $q = 1$ e, for an overall m/q ratio of 2, a typical m/q ratio for HCI. Simulations with singly charged $m = 74$ u ions has also been made in order to cover the range of mass expected to be measured at TITAN.

A magnetic field map has been generated according to the on-axis axial $B_z^{data}(z,r = 0)$, the off-axis axial $B_z^{data}(z,r = 5$ mm) and the off-axis radial $B_r(z,r = 5$ mm) magnetic field values given by the 4T magnet manufacturer. For a brief overview on how the magnetic field map was generated, see Appendix A.1.

In order to find the best conditions, each of the three parameters f, d_i and z_i was varied independently, leaving the other two constant. To see how each parameters were varied in the simulations, see Appendix A.2. The beam is assumed to have an initial diameter $d_i = 2$ cm, which is a typical beam envelope size expected from the RFQ, assuming no change in the transport. The position where the beam starts to focus was set to $z_i = 900$ mm; this corresponds to the position of one of the 6-way cross used for vacuum pumping. In order to see their effect on d_f, each parameter where varied over a broad range. The focal point f is the first parameter to be varied. Then, d_i was varied using the value of f that minimized d_f previously founded. Finally, z_i was varied using the two previous results. Figure 2.15 shows the effect of the variation of each parameters on the beam diameter and radial kinetic energy entering the Penning trap.

The parameter f was varied from the trap center position to 800 mm from the trap center. The smallest final beam diameter was found to be 0.75 mm when the beam is focused at $f = 400$ mm from the trap center and the corresponding final radial kinetic energy of the beam is 2.5 eV. For decreasing values of f smaller than 400 mm, the beam width entering the strong magnetic field region gets bigger, resulting in a bigger beam spot at the entrance of the trap. For increasing values of f bigger than 400 mm, the focal length decrease, leading to a stronger divergence of the beam as it enters the magnetic fringe field. Thus, as was explained earlier, the magnetic force applied on the ion will increase the beam size before it enters the strong magnetic field region, giving consequently a bigger diameter to the beam as it enters the Penning trap.

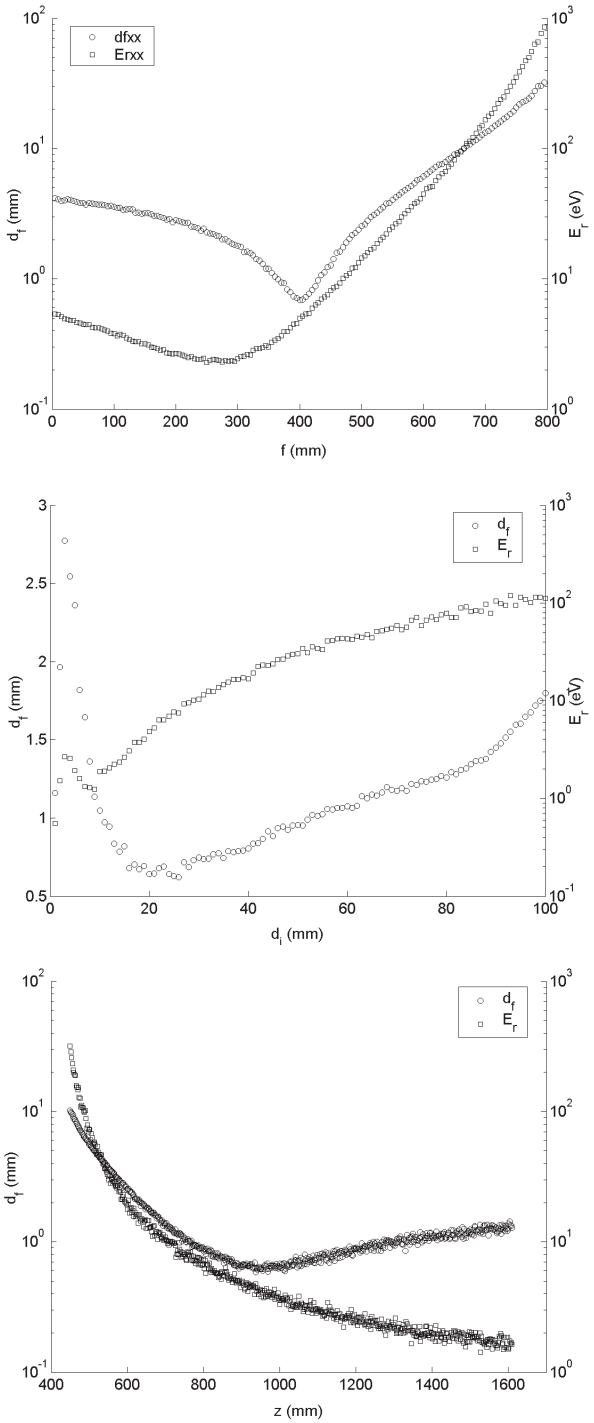

Figure 2.15: The final ion beam diameter d_f was minimized by varying subsequently the focal point position f, the initial beam diameter d_i and the point where the beam start to focus z_i, taking each time the position, shown by the arrows, where d_f was founded to be minimal. The corresponding radial kinetic energy of the beam is also shown. For more details about the results, see the text.

Table 2.2: Starting parameters that gives a minimal d_f, for different masses and distributions.

	m = 2 u (flat)	m = 2 u (Gauss.)	m = 74 u (Gauss.)
f (mm)	400	400	325
$d_i(mm)$	20	24	18
z_i (mm)	950	1050	1050
d_f^{min} (mm)	0.65	0.57	1.6
$E_r(d_f^{min})$ (eV)	4.2	3.8	0.4

Following this simulation, assuming that the beam starts 900 mm from the trap center and focuses at 400 mm, the initial beam size was varied from 1 to 100 mm. Figure 2.15 shows that the final beam size is a minimum when the initial beam size was 20 mm. Note the different scale on which d_f vary. There are two features in the variation of the initial beam diameter d_i; the increase of the angular spread of the ions forming beam as the beam size decrease at constant emittance and the increase of the angle at which the beam penetrate the magnetic drift field as the beam size increase. $d_i = 20$ mm correspond to the point where the two effects compensates each other.

Taking the results of the previous two sections, $f = 400$ mm and $d_i = 20$ mm, in Figure 2.15, the initial beam focusing point z_i was changed from 450 mm to 1610 mm. The final beam size was found to be minimal at $z_i = 950$ mm and varies slowly for increasing values of z_i, while the radial kinetic energy E_r steadily decreases.

The decrease in d_f as z_i change from 450 mm to 950 mm is due to the decrease of the angle at which the ion beam enters the magnetic fringe, while the increase in d_f as z_i increase beyond 950 mm is due to the angular spread of the beam due to the emittance, that becomes more important as the separation between z_i and f increase.

Table 2.2 summarize the parameters of the beam when it has its minimal final size. The second column of Table 2.2 is the results of an other d_f minimization, this time using a circular beam with a Gaussian ion distribution both in the emittance and in the beam density. The results of both simulations agree well together. Because of the slow variation in the final beam size near the minimum for d_f, the different value of d_i and z_i founded for the Gaussian distribution, as a minute impact on d_f.

The third column shows that for a beam of particles of mass 74 u and charge 1 e the minimal beam size achieved is larger than that found for the ions with the 2 u mass. In both simulations, the ion beam started with a 5 keV/q axial kinetic energy, this means, that the ions of higher mass get into the magnetic field with a smaller velocity and therefore, the focusing due to the magnetic force will be smaller, resulting in a bigger final beam spot. Since a smaller radial force is applied on the mass 74 u ions than the mass 2 u, a smaller amount of axial kinetic energy will get converted into radial kinetic energy.

Table 2.3: Minimal final beam diameter and the corresponding radial kinetic energy for different initial beam.

E_z (keV)	1.25	5	5
m (u)	2	2	74
σ (mm)	14	14	9
V_{EL} (V)	-800	-3180	-3080
d_f^{min} (mm)	1.05	0.78	1.87
$E_r(d_f^{min})$ (eV)	1.83	3.43	0.42

To conclude, a minimized beam diameter d_f entering the Penning trap was founded for a $d_i = 24$ mm wide converging Gaussian distributed ion beam starting at $z_i = 1050$ mm and focusing at $f = 400$ mm from the trap center. The parameters z_i and f determine the position and focusing strength of the Einzel lens that the TITAN experiment will have to include to its injection optics.

Simulation using an Einzel lens

In these simulations a 110 mm long Einzel lens with an inner diameter of 30 mm is placed at the optimal distance $z_i = 1050$ mm, as found in the previous section. For the initial conditions, a collimated beam with a Gaussian velocity and coordinate distribution is assumed. In order to minimize the spherical aberration at the focal point, a decelerating Einzel lens was used (see Section 2.2.2 for more details). In these simulations, the effect on the final beam diameter and radial kinetic energy of changing the initial axial kinetic energy and mass of the ion is determined.

To cover the possible range of kinetic energy that the ion beam can have in TITAN's transport beam line, the impact of the decreasing the axial kinetic energy of the beam to 1.25 keV was determined. In order to conserve the normalized emittance, the emittance of the 1.25 keV beam has to be:

$$\varepsilon(1.25\text{keV}) \cdot p_z(1.25\text{keV}) = \varepsilon(5\text{keV}) \cdot p_z(5\text{keV}) \tag{2.9}$$

$$\varepsilon(1.25\text{keV}) = \sqrt{\frac{5\text{keV}}{1.25\text{keV}}} \cdot \varepsilon(5\text{keV}) = 20\ \pi\text{mm mrad} \tag{2.10}$$

As shown in Table 2.3, for the same initial beam diameter, the minimal beam size achieved for a 1.25 keV is wider than when the beam has an energy of 5 keV. It is due to the increase of the emittance.

The last case studied is a singly charged ion beam of mass 74 amu. This is the worst case in terms of the final beam size (see Table 2.2), this is because the axial velocity of the ions entering the magnetic fringe field is smaller, resulting in a weaker focusing of the ions due to the magnetic force. However, since the beam properties depend on the m/q ratios, the use of highly charged ^{74}Rb ions with a ratio of $m/q \sim 2$ is similar to using singly charged ions of mass $m = 2$ u.

Injection optics design

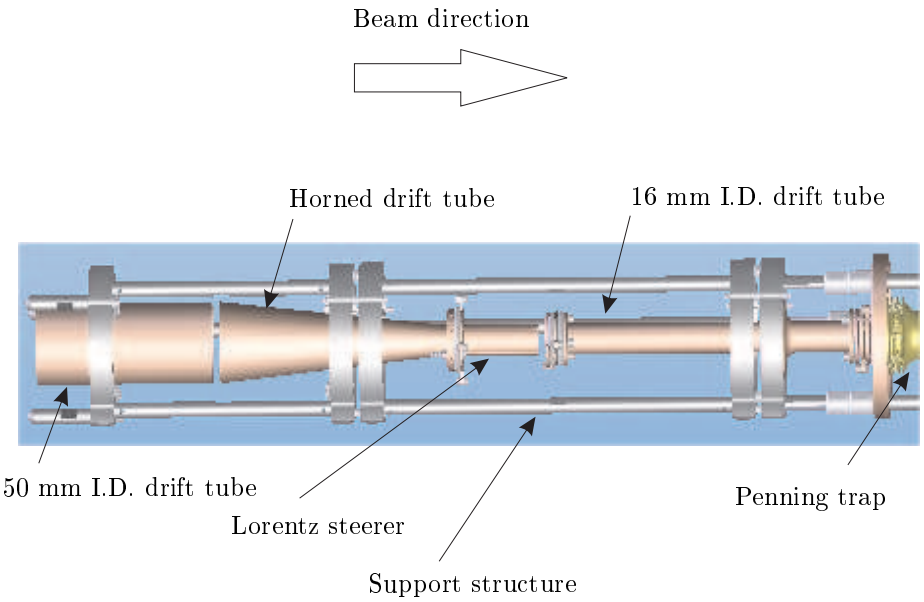

Figure 2.16: Rendered design drawing of the electrode structure for the injection into the TITAN's mass measurement Penning trap. Shown are the different drift tube section, the Lorentz steerer, the Penning trap and the support structure.

Figure 2.16 shows the design of the electrode structure for the injection of the ion bunch into the precision Penning trap. This comprises of several optical components for the injection into the trap, such as:

- A horned drift tube with a shape following the magnetic fringe field lines. Inside the strong magnetic field region, the ions undergo cyclotron motion around the magnetic field lines. As they move into the strong magnetic field region, the ions will spiral along the converging field lines resulting in a decrease in the beam size. Therefore, inside the strong field region, one can use a drift tube with a smaller diameter. The flaring of the drift tube simply implements a smooth transition between the two different drift tube diameters.

- After the horned drift tube, a Lorentz steerer [Rin05] allows a preparation of the ions with well defined radius which results in a specific magnetron motion in the trap. The Lorentz steerer is made of a drift tube which is longitudinally segmented into four equal parts allowing for the creation of an electric field perpendicular to the magnetic field of the magnet (see Figure 2.17). The cross product of the electric and magnetic field comprises

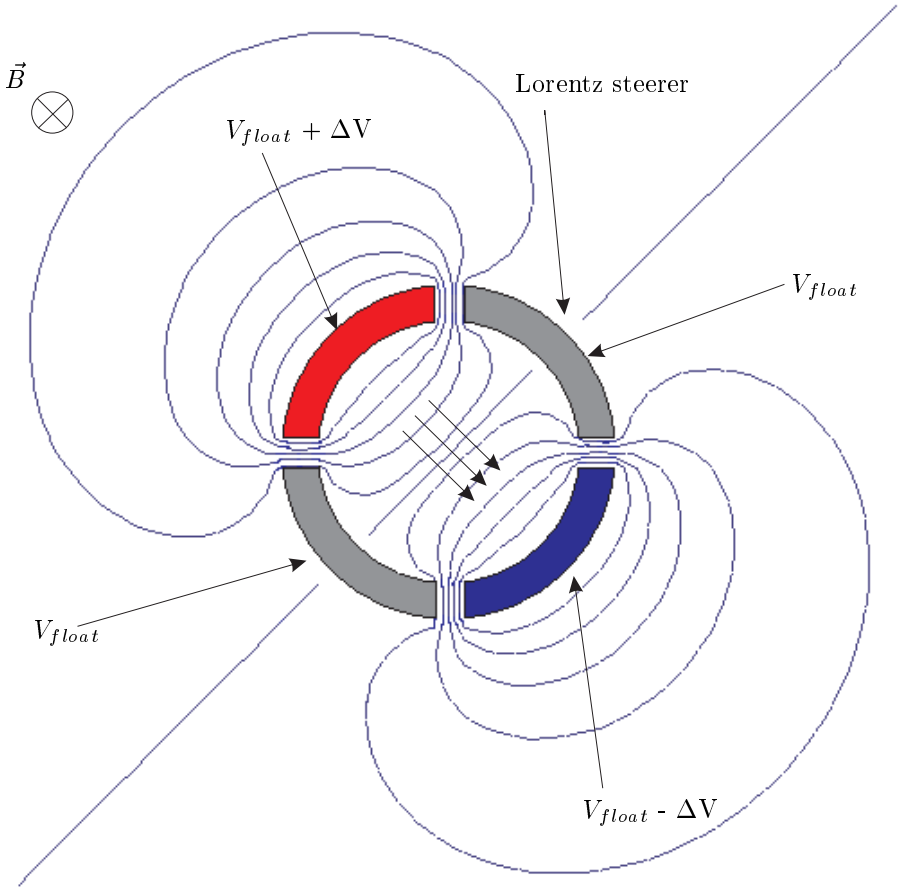

Figure 2.17: Simulations cross sectional view of a schematic for a Lorentz steerer. Shown is the electrode configuration necessary to create the potential which will steer the ion beam. V_{float} is the drift tube potential and ΔV the Lorentz steerer potential shift. Equipotential lines have a distance of $\Delta V/5$. The arrows represent the electric field direction. The magnetic field B perpendicular to the electric field is also shown.

Table 2.4: Parameters used in the study of the Lorentz steerer

V_{DT} (kV)	ΔV_{steer} (kV)	Δr (mm)	d_f (mm)	$\overline{E}_r$ (eV)	σE_r (eV)
0	0	N/A	0.9	3.8	2.9
0	1.1	1.0	0.9	80.3	23.5
4.5	0	N/A	0.8	3.8	2.9
4.5	0.35	1.0	0.8	4.1	2.9

a velocity filter that induces a magnetron motion as describe in section 1.4.1. Since the Lorentz steerer is inside a region of strong axial magnetic field, the induce magnetron displacement on the bunch remain constant as the ions fly from the steerer to the Penning trap.

Simulation of the Lorentz Steerer

As explain in the previous section, a Lorentz steerer creates an axial displacement of the beam before it enters the Penning trap. This gives a non-zero initial magnetron radius to the ion bunches in the Penning trap. The effect of the Lorentz steerer on the final beam size and radial kinetic energy has been simulated and is discussed in the following.

The simulations use the optimal injections conditions found in the previous section, i.e. an Einzel lens is placed at $z_i = 1050$ mm focuses a collimated Gaussian beam at 400 mm from the trap center. Two sets of simulations were carried out; one with grounded injection drift tubes and the other with the drift tubes floating at 4.5 keV above ground. In the first case, where the injection drift tube was grounded, the kinetic energy of the beam entering the Lorentz steerer was 5 keV. At such energies, one needs to apply 1.1 kV to the Lorentz steerer in order to displace the beam by $\Delta r = 1.0$ mm. Due to the radial electric field created by the Lorentz steerer, the radial kinetic energy of the ion increases together with the radial offset of the beam. Part of this kinetic energy contributes to an increase in the cyclotron radius of the beam. Thus, once it leaves the Lorentz steerer, the radial kinetic energy of the ions does not return to the unperturbed level. In the case where the drift tube section is grounded, a large fraction of the kinetic energy gained goes into an increase of the cyclotron radius and the ion enters the Penning trap with a radial kinetic energy of 80.3 eV. Floating the injection drift tube section at +4.5 keV decreases the axial kinetic energy of the beam from 5 keV to 500 eV. Thus the voltage offset ΔV_{steer} that one needs to apply on the steerer to shift the beam by the same amount is lower. A $\Delta V_{steer} = 0.35$ keV allows one to shift the beam by 1.0 mm while the radial kinetic energy increases by only 0.3 eV. Furthermore, Table 2.4 also shows that floating the drift tube 4.5 keV above ground has a minuscule impact on the final kinetic energy and dimensions of the beam. Figure 2.18 shows that the Lorentz steerer displaces the beam spots without changing the beam spot dimensions.

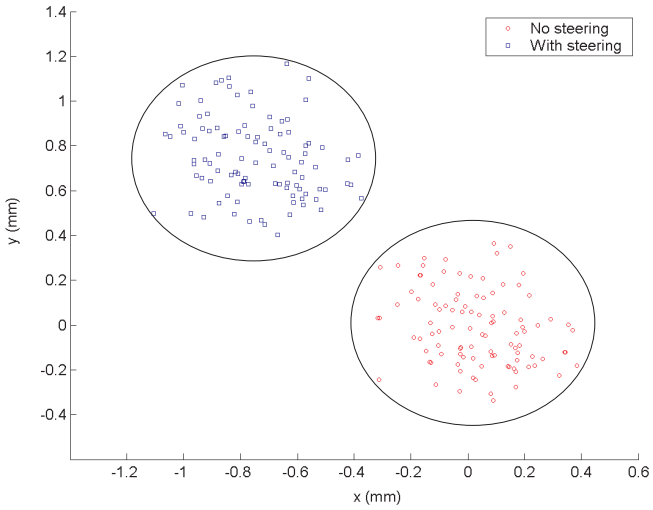

Figure 2.18: Simulation of the displacement of the beam spot entering TITAN's Penning trap. The circles represent the 0.8 mm

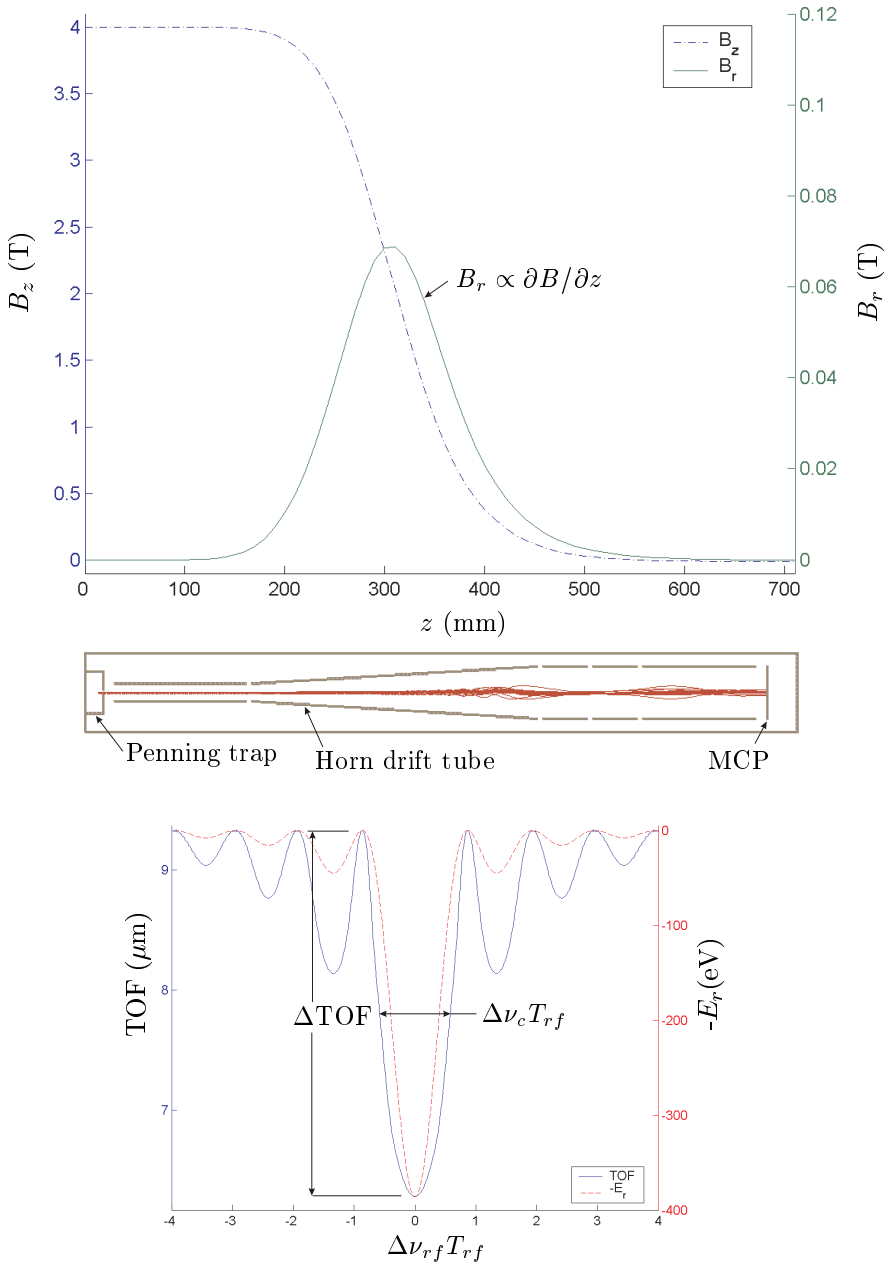

Figure 2.19: Schematic of the extraction electrode structure together with the variation of the magnetic fields B_r and B_z. The lower panel show a schematic TOF spectra together with the radial kinetic energy E_r of the ions before extraction from the Penning trap. See text for more details.

2.2.5 Extraction optics for the Penning trap

The extraction of the ion from the mass measurement Penning trap is an important part of the TITAN experiment. In a mass spectrometry experiment using Penning trap, the mass is determined from the measurement of the cyclotron frequency of the ion in the trap. This cyclotron frequency is measured using the so-called time-of-flight (TOF) technique. The ions are electrostatically extracted from the Penning trap and fly in the magnetic fringe field of the 4 T superconducting magnet where the coupling of their magnetron moment $\mu(\omega_{rf})$ with the magnetic field gradient convert their radial kinetic energy in axial kinetic energy, as explain in Section 1.4.2. Thus, the ions with the highest initial radial kinetic energy will spent less time in the magnetic fringe field. The TOF of the ions is recorded by a Micro-Channel Plate (MCP) detector situated downstream of the Penning trap, as shown in Figure 2.19.

A schematic TOF spectra together with the initial radial kinetic energy E_r of the ion is also shown in Figure 2.19. The dimensionless quantity $T_{rf} \cdot \Delta\nu_{rf} = T_{rf} \cdot (\nu_{rf} - \nu_c)$ is the product of the difference between the excitation frequency ν_{rf} and the cyclotron frequency ν_c with the excitation time T_{rf} spent by the ion in the Penning trap. The cyclotron frequency is determined by an excitation frequency ν_{rf} scan near the expected position of the cyclotron frequency ν_c resonance. Note the broadening of the central peak and the enhancement of the secondary peaks of the TOF spectra compared to the E_r spectra in Figure 2.19. This is due to the non-linearities in the conversion of the radial energy into axial energy [Kon95]. The broadening of the central decrease the resolving power R on the cyclotron frequency ν_c measurement:

$$R = \frac{\nu_c}{\Delta\nu_c}, \tag{2.11}$$

where the line width $\Delta\nu_c$(FWMH) is define at the Full Width Half Maximum of the central peak. The resolving power is related to the uncertainty on the mass measurement (Eq. (2.2)) by:

$$\frac{\delta m}{m} = \frac{1}{R\sqrt{N}}, \tag{2.12}$$

where N is the total number of ion recorded in the resonance. In order to achieve a mass measurement with very low uncertainty, a minimized line width is very important. Therefore, the main goal of the extraction optics from the mass measurement Penning trap is to maximize the resolution on the resonance peak.

Figure 2.19 shows a schematic of the electrode structure from TITAN's Penning trap. As it is shown, the position of the horned drift tube correspond to the region where the gradient of the magnetic field is the highest and because of that, the extracted ions will gets the highest TOF effect inside the horned drift tube.

Therefore, simulations were carried out to observe the effect of varying the potential V_{horn} of the horned drift tube on the TOF spectra. The two quantities measured in the simulations are the dimensionless line width at full width

Table 2.5: Variation of the width $\Delta\nu_c T_{rf}$ of the cyclotron frequency resonance and the amplitude of the resonance ΔTOF with the horned drift tube section potential V_{horn}.

V_{horn} (V)	$\Delta\nu_c T_{rf}$	ΔTOF (μs)
-30	1.12	2.8
-20	1.20	3.7
-10	1.24	5.7
0	1.48	24.7

half maximum $\Delta\nu_c T_{rf}$ and the amplitude of the resonance peak ΔTOF. Both parameters are shown in Figure 2.19. In the simulation, ion of mass $m = 2$ u and charge $q = 1$ e (giving a typical HCI m/q-ratio of 2) were extracted from the Penning trap into the electrode structure shown in Figure 2.19. The ions had an initial radial kinetic energy given by:

$$E_r = E_0 \frac{\sin^2(\frac{\pi}{2}\sqrt{(2\Delta\nu_{rf}T_{rf})^2+1})}{(2\Delta\nu_{rf}T_{rf})^2+1}, \tag{2.13}$$

where E_0 is the radial kinetic energy at the cyclotron frequency resonance:

$$E_0 = \frac{(qBr_0)^2}{2m}. \tag{2.14}$$

The initial radial position of the ion was $r_0 = 1$ mm, a typical radial position of an ion inside a Penning trap and $B = 4$ T, is the magnetic field produced by TITAN's superconducting magnet. Keeping a constant potential on the other electrodes, the potential applied on the horned drift tube was varied from -30 V up to 0 V.

Table 2.5 shows the results of this simulation. The applied potential on the horned drift tube affect both $\Delta\nu_c T_{rf}$ and ΔTOF. This is because varying the potential applied on the horned drift tube will affect the velocity of the ions inside the region of strong magnetic field gradient. The work W made on the ion due to the axial force (1.58) that convert the radial kinetic energy into axial kinetic energy is:

$$W = \int \vec{F}\cdot\vec{v}dt = \mu(\omega_{rf})\int \frac{\partial B(z)}{\partial z} v(z,t)dt, \tag{2.15}$$

where $v(z,t)$ is the axial velocity of the ion inside the horned drift tube. From Eq. (2.15), since an ion of reduced velocity will spent more time inside the strong magnetic field gradient, the conversion of its radial kinetic energy into axial kinetic energy will be increased. Thus, decreasing the potential $|V_{horn}|$ increase the amplitude ΔTOF of the central peak. Also, as the ion spent more time in the magnetic field gradient, the non-linearities in the radial kinetic energy conversion are increased and this causes a broadening of the resonance peak, thus a larger $\Delta\nu_c T_{rf}$ [Kon95]. The broadening of the central peak as $|V_{horn}|$

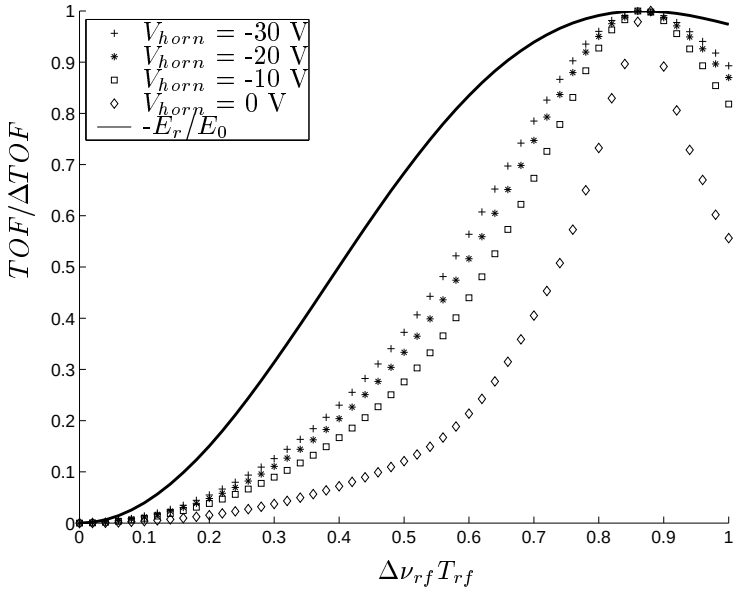

Figure 2.20: Variation of the normalized time-of-flight of $m/q = 2$ ions with $\Delta\nu_{rf}T_{rf}$. The normalized TOF spectra is shown for different applied voltage V_{horn} on the horned drift tube as well as the normalized radial kinetic energy of the ion leaving the trap.

decrease is illustrated in Figure 2.20. This figure shows the normalized time-of-flight spectra ($TOF/\Delta TOF$) of the different cases tabulate in Table 2.5, plus the spectra of the normalized radial kinetic energy (E_r/E_0) of the ion leaving the trap. Note the strong non-linear effects present when $V_{horn} = 0$ V.

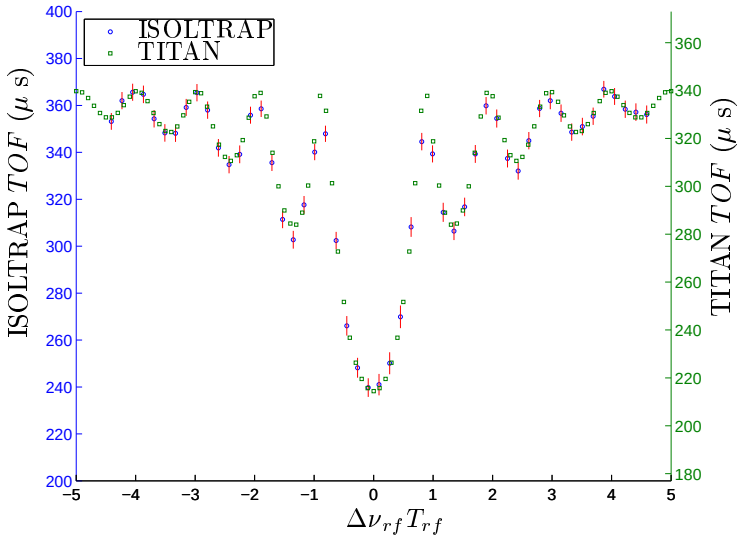

Figure 2.21: Comparison of a simulated TITAN $^{85}Rb^{+}$ TOF spectrum and an experimental TOF spectrum of the ISOLTRAP experiment. The two spectrum have a similar resonance amplitude $\Delta TOF = 125$ μs, but are shifted from each other by 25 μ s, for explanation see text.

In order to test the flexibility of TITAN's Penning trap extraction electrode structure, an observed TOF spectra from the ISOLTRAP experiment [Bla06] was successfully simulated. Figure 2.21 compares the simulated TOF spectra of $^{85}Rb^{+}$ from the TITAN experiment extraction with the corresponding TOF spectra measured at the ISOLTRAP experiment. Both spectra have the same resonance amplitude $\Delta TOF = 125$ μs and width $\Delta\nu_{rf}T_{rf} = 1.22$. But the two spectra are shifted by 25 μs, there can be several cause to such shift, like; different lengths in the extraction system or different accelerating potentials applied on the drift tubes. Assuming that the ions in TITAN's Penning trap and undergoes the same excitation period $T_{rf} = 900$ ms as the ISOLTRAP experiment, the resolving power on the cyclotron frequency of $^{85}Rb^{+}$ is:

$$R = \frac{\nu_c}{\delta\nu_c} = \frac{qB}{2\pi m}\frac{1}{\Delta\nu_c} = 5.3 \times 10^5 \tag{2.16}$$

For the same singly charged ^{85}Rb, the ISOLTRAP achieve a resolving power of $R = 7.9 \times 10^5$. The difference being caused by the stronger 6 T magnetic field

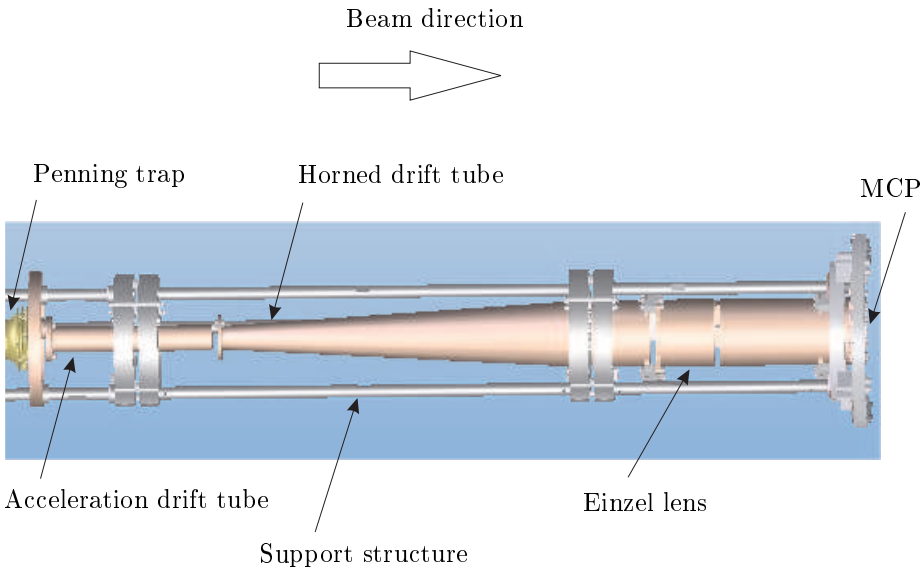

Figure 2.22: Rendered design drawing of the electrode structure for the extraction from the TITAN's mass measurement Penning trap. Shown are the different drift tube section, the Einzel lens, the Penning trap, the MCP and the support structure.

produced by the ISOLTRAP's magnet. On the other hand, the use of HCI will increase the resolving power of the TITAN experiment by a factor of q.

Finally, a description of the extraction optics electrode structure, shown in Figure 2.22, is given. The extraction optics is divided in three parts: The extraction optics electrode structure is divided into three parts:

- A 16 mm inner diameter 130 mm long drift tube accelerates the ion while they are in the strong magnetic field region, i.e. when B is close to 4 T. Since the magnetic field gradient in this region is small, no radial kinetic energy change occurs. Thus, no significant effect on the time-of-flight spectra can be achieved by varying the drift tube potential. Accelerating the ion through the strong field region has the advantage of reducing the flight time and thus the total time required for the frequency scan. Long frequency scans induce larger systematic errors on the TOF spectra due to time dependant variables such as drift of the magnetic field as describe in Section 3.2.

- A horned drift tube encloses the region with the highest magnetic field gradient. Compared to the previous drift tube section, the potential of the horn is closer to ground. The voltage applied on the horn modifies the amplitude and width of the cyclotron frequency resonance.

- The last drift tube section is in three parts, in order use to be used as an Einzel lens that focuses the diverging beam onto the 16 mm diameter micro-channel plate (MCP) detector situated at the end of the tube.

2.3 Status of the Penning trap

At the center of a Penning trap lies the electrode structure that generates the harmonic quadrupole potential. Together with the magnetic field, this generates the three-dimensional trapping of the ion as discussed in Section 1.4.1.

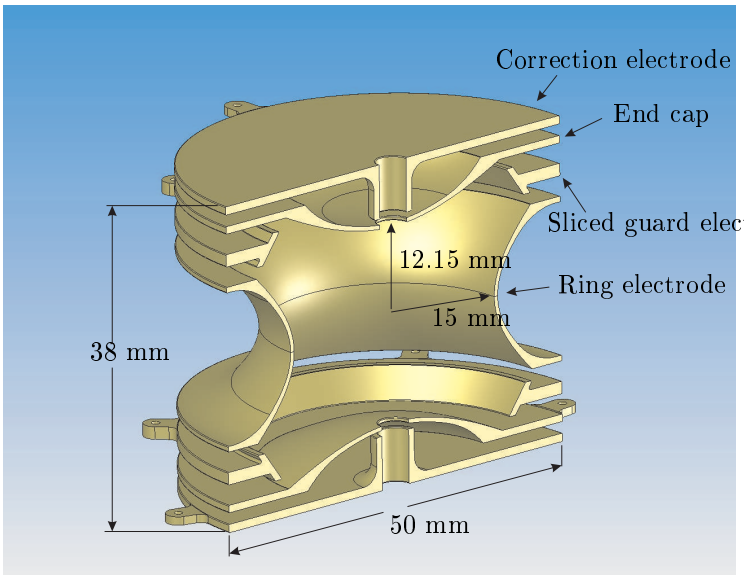

Figure 2.23: Cross-sectional view of a rendered drawing of TITAN's precision Penning trap electrode structure. Shown are the correction and guard electrodes, the ring and the end caps, together with the dimensions of the trap.

Figure 2.23 shows a rendered design drawing of TITAN's precision Penning trap electrode structure. Two important features are shown; first, two corrections electrodes corrected the perturbations cause by the entrance and exit holes. Second, an other kind of correction electrodes, the "guard electrodes" correct the electric field perturbations due to the finite size of the end cap and ring hyperbolic electrodes.

Any misalignment of the electrodes with the magnetic field, asymmetries in the electrodes or misalignment of the electrodes with each other cause uncertainties in the determination of the cyclotron frequency (for a detail discussion about the effect of misalignment, see [Bro86] and [Bol90]). Thus, each electrode will be precisely aligned with respect to each other with sapphire ball insulators.

The Penning trap electrodes are made of oxygen free high conductivity gold-plated copper. The gold plating prevents oxidation and outgassing. Outgassing can occur when certain types of materials are put into high vacuum: certain molecules, H_2 for example, leak out of the material at a low rate, limiting the vacuum quality. The amount of outgassing reduces exponentially as a function of time. However, if one wishes to accelerate this, one can heat the system to higher temperatures.

A novel feature of the TITAN experiment is its Penning trap vacuum chamber which made of titanium. With its outgassing rate of 6.0×10^{-13} Pa m s^{-1}, titanium has better ultra-high-vacuum properties than stainless steel (2.0×10^{-10} Pa m s^{-1}), the more common material for vacuum chamber construction [Kur03]. A choice of material with very low outgassing rate is more critical at the TITAN experiment than the other Penning trap experiments because of its use of HCI. Since most of the electronic shells of the HCI are empty, they interact more strongly with residual gas that is coming from the outgassing of the material surrounding the ultra-high vacuum.

Therefore, to reduce recombination, TITAN's beam line will need to be at high vacuum of around 10^{-8} mbar and the Penning trap at a ultra high vacuum of 10^{-11} mbar [Ryj05b].

In addition to the electric field, a strong and homogenous magnetic field completes a Penning trap. In the present case, a 4 T superconducting solenoid is used. The quadrupolar magnetic field deviations are tuned out by the used of room-temperature shim coils. The resulting magnetic field inhomogeneities are less than 0.2 ppm over the 20 mm magnet length [Ryj05b]. The superconducting magnet is cooled to cryogenic temperature using liquid nitrogen and liquid helium, while its bore is at room temperature. Hence, the vacuum vessel including the electrode structure is also at room temperature and follows the ambient temperature variations. Such fluctuations are known to lead to uncertainty in the determination of the cyclotron frequency. A systematic study of the influence of the temperature variations was carried out as part of this thesis. This was done at the existing ISOLTRAP experiment at CERN, Geneva. It was shown that theses fluctuations can be minimized by a feed-back control system that stabilized the temperature. A similar system is forseen at the TITAN experiment as well.

Chapter 3

Studies at existing Penning trap experiment

In the following sections, two studies carried out at existing and running Penning trap spectrometer system in radioactive beam facilities are described.

3.1 ISOLTRAP experiment at ISOLDE

The ISOLTRAP experiment [Bla05c] at on-line isotope mass-separator ISOLDE at CERN [Kug00] uses a combination of three ion traps to prepare radioactive ions and to measure their mass with a relative uncertainty of $\delta m/m \approx 8 \times 10^{-9}$ [Kel03], for isotopes with half-lives of 65 ms. The three traps are:

- The first trap is a Radio Frequency Quadrupole (RFQ) Paul trap for cooling and bunching the continuous ISOLDE beam.
- The second one is a a buffer-gas filled cylindrical Penning trap for the preparation and isobaric cleaning of the ion bunch.
- The last one is a hyperbolic Penning trap for the determination of the cyclotron frequency.

The setup is shown in Figure 3.1. The basic functions of ISOLTRAP's and TITAN's RFQ and precision Penning trap are very similar. The cylindrical Penning trap uses buffer-gas for cooling, hence can not be used with highly charged ions (see Section 2.1.4.). For a detailed description of this cooling Penning trap system, see [Sav91].

3.2 Magnetic field stability studies for the ISOLTRAP precision Penning trap

3.2.1 Importance of the magnetic field stability

In general, the ions inside a Penning trap have 3 eigenmotions of different frequencies: axial ν_z, reduced cyclotron ν_+ and magnetron ν_-.

As explained in Section 1.4.2, the ions mass are directly determined by the measurement of the true cyclotron frequency:

$$\nu_c = \nu_+ + \nu_- = \frac{1}{2\pi}\frac{qB}{m} \tag{3.1}$$

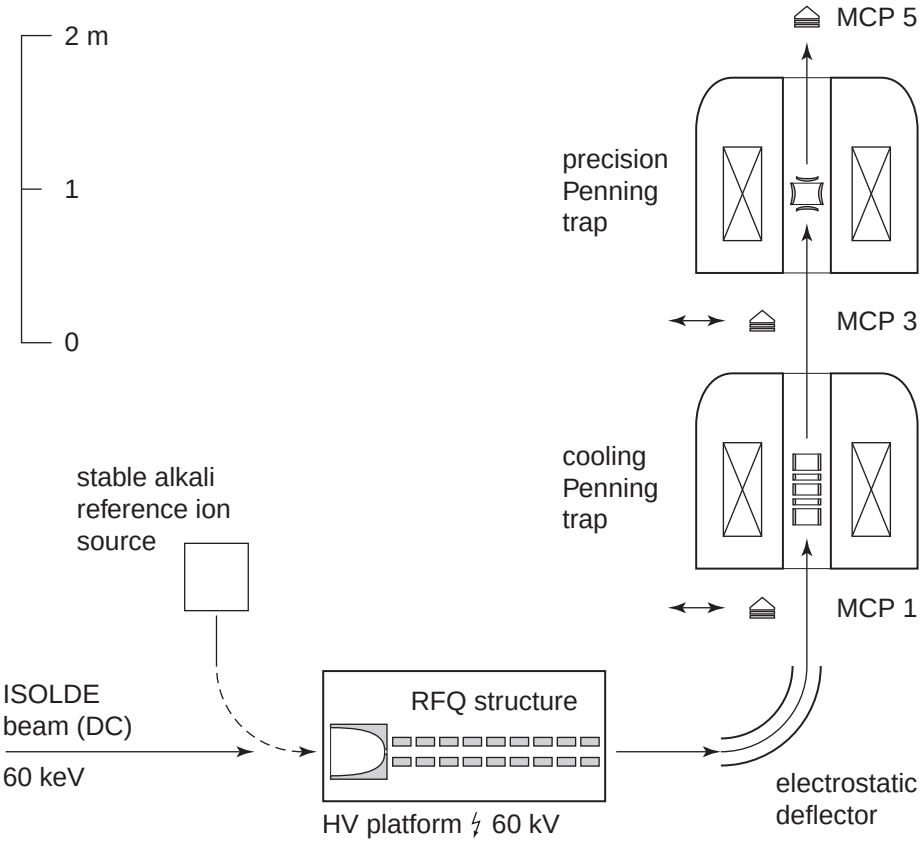

Figure 3.1: Sketch of the ISOLTRAP setup. Shown are the ISOLDE quasi-DC beam, the reference ion source, the RFQ, the cooling and the precision Penning trap. The Micro-Channel Plates (MCP) 1 and 3 are use for beam tuning, while MCP5 record the TOF of the ions.

Thus, for a constant magnetic field B and charge q, different cyclotron frequencies correspond to different masses. The magnetic field can be obtained by measuring the cyclotron frequency of a reference ion with well-known mass and the atomic mass of the ion of interest is:

$$m^{new} = \frac{\nu_c^{ref}}{\nu_c^{new}}(m^{ref} - m_e) + m_e, \tag{3.2}$$

where m_e is the electron mass, and ignoring the atomic binding energy. But since the two measurements are separated in time, relation (3.2) is only correct if the magnetic field is time independent. It was observed at ISOLTRAP

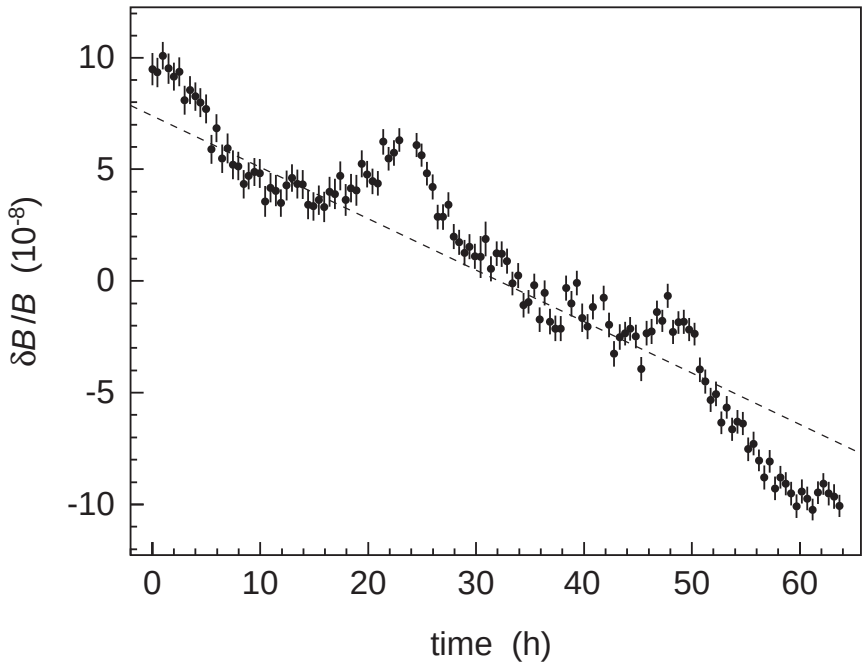

Figure 3.2: Magnetic field variations produced by the ISOLTRAP precision Penning trap 6T superconducting magnet, observed over a period of 64 hours. The short-term fluctuations correspond to day-night variations. (taken from [Kel03])

[Kel03] that the magnetic field in the measurement Penning trap linearly drifts with additional short- and long-term fluctuations (Figure 3.2). One possible explanation for this effect is the fluctuations in the temperature of the superconducting magnet's bore. The linear magnetic field drift was determined [Kel03] as [1]: $\frac{\delta B}{\delta t}\frac{1}{B} = -2.30(3) \times 10^{-9}$ h^{-1}.

[1] A typographical error was founded in [Kel03]. Rather than the given value of -2.30(3)

Therefore, fluctuations in the magnetic field have directly affected, although on a very small scale, the experimentally measured cyclotron frequencies.

Since there is good evidence for fluctuations on the magnetic field due to the temperature, a study of the correlation between magnetic field variations and temperature variations in the magnet bore of the ISOLTRAP experiment was carried out and is shown in the following section. This was part of a systematic study of the ISOLTRAP experiment and is reported in [Bla05b].

3.2.2 Data acquisition

The magnetic field was determined from the measurement of the cyclotron frequency ν_c of ^{85}Rb and relation (3.1). The temperature was measured with a platinum resistance thermometer (PRT) which was placed in the room temperature bore of the superconducting magnet of the precision Penning trap. At room temperature, the resistance measured by the PRT varies linearly with the temperature following the empirical formula [DIN04]:

$$R = R_0[1 + \alpha T] \tag{3.3}$$

where α is the temperature coefficient $\alpha = 3.89 \times 10^{-3}\ ^\circ\mathrm{C}^{-1}$ and $R_0 = 100\ \Omega$, the resistance at $T = 0^\circ\mathrm{C}$.

3.2.3 Comparison of the resistance and cyclotron frequency variation

Time evolution of the resistance

The resistance has been measured continuously for about a week (one measurement per minute). The resistance of the PRT was measured by a Keithley multimeter (model 2000). A program was set-up to remotely control the measurement process. As expected from [Kel03], a day-night variation of the temperature has been observed. Figure 3.3 shows the variation of the resistance over the week of measurements and two dominant features are visible:

- A disturbance of the measurement due to variations of the data acquisition system.
- Cooling of the experimental setup due to the filling of the superconducting magnet with liquid nitrogen.

The disturbance in the resistance measurement were possibly caused by the motion of the loose wire connecting the PRT to the multimeter or by the motion of the multimeter it self, since they were happening when someone was working near the data acquisition system. Later, care where taken to avoid those disturbances. The magnitude of the disturbance is of the same order as the daily

$\times\ 10^{-8}\mathrm{h}^{-1}$, the correct value should have read -2.30(3) $\times\ 10^{-9}\mathrm{h}^{-1}$. This was confirmed by private communication from the author.

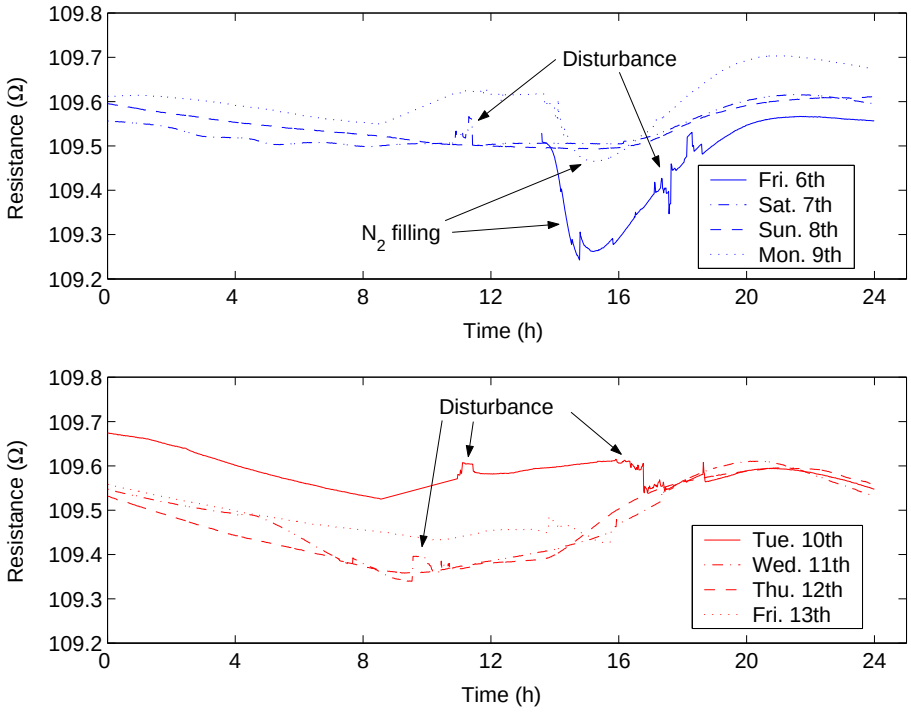

Figure 3.3: Daily fluctuation of the resistance of the PRT. Data taken between August 6th (Friday) to August 13th 2004 (Friday). The different curves corresponds to the four different days. Shown are the disturbance of the measurement possibly due to the motion of the wire connecting the PRT to the multimeter and the decrease in resistance produced by the cold vapor emit from the exhaust pipe during liquid nitrogen filling.

fluctuations. This important effect was taken into account when the data has been analyzed.

The second important effect observed is the impact of the filling of the superconducting magnet of the precision Penning trap with liquid nitrogen. The trap was filled with liquid nitrogen two times per week and with liquid helium once every 6 weeks. During the liquid nitrogen filling a decrease in the resistance of the PRT was observed. This decrease is caused by cold nitrogen vapor, that was directed to the apparatus, through an exhaust pipe. Later on, the exhaust pipe was redirected away from the experimental setup and the perturbation of the temperature became significantly smaller.

Time evolution of the cyclotron frequency

In all of the following graphs, each point represents three frequency scans. This minimizes statistical fluctuations and gives a better estimation of the frequency as a function of time. Some problems with the automatic regulation of the buffer-gas pressure in the preparation trap caused a stopping of the cyclotron frequency measurement. Thus, the cyclotron frequency of $^{85}Rb^{+}$ was measured only for short time intervals. Figure 3.4 gives all the different frequency mea-

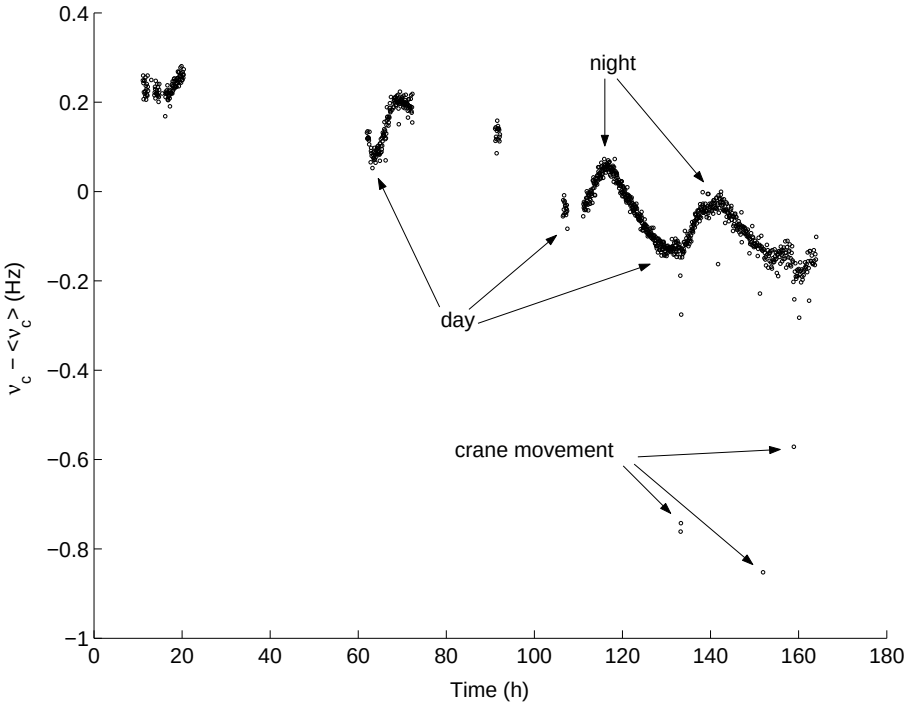

Figure 3.4: Cyclotron frequency determination of ^{85}Rb in the ISOLTRAP experiment Penning trap over a period of 160 hours. Visible are the linear drift and the so-called day-night fluctuations. In addition, decrease of the measured cyclotron frequency due to crane movement is shown.

surements that had been made within one week. There are three observed features:

- Linear drift in the frequency
- Day-night oscillations of the frequency
- A large drop in the frequency due to the movement of the bridge crane

A decrease of the cyclotron frequency had been observed when the large bridge crane was moving close to the apparatus. The experimental hall in which the experiment is located features bridge crane, which is used to transport heavy experimental equipments. This crane sits on two rails on the side of the hall, and can move across it. To determine the effect of the crane, a ten minute

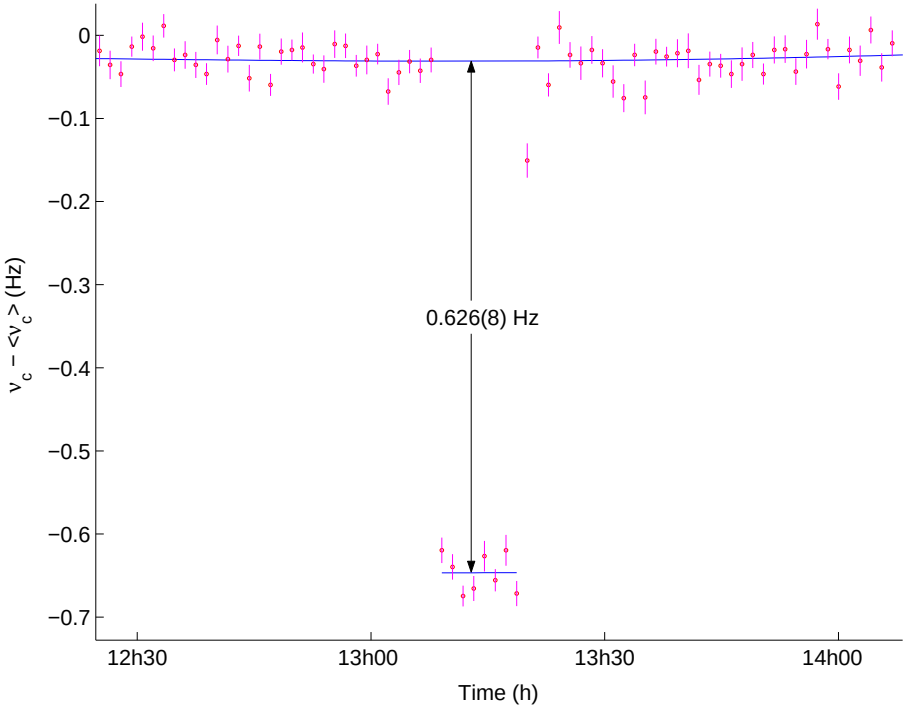

Figure 3.5: Ten minutes measurement of the cyclotron frequency with the crane straight above the Penning trap. Shown is a 0.626(8) Hz decrease in the measure cyclotron frequency.

measurement was made with the crane at 46.5 cm straight above the top of the MCP5 detector (Figure 3.1), hence about one meter above the precision Penning trap magnet (Figure 3.5). The frequency shift with respect to the previously determined cyclotron frequency was: 0.626(8) Hz, which is in the same order of magnitude as the cyclotron frequency drift over 160 hours. Such an effect is caused by a magnetization of the ferromagnetic material in the crane. This magnetization distorted the magnetic field fringe lines of the magnet causing a decrease of the magnetic field in the region of the trap [Kel03]. All points with large deviations from the general behavior of the cyclotron frequency (like the ones described above) were not taken into account for the evaluation of the linear drift.

In order to quantify the cyclotron frequency drift, it has been computed by a linear regression fit routine. The equations of the fitting function is:

$$\nu_c = mt + b_i \tag{3.4}$$

$$m = \frac{\partial \nu_c}{\partial t} = -2.84(5) \times 10^{-3} \text{ Hz h}^{-1} \tag{3.5}$$

$$b_1 = \nu_c(0) = 1069831.124(6) \text{ Hz} \tag{3.6}$$

$$b_2 = \nu_c(0) - <\nu_c> = 0.315(6) \text{ Hz} \tag{3.7}$$

The relative magnetic field drift is deduced to be:

$$\frac{1}{B}\frac{\partial B}{\partial t} = \frac{1}{\nu_c}\frac{\partial \nu_c}{\partial t} = \frac{m}{b_1} = -2.65(4) \times 10^{-9} \text{ h}^{-1} \tag{3.8}$$

This result correspond to a deviation of 8.75σ from the previous result [Kel03]. The Author of [Kel03], gave two others results from cyclotron frequency measurement at the ISOLTRAP experiment; a Kr run where they found a drift of: -3.1 $\times$ 10^{-9} h^{-1} and an other Rb run where the drift was: -2.4 $\times$ 10^{-9} h^{-1}. An average of the three results from the Author of [Kel03] (assuming an equal uncertainty as the result in [Kel03]), gives a magnetic field drift of:

$$\frac{1}{B}\frac{\partial B}{\partial t} = -2.60(5) \times 10^{-9} \text{ h}^{-1}, \tag{3.9}$$

which is in good agreement with the result found in Eq. (3.8). The deviation from the previously published result will be addressed in a following publication.

The magnetic field drift could be caused by a flux creep which reduces the current in the superconducting coil and subsequently, the magnetic field decreases with time [Kel03]. With the known linear magnetic drift, the next step is to check if the magnetic field and temperature oscillations are correlated.

Determination of the cyclotron frequency/temperature ratio

In order to compare the oscillation of the cyclotron frequency and the resistance, one first subtracts the independent linear drift of the cyclotron frequency. It is convenient to decompose the cyclotron frequency variations into a product of two functions:

$$\nu_c(t) = f(t) \cdot g(t), \tag{3.10}$$

where $f(t)$ is a function that oscillates with time and $g(t)$ is a function of the drift $\frac{\partial \nu_c}{\partial t}$:

$$g(t) = \frac{\partial \nu_c}{\partial t} \cdot t + \nu_c(0). \tag{3.11}$$

The behavior of $f(t)$ is found by dividing the cyclotron frequency data by the function $g(t)$ found in the previous section. Now, one can compare the cyclotron frequency and resistance fluctuations. Since only small variations of the frequency ν_c and the resistance R are measured, it is more convenient to plot

the deviation at each data point: ν_c - 1069831.0 Hz and R - 109.0 Ω. The ratio of the cyclotron frequency over the temperature variation is given by:

$$\frac{\Delta\nu_c}{\Delta T} = \frac{\Delta\nu_c}{\Delta R}\frac{\Delta R}{\Delta T}, \tag{3.12}$$

and using (3.3),

$$\frac{\Delta R}{\Delta T} = \alpha R_0 = 0.389\ \Omega\ {}^{\circ}\mathrm{C}^{-1} \tag{3.13}$$

In Figure 3.6, the absolute change of the cyclotron frequency with the drift

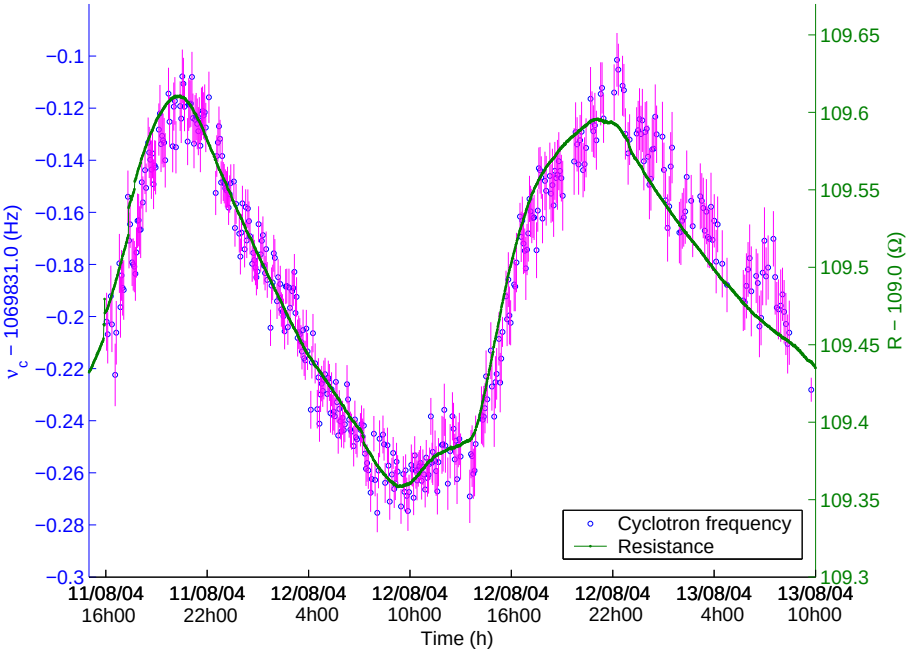

Figure 3.6: Comparison of the resistance measured by a PRT in the ISOLTRAP's Penning trap magnet bore with the cyclotron frequency of ^{85}Rb measured during the same period of 160 hours. The cyclotron frequency drift was corrected using (3.10) and (3.11). Both data sets present the same day-night fluctuations.

correction and the change of resistance are plotted. This graph shows that the day-night variation of the magnetic field and the temperature fluctuation inside the magnet bore have the same behavior. Figure 3.7 shows the magnetic field drift as a function of time. The effect is visible already in periods of only a few days.

The correlation between the temperature and the magnetic field fluctuation can be verified by plotting one of them as the function of the other. The

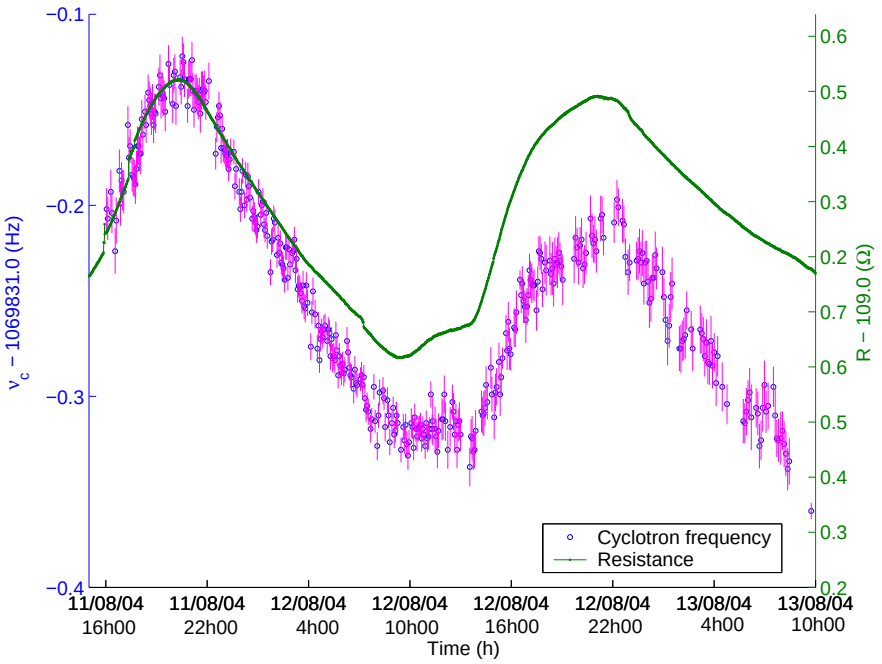

Figure 3.7: Comparison of the resistance measured by a PRT in the ISOLTRAP's Penning trap magnet bore with the cyclotron frequency of ^{85}Rb measured during the same period of 160 hours. The deviation between the two curves is made by the linear drift of the magnetic field of the Penning trap superconducting magnet that cause a drift in the cyclotron frequency as shown.

cyclotron frequency will be assume to be a polynomial function of the resistance:

$$\nu_c(t) = f(R(t)) = a_0 + a_1 R + O(R^2) \tag{3.14}$$

$$\frac{\partial \nu_c}{\partial R} = a_1 + O(R). \tag{3.15}$$

If the magnetic field varies linearly with the temperature, the derivative (3.15) should be constant (a_1). One way to see this, is to perform a linear fit using the least-square method. In Figure 3.8, the cyclotron frequency was plotted as a function of the resistance to illustrate the correlation between the cyclotron frequency and the resistance. The slope and the y-intercept of the linear regression

$$\nu_c(R) = a_1 R + a_0 \tag{3.16}$$

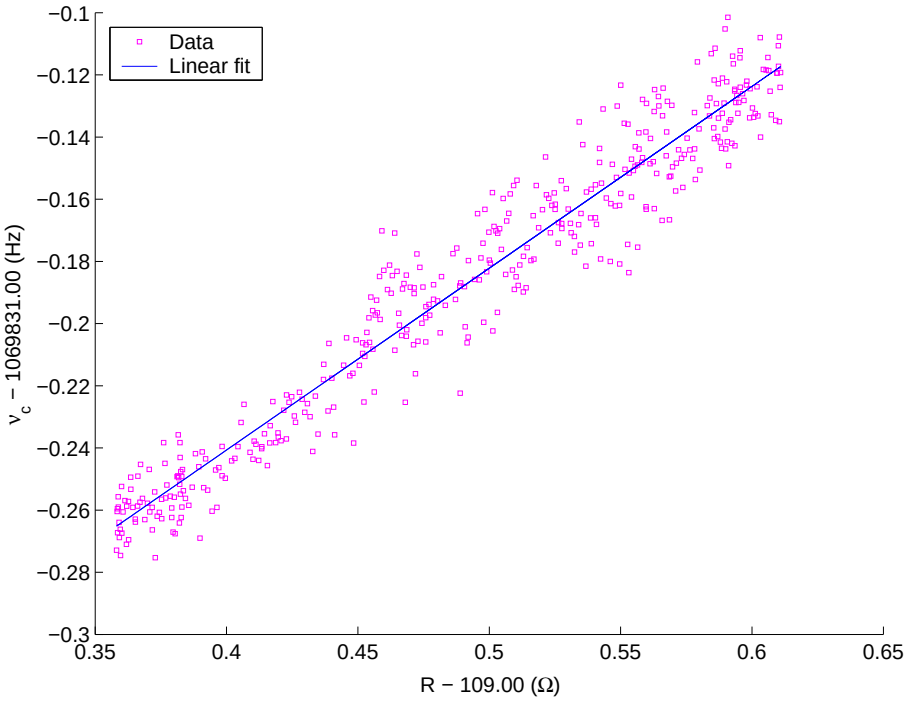

Figure 3.8: Cyclotron frequency ν_c as a function of the resistance R.

in are found as:

$$a_1 = \frac{\Delta\nu_c}{\Delta R} = 0.585(7) \text{ Hz } \Omega^{-1} \tag{3.17}$$

$$a_0 = -0.475(4) \text{ Hz} \tag{3.18}$$

The reduced chi-square of the first 202 data points is:

$$\chi^2/\nu = 1.51 \tag{3.19}$$

The probability to exceed this χ^2/ν value is less then 0.1%, which means that the linear regression (3.16) is an accurate representation of the $\nu_c(t) = f(R(t))$ data set [Bev92].

Figure 3.8 shows the frequency ν_c as a function of the resistance. It can be seen how much the cyclotron frequency changes for different values of the resistance. The standard deviation of the cyclotron frequency along the linear fit

$$\nu_c(t) = \nu_c(0) + \frac{\partial\nu_c}{\partial R} \cdot R(t) \tag{3.20}$$

is 1.14×10^{-2} Hz. This number illustrates the statistical fluctuations of the cyclotron frequency with the temperature. With (3.13) and (3.17), the cyclotron

frequency variation with the temperature is:

$$\frac{\Delta\nu_c}{\Delta T} = \frac{\Delta\nu_c}{\Delta R}\frac{\Delta R}{\Delta T} = 0.228(3)\ \text{Hz}\ ^\circ\text{C}^{-1} \tag{3.21}$$

Finally, the variation of the magnetic field B with the temperature T for $^{85}\text{Rb}^+$ is:

$$\frac{\Delta B}{\Delta T} = \frac{\Delta\nu_c}{\Delta T}\frac{\Delta B}{\Delta\nu_c} = 2\pi\frac{m}{q}\frac{\Delta\nu_c}{\Delta T} = 1.26(2)\times 10^{-6}\ \text{T}\ ^\circ\text{C}^{-1}, \tag{3.22}$$

where $m(^{85}Rb) = 84.9117893(25)$ amu [Bra99] and ΔT is the day-night magnet bore temperature fluctuation. Table 3.1 summarizes the different values found

Table 3.1: Parameters of the temperature and frequency variations

$\Delta B/\Delta T$	1.26(2) $\times 10^{-6}$ T $^\circ$C^{-1}
$\frac{1}{B}\frac{\delta B}{\delta t}$	-2.65(4) $\times 10^{-9}$ h^{-1}
ΔT	0.65 $^\circ$C
σB	6.28×10^{-8} T

in this section.

In conclusion, a strong correlation between the magnetic field and temperature variations was founded as well as a steady linear drift of the magnetic field. Effects that have to be taken into consideration in a later analysis are: Movements of the PRT wire or the GPIB device causes variations in the measured resistance, therefore the GPIB device and connecting wire should be put to a place where they can not be affected. The exhaust pipe for the nitrogen filling should be pointed opposite to the trap, because it will reduce the temperature surrounding the trap. Crane movement decreases the cyclotron frequency by a significant amount, thus long stops of the crane near the apparatus should be avoided and the corresponding data points should be remove from analysis.

Considering those points, more precise measurements of the temperature and cyclotron frequency variation should be conducted in the future. The use of a device which can regulate the temperature fluctuations inside the bore of the superconducting magnet, which has already shown its impact in other experiments [Fri01] should be considered, example of such device are given in Section 3.5. The implementation of such system is planned for the TITAN set-up.

3.3 The CPT experiment at ATLAS

Additional studies where carried out at another on-line Penning trap mass spectrometer, the Canadian Penning Trap (CPT). The CPT is located at the Argonne National Laboratory (ANL) in the USA. A brief description is given in the following, for more details see [Cla05].

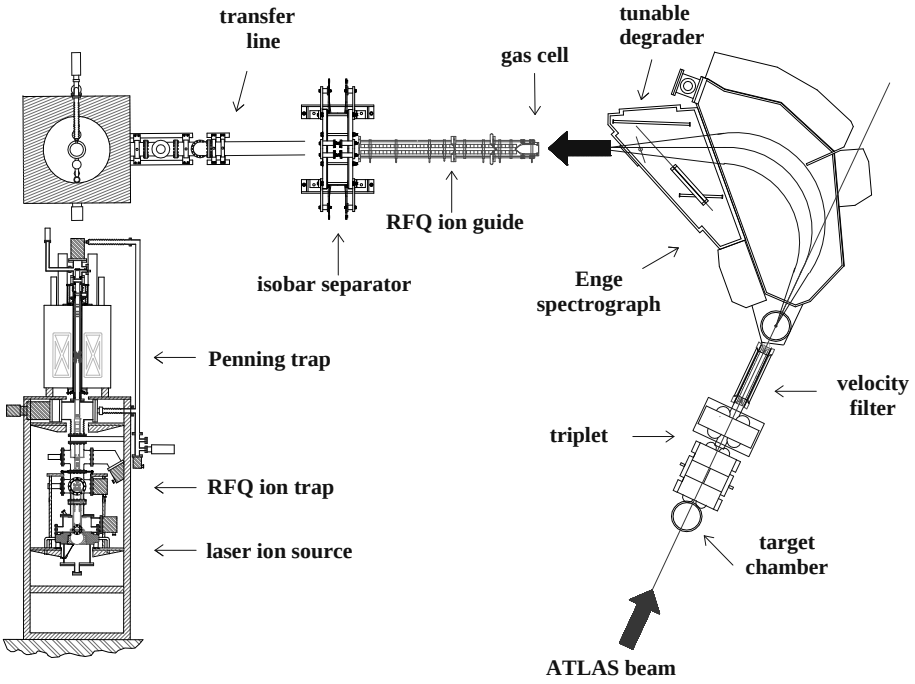

Figure 3.9: The Canadian Penning trap experimental setup together with beam production, stopping and separation system (from [Cla05]).

The setup of the CPT experiment is shown in Figure 3.9. At the entrance of the CPT experiment, the 8-17 MeV/A stable heavy ion beam produced by the Argonne Tandem Linac Accelerator System (ATLAS) hits a thin target. The radioactive nuclei are produced by fusion-evaporation reactions. In such reactions, the heavy ions from the incoming beam collide with the nuclei of the target producing several different new nuclei.

Due to momentum conservation, the products also move forward in the beam direction. The radioactive beam then needs to be cleaned from undesirable species and efficiently transferred to the measurement system. After the target, a magnetic quadrupole triplet focus the radioactive beam at the entrance of a spectrograph.

After the quadrupole triplet, a velocity filter separates the primary beam from the radioactive nucleus products. In the CPT experiment, the velocity filter is used to deflect the primary beam away from the Enge entrance.

An Enge is a split pole spectrograph made of two magnetic dipoles that allows one to focus ions with a specific magnetic rigidity $B\rho$ [Spe67]:

$$B\rho = \frac{p}{q}, \tag{3.23}$$

where B is the magnetic field, ρ is the bending radius of the ions, q is their charge and p their momentum. The spectrometer is used to decrease the number of nuclei of undesired species that are transmitted to the next component, the gas catcher [Mai01].

Since the gas catcher can only effectively cool ions with energies lower then 3 MeV, so-called degrader are placed before the gas catcher which decrease the energy of the radioactive beam. Degraders are made from a series of aluminium foils of different thicknesses, or stopping powers, mounted on a movable ladder structure. The thickness can be adapted to the energy of the incoming beam.

The gas catcher stops the energetic beam by thermalization with high purity helium gas. Once stopped in the cell, the ions are extracted through a nozzle using combination of gas pressure gradient and electric field. Radio-frequency excitation applied to the gas catcher walls radially confines the ions [Sav05b].

The ion cooler allows the transport the ions from the gas cell to the high vacuum (HV) beam line. The beam cooler is a linear RF trap, similar to the TITAN RF cooler and buncher. The ion cooler is segmented into three sections with different helium pressures. It allows to gradually decrease the pressure close to the high vacuum beam line. The electrode structure of the ion cooler is made of four rods longitudinally segmented. Therefore, the last section can be used as a linear Paul trap to cool and bunch the ions.

The next component is a cylindrical Penning trap that is used as an isobar separator, removing contaminants coming from the gas catcher. For a detail description of an isobar separator, see [Sav91]. Before entering the mass measurement Penning trap, the ions are prepared in a linear Paul trap. This trap basically acts as a "buffer" that cools and accumulates the ion bunches coming from the transport beam line. It allows to produce pulses of equal length that

are sent into the mass measurement Penning trap at constant interval independently to the properties of the bunches prior to their injection in the Paul trap. Finally, the ions enter the precision Penning trap, where the mass measurement takes place using the TOF method, as discuss in Section 1.4.2.

3.4 Design of an off-line calibration laser ablation ion source for the CPT experiment

This section gives motivation and the design of a laser ablation ion source for the CPT.

3.4.1 Motivation for a calibration laser ablation ion source

The purpose of this source is to produce stable ions for off-line mass measurements. A laser ion source is versatile and allows the production of a variety of elements. The first ion species required is ^{26}Mg. ^{26}Mg can be produced by the β-decay of the meta-stable ^{26m}Al:

$$^{26m}\mathrm{Al} \rightarrow ^{26}\mathrm{Mg} + e^+ + \nu_e. \tag{3.24}$$

This is one of the 12 best known $0^+ \rightarrow 0^+$ super-allowed beta decays [Har05] which Ft-value enters in the calculations of the average Ft-value, from which the V_{ud} element of the CKM matrix is calculated (refer to Section 1.2.2 for details). The Ft-value of $0^+ \rightarrow 0^+$ super-allowed beta decay transitions depends on the Q-value, which can be derived from the parent-daughter mass difference:

$$Q = m(^{26m}\mathrm{Al}) - m(^{26}\mathrm{Mg}) - 2m_e. \tag{3.25}$$

Therefore, a precise determination of the mass of ^{26}Mg and ^{26m}Al will put better constrains on the determination of the V_{ud} matrix element and ultimately on the unitarity of the CKM matrix. The mass of ^{26m}Al was measured by the CPT experiment. During this on-line measurement, the numbers of ^{26}Mg produced by the decay (3.24) were too small for a ^{26}Mg mass measurement. But since ^{26}Mg is a stable nuclei, a beam can be easily produced off-line. Thus, an off-line ion source was designed as part of this thesis and is described in the following. It is currently under construction and will after completion be included in the CPT set-up. The source will produce stables ions by laser ablation using an Nb: YAG laser. The next section gives an overview of the ion source.

3.4.2 Overview of the ion source

In a laser ablation ion source, a pulsed laser beam is directed onto a thin solid target through a series of optical devices. The energetic photons from the laser beam removes electrons and some ions from the target surface. This creates an electron-ion plasma that expands outward from the target surface. This plasma

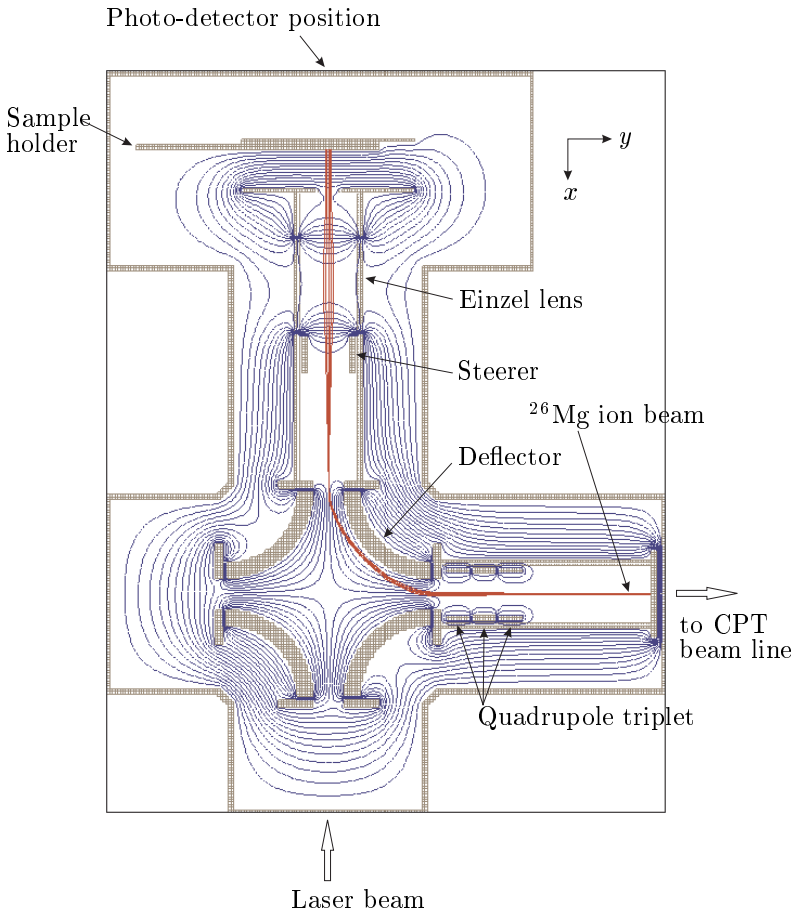

Figure 3.10: Schematic cross-section view of the CPT ion source. The electrode structure are showed along with the corresponding equipotential lines and a $^{26}Mg^{+}$ ion beam.

is confined between two plates at different potential. The electric field between the plates accelerates the positive ions towards a drift tube. Afterwards, the ion beam is focused by an Einzel lens. The choice to produce the stable ions by laser ablation mainly comes from the versatility of such system. Figure 3.10 shows the cross-section view of the CPT ion source. Before going into the discussion about the ion source electrode structure, some characteristics of the laser uses are given.

The ion source uses a pulsed Nb: YAG laser that emits pulses of 5 ns durations at 532 nm every 20 s. Each laser pulse has a maximal energy of 165 mJ [Fuk00]. The laser beam enters the ion source system through a window after being deflected by a prism.

Laser ablation is a complex process where the efficient production of ions depends also on the specific tuning of the laser beam. For example, too short times between each laser pulse will deposit too much energy in the target and increase the temperature of the plasma. Due to their high mobility, the thermal motion of the electrons will screen the electric potential, e.g. most of the produced ions will recombine and the source will produce a beam of neutral atoms. Thus, it is important to leave enough relaxation time between each pulse to decrease the thermal motion of the electron. It is possible to tune of the pulsed laser such that one can produce ion pulse of less than 1 eV energy spread.

Simulations were made to find a geometry that will allows to extract efficiently a pulsed beam, as produced by laser ablation, into the existing CPT beam line. Figure 3.9 shows the placement of the ion source in the existing system. The critical point in this laser ablation ion source, is to efficiently transport a clean and single-species pulsed beam out of the source without contaminating the CPT transport beam line. As previously mentioned, laser ablation process can lead to the production of a beam of neutral atoms. The reason for "L"-shaped configuration of the source, is to avoid such neutral atoms from coming in the CPT system. Depending on the potential applied on the deflector, only the desirable charge state will get out of the source. Each component of the source will be explain in details in the following. The simulation shown assumed that the ion were produced by laser ablation. The simulation were intend to find a geometry that optimizes the extraction of ions produced in such source most efficiently. Five equal distant $^{26}Mg^{+}$ ions were produced within a radius of 1.4 mm along the line $z = y$ (see Figure 3.10) with an initial beam energy of 1 eV. These initial conditions allow us to compare the behavior of the beam in the X-Y and Y-Z planes. The ions are assumed to be produced at the ground potential sample holder surface (A in Figure 3.11).

At a distance of two 37 mm, a plate (B in Figure 3.11) at a potential of -1.49 kV accelerates the produced ions into the -1.49 kV drift tube section through a 25 mm diameter aperture in the accelerating plate. There are three reasons for the accelerating electric field; first, the electric field allows for a charge separation between the electron cloud and the ions, preventing an expansion of the electrons cloud. Second, accelerating the ions increase the quality of the beam by decreasing the angular spread of the ions. Third, since the potential of CPT transport beam line is already at -1.49 kV, accelerating the produced

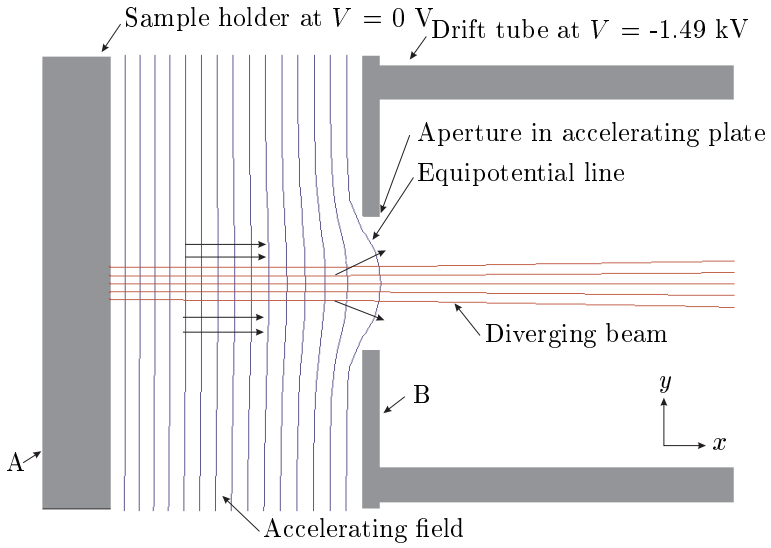

Figure 3.11: A parallel beam of 1 eV $^{26}Mg^{+}$ ions passing through an aperture at higher potential is diverged by the non-parallel equipotential line. (A) shows the grounded plate while (B) shows the -1.49 kV plate that accelerate the ion toward the drift tube. The arrows shows the direction of the electric field.

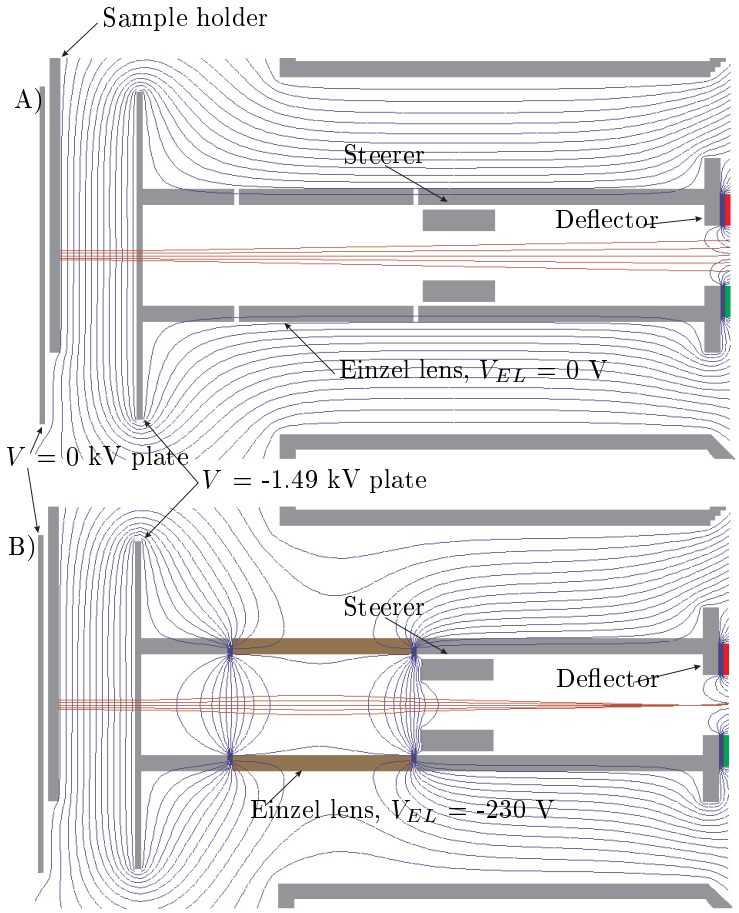

Figure 3.12: CPT ion source Einzel lens. A) Without any Einzel lens, the beam entering the deflector has too large of a size which results in an improper deflection. B) An Einzel lens focuses the diverging beam at the deflector entrance situated 25 cm from the sample holder. In blue are the equipotential lines.

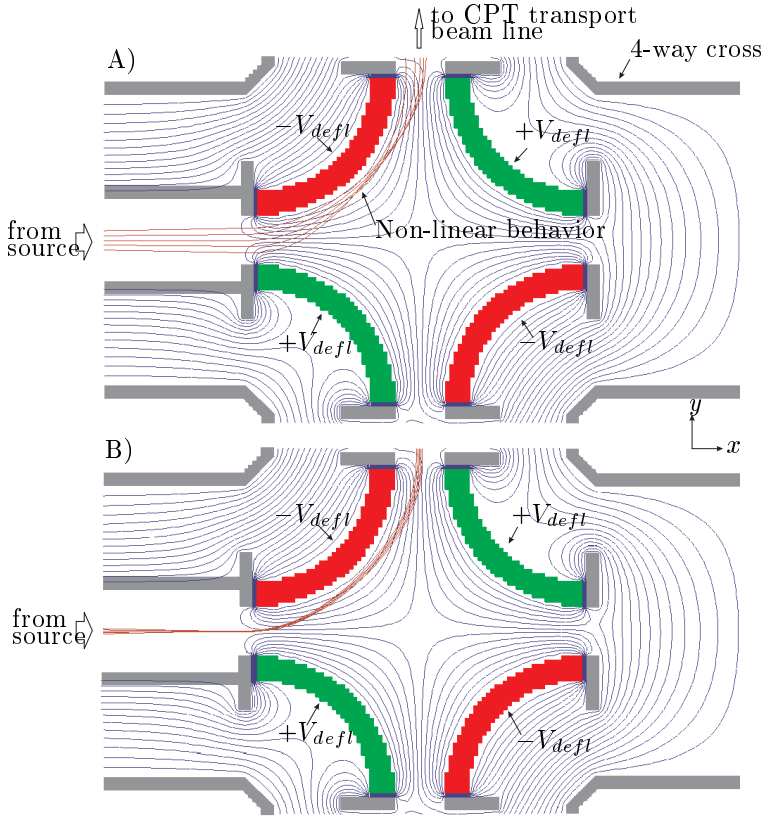

Figure 3.13: CPT ion source deflector. A) Without the Einzel lens, the wide beam entering the deflector is subjected more to a non-linear deflection and exits the deflector with a large angular spread. B) The beam size entering the deflector is reduced by an Einzel lens, leading to an on-axis exit of the deflected beam. In blue are the equipotential lines.

ions with at this potential avoid to used a pulsed drift tube to extract the ion from the source, simplifying the procedure. A deformation in the equipotential lines is caused by the aperture. The electric field present between the two plates penetrates through the aperture where it causes the beam to diverge as shown in Figure 3.11. This non-negligible divergence of the beam made by the aperture results in a large 14 mm beam spot at the deflector entrance. Therefore, two scenarios were simulated. One with and one without and Einzel lens. This was done to check the effect of changing the size of the beam entering the deflector on the extracted beam.

Figure 3.13 shows that an unfocused beam will exit the deflector with a wider angular spread than if it is focused with an Einzel lens. The large width of the beam entering the deflector causes the ions at the beam envelop to be deflected through a greater angle then the ions in the central part of the beam. This beam is then difficult to refocus as it leaves the deflector. Such effect can be caused by the circular-shaped electrode quarter that form the deflector. In an ideal deflector, a hyperbolic electrode configuration produces a quadrupolar field which provides a radial force that deflects the ion beam by 90° around the electrodes with lower potential. But since the electrodes of this deflector are circular due to simplifications in the manufacturing process rather then hyperbolic as required for a truly quadrupolar field, the deflected ion beam will suffer from some spherical aberration. This becomes more important as the axial offset increases. Thus, using an Einzel lens will decrease the beam size as it enters the deflector, such that the effect is small and non-critical for the purpose of the source, i.e. allowing to efficiently extract the produced ions.

Therefore, in order to minimize aberration due to the size of the beam, a 7.8 cm long Einzel lens focuses the beam at the deflector entrance, as shown in Figure 3.12. This Einzel lens is centered 7.5 cm from the acceleration plate and has a potential of V_{EL}. As shown in Figure 3.13, once in the deflector, the ion beam is deflected by 90° into a drift tube section that brings it into the CPT transport beam line.

The deflected beam will be focused differently in the X-Y and Y-Z planes. This is because inside the deflector, the beam will not experience any force in z direction, in the x and y directions, the potential gradient at the entrance and exit of the deflector changes the focusing of the ion beam. This causes the beam to have different focusing in the X-Y and Y-Z planes and it can be corrected with a quadrupole triplet. The quadrupole is made of a cylindrical electrode segmented in four parts. The opposite electrodes of the quadrupole share the same potential, while adjacent electrodes have an opposite potential. This potential configuration allows us to treat the X-Y and Y-Z planes separately. A set of three quadrupoles allows one to focus the beam in both directions [Wol87].

Finally, the electrode structure of the ion source sits inside two 4-way crosses. A steerer placed at the end of the Einzel lens corrects any misalignment of the two electrode structures sections. The steerer is made of a drift tube section longitudinally sliced into four segments as shown in Figure 2.17. To steer the misaligned beam, two opposite electrodes share an opposite potential offset ΔV, while the other electrodes are at the drift tube potential V_{float}. The resulting

potential gradient steers the positive ion beam towards the electrode with the lower potential, allowing force re-centering of the beam at the deflector entrance.

In conclusion, the purpose of the ion sources in Penning trap mass spectrometry experiment is manyfold. Initially they are used to commission the system. A complete understanding and optimization is necessary before measurement with radioactive ions are pursued. In addition, systematic studies are needed to determine the extended of systematic uncertainties of the system. Moreover, once on-line mass-measurements start, the magnetic field strength has to be determined on a regular basis to allow for precise measurement. If the motivation for the mass measurement comes from Q-values determinations, it is of systematic advantage to use the stable parter of the reaction as a reference, excluding additional source of uncertainty. For all of the above reasons, well functioning ion sources are needed. Laser-ablation ion sources have the advantage of allowing a production of a wide variety of elements, hence are able to serve as calibration devices for many purposes.

3.5 Conclusions

This chapter presented two projects that were carried out at existing Penning trap experiments. The knowledge obtained from both projects will help the TITAN experiment. First, the variation of the magnetic field inside a Penning trap has a non-negligible effect on the motion of the ions inside the trap. The correlation between the temperature and magnetic field variations found at the ISOLTRAP experiment demonstrated the need to control the temperature in the cryomagnet bore. The TITAN experiment which will also have a room-temperature magnet bore, will consider using a magnetic field and/or temperature regulation system. There are two existing ways to achieve this:

1. The temperature inside the magnet bore is regulated by enclosing the bore from the outside and forcing air to circulate, creating an air current of homogenous temperature in the trap region. Such system exist and shows to maintain a temperature stability within 0.03 °C [Fri01], corresponding to a magnetic field stability of $\Delta B = 3.78(6) \times 10^{-8}$ T according to (3.22).

2. Higher stability in time of the measured cyclotron frequency can be achieved with an active regulation, where variations of ν_c less then 14 ppb within 16 hours were observed. The fact that the magnetic field and temperature variations are highly correlated can be used to regulate the Penning trap magnetic field based on a temperature probe. The probe is placed in the magnet bore and any temperature variation is corrected by changing the current of correction coils [Fri01].

Second, an off-line ion source, such as the one designed at CPT, is a very crucial device for mass measurement experiments using Penning traps. The TITAN experiment has two ions source for off-line ion production. A surface ion source can produce alkali and alkaline earth metal ions, used for the commissioning of the RFQ (with Cs^+ ions). This ion source, which is described in

detail in [Smi05], uses a similar setup as the ion source design for CPT. The main difference resides in the method of production of the ion. In a surface ion source, the ions are produced by a thermionic emission process; a rhenium filament embedded inside an alumina insulator is heated by an electric current. Heat gets transmitted through the alumina and is transferred to metal salt on the source surface. This heat releases ions from the surface by a thermionic emission process [Ble36].

The other ion source present at the TITAN experiment is a plasma ion source. A plasma ion source is made of a low pressure hydrogen gas-filled ceramic container in which a tungsten filament is brought to high temperature via resistive heating. The ions are produced by a DC discharge that occurs between the filament and a cathode. The ions produced are accelerated by the cathode through a hole in the ceramic container and enter the beam transfer system, and eventually gets injected into the Penning trap. The ions produced by the plasma ion source are H^+, H_2^+ and H_3^+. These ions are then used as reference masses for unstable HCI with the $m/q = 1, 2, 3$. It is of importance to use reference ions that probe the same electric and magnetic fields in the Penning trap as the ions of interest. Therefore, same or very close m/q-ratio for the reference ion is desired.

Chapter 4

Summary and outlook

High precision mass measurements of short live isotopes are more than ever of high importance. The motivations stems from the fields of; test of fundamental symmetries, nuclear structure and fundamental nuclear physics but also from nuclear astrophysics and neutrino-physics, as for neutrinoless double beta decay. With the advent of second generation radioactive beam facilities facilities, like ISAC, the access to the short-lived isotopes has been increase tremendously and new mass measurement facilities, adapted to the new requirements of very-short-lived isotopes and increased precision, are needed. The here presented thesis is concerned with the main system for the TITAN mass measurement facility at ISAC, the high precision Penning trap for highly charged ions. In addition two other systematic studies were carried out at existing Penning trap spectrometers, which are described in detail. These two systems are the ISOLTRAP system at CERN, Geneva and the CPT system at Argonne US National Lab, near Chicago.

The thesis gives a broad overview of the motivation for mass measurements and sets the stage for the requirements. The basic principle of exotic beam production is introduced. Mass measurement for radioactive isotopes are explained and particular emphasis is set on the Penning trap system. The TITAN system will be different from all other existing on-line Penning trap spectrometers, in that it employs highly charged ions for the measurement procedure. This leads to a boost in precision proportional to the charge state q of the ions, however introduces systematic differences which are dealt with in this thesis.

Therefore, simulations for the injections and extraction from TITAN's mass measurement Penning trap were made. Injection simulations minimizing the beam diameter entering the trap, were carried out using the magnetic field map of the 4 T superconducting magnet of the Penning trap. Conditions could be identified that will allow an injections of the ions with 100 % efficiency. Comparison of the injection between singly and highly charged ions were carried out and showed satisfactory results.

Simulations to verify the possibility ti use a Lorentz steerer was carried out. This will induce an initial magnetron displacement to the incoming ion bunch and save excitation time inside the Penning trap. It was found that for a 5 keV/q beam, floating the injection electrode structure 4.5 keV above ground reduce the final radial kinetic energy from 80.3 eV down to 4.1 eV for a beam steered by 1 mm. It was also shown that actual extraction electrode structure of the TITAN mass measurement Penning trap is able to reproduce a $^{85}Rb^{+}$ TOF spectra observed at the ISOLTRAP experiment. Finally, the matching between

the 26 mm inner diameter pulsed drift tube placed after the TITAN RFQ and the following 76 mm inner diameter Einzel lens was optimized. The matching is made by a 21 mm long horn at the end of the pulsed drift tube. This matching minimized spherical aberration while keeping small penetration of electric field produced by the Einzel lens inside the pulsed drift tube.

For the studies carried out at ISOLTRAP, CERN, Geneva, a measurement of the correlation between the temperature and the cyclotron frequency of $^{85}Rb^{+}$ in the Penning trap spectrometer have been systematically studied. This has shown that the magnetic field is linearly dependent on the bore temperature of the Penning trap superconducting magnet. A magnetic field drift of $\frac{1}{B}\frac{\partial B}{\partial t} = -2.65(4) \times 10^{-9}$ h^{-1}, a magnetic field-temperature correlation of $\frac{\Delta B}{\Delta T} = 1.26(2) \times 10^{-2}$ G °C^{-1} and a 0.61(2) °C day-night temperature variation have been observed. This has led to the development of a temperature stabilization system, that is now implemented by the group.

Third, a reference laser-ablation ion source that provided stable isotope ions was designed. An overview of the different parts of the ion source was presented. It was shown that the source can efficiently transport the stable ion produced. The ion source is currently under construction. The first ions that would be produced are $^{26}Mg^{+}$, which mass enters in the calculation of the Q-value of a $0^{+} \rightarrow 0^{+}$ super-allowed beta transition which Ft-value is used to compute the V_{ud} element of the CKM matrix.

In conclusion, high precision mass measurements on highly charged ions will be carried out with the TITAN Penning trap system at ISAC/TRIUMF. Systematic investigations for the system and elsewhere were carried out. The TITAN experiment is in an advanced construction phase. Major parts, like the RFQ and the EBIT, exit and have been commissioned. The Penning trap structure has been fully designed, in part based on this thesis, and is presently manufactured. Assembly and commissioning will take place over this summer and the first experiment on short-lived isotopes with the Penning trap are planned for December 2006.

Bibliography

[Ast20] F.W. Aston, Nature, 105, 617 (1920).

[Ber02] I. Bergström *et al.*, Nucl. Inst. Meth. A, 487 (2002).

[Bev92] P. R. Bevington and D. K. Robinson, *Data Reduction and Error Analysis for the Physical Sciences*, Second Edition, WCB McGraw-Hill (1992).

[Bla02] K. Blaum et al., Nucl. Instr. and Meth. B, 204, 478 (2002).

[Bla05a] K. Blaum, *Hochpräzisionsmassenspektrometrie mit Penningfallen und Speincherringen*, Habil. Thesis (in English), Johannes Gutenberg-Universität Mainz (2005).

[Bla05b] K. Blaum *et al.*, J. Phys. G: Nucl. Part. Phys. 31, S1775 (2005).

[Bla05c] K. Blaum *et al.*, Nucl. Phys. A, 752, 317c (2005).

[Bla06] Private Communication 2006.

[Ble36] J.P. Blewitt, Phys. Rev., 50, 464 (1936).

[Blo05] M. Block *et al.*, Eur. Phys. J A 25, s01, 49 (2005).

[Bol90] G. Bollen *et al.*, J. Appl. Phys. 68, 4355 (1990).

[Bol02] G. Bollen, Eur. Phys. J. A, 15, 237 (2002).

[Bol05] G. Bollen, private communication 2005.

[Bra99] M.P. Bradley *et al.*, Phys. Rev. Lett., 83, 4510 (1999).

[Bro86] L. S. Brown and G. Gabrielse, Rev. Mod. Phys. 58, 233 (1986).

[Cab63] N. Cabibbo, Phys. Rev. Lett. 10, 531 (1963).

[Cla05] J. Clark, *Investigating the Astrophysical rp-process through Atomic Mass Measurement*, Ph.D. thesis, University of Manitoba (2005).

[Dah00] D.A. Dahl, Int. J. Mass. Spectr., 3, 200 (2000).

[Dav05] B. Davids and C. N. Davids, Nucl. Instr. and Meth. A, 544, 565 (2005).

[DIN04] DIN IEC 751 - Temperature/Resistance Table for Platinium Sensors, *Lake Shore Cryotronics*.

[Dil01] J. Dilling *et al.*, Hyp. Inter., 132, 495 (2001).

[Dil03] J. Dilling *et al.*, Nucl. Instr. Meth. Phys. Res. B 204, 492 (2003).

[Dom02] M. Dombsky *et al.*, Nucl. Phys. A, 701, 486c (2002).

[Dom06] M. Dombsky, http://www.triumf.ca/people/marik/homepage.html.

[Edd20] A.S. Eddington, Nature, 106, 14 (1920).

[Fri01] T. Fritioff, Hyp. Int., 132, 231 (2001).

[Fuk00] H. Fukutani, *First Measurements of Atomic Masses with the Canadian Penning Trap (CPT) Mass Spectrometer*, M.Sc. thesis, University of Manitoba (2000).

[Gei01] H. Geissel *et al.*, Nucl. Phys. A, 685, 115 (2001).

[Gos95] P.K. Ghosh, *Ion traps*, Oxford University Press (1995).

[Han87] P.G. Hansen and B. Jonson, Europhys. Lett. 4, 409 (1987).

[Hau00] M. Hausmann *et al.*, Nucl. Instr. and Meth. A, 446, 569 (2000).

[Hax49] O. Haxel, Phys. Rev. 75, 1766 (1949).

[Har05] J.C. Hardy and I.S. Towner, Phys. Rev. C, 71, 055501 (2005).

[Her03] F. Herfurth *et al.*, J. Phys. B, 36, 931 (2003).

[Her58] G. Herrmann, J. App. Phys. 29, 127 (1958).

[Hof00] S. Hofmann and G. Münzenberg, Rev. Mod. Phys., 72, 733 (2000).

[Hut03] D.L. Hutcheon *et al.*, Nucl. Instr. and Meth. A, 498, 190 (2003).

[ISA99] *ISAC II - A Project for Higher Energies at ISAC*, TRI-99-01.

[Jok05] A. Jokinen *et al.*, Eur. Phys. J A 25, s01, 27 (2005).

[Kel03] A. Kellerbauer et al., Eur. Phys. J. D, 22, 53 (2003).

[Kes04] O. Kester *et al.*, J. Phys: Conf. Series 2 106 (2004).

[Kin99] M. Kobayashi and K. Maskawa, J. Phys. Soc. Jap. 68, 3763 (1999).

[Klu03] H.-J. Kluge *et al.*, Phys. Scr. T 104, 167 (2003).

[Kob73] M. Kobayashi and K. Maskawa, Prog. Theor. Phys. 49, 652 (1973).

[Kon95] M. König *et al.*, Int. J. Mass Spectr. Ion. Proc., 142, 95 (1995).

[Kug00] E. Kugler, Hyp. Inter., 129, 23 (2000).

[Kur03] H. Kurisu *et al.*, J. of Vac. Sc. and Tech. A, 21, L10 (2003).

[Lal01] A.-S. Lallemand *et al.*, Hyp. Int. 132, 514 (2001).

[Law77] J.D. Lawson, *The Physics of Charged-Particle Beams*, Clarendon Press (1977).

[Lun00] D. Lunney and G. Bollen, Hyp. Int. 129, 249 (2000).

[Lun01] D. Lunney *et al.*, Phys. Rev. C, 64, 054311 (2001).

[Lun03] D. Lunney *et al.*, Rev. Mod. Phys. 75, 1021 (2003).

[Lun05] D. Lunney, Eur. Phys. J A 25, s01, 3 (2005).

[Mai01] M. Maier *et al.*, 132, 521 (2001).

[May49] M. G. Mayer, Phys. Rev. 75, 1969 (1949).

[McL96] D.J. McLaughlin *et al.*, Phys. Rev. A 54, 2040 (1996).

[Pen91] B. M. Penetrante *et al.*, Phys. Rev. A 43, 4873 (1991).

[Pen97] H. Penttilä *et al.*, Nucl. Instr. and Meth. B 126, 213 (1997).

[Pre62] M.A. Preston, *Physics of the nucleus.*, Addison-Wesley Publication Company (1962).

[Rad00] T. Radon *et al.*, Nucl. Phys. A 677, 75 (2000).

[Rin05] R. Ringle *et al.*, Eur. Phys. J. A 25, s01, 59 (2005).

[Rui02] C. Ruiz *et al.*,Phys. Rev. C 65, 042801(R) (2002).

[Ryj05a] V. L. Ryjkov *et al.*, Eur. Phys. J. A 25, s1.53 (2005).

[Ryj05b] Private communication 2005/6.

[Sav91] G. Savard et al., Phys. Lett. A, 158, 247 (1991).

[Sav05a] G. Savard *et al.*, Phys. Rev. Lett. 95, 102501 (2005).

[Sav05b] G. Savard, Eur. Phys. J. A 25, s01, 713 (2005).

[Sav05c] H. Savajols, Eur. Phys. J. A 25, s01, 23 (2005).

[Sch05] P. Schury *et al.*, Eur. Phys. J A 25, s01, 51 (2005).

[Sik05] G. Sikler *et al.*, Eur. Phys. J A 25, s01, 63 (2005).

[Smi05] M. Smith, *A Square-Wave-Driven Radio Quadrupole Cooler and Buncher for TITAN*, M.Sc. Thesis, University of British Columbia (2005).

[Smy50] W. R. Smythe, *Static and Dynamic Electricity*, McGraw-Hill (1950).

[Spe67] J. E. Spencer and H. A. Enge, Nucl. Instr. Meth. 49, 181 (1967).

[Sve03] C. E. Svensson *et al.*, Nucl. Instrum. Meth. Phys. Res. B 204, 660 (2003).

[Vaz06] J. Vaz, private communication 2006.

[Von77] H. Vonach *et al.*, Nucl. Phys. A 278, 189.

[Wol87] H. Wollnik, *Optics of Charged Particles*, Academic Press, Inc. (1987).

Appendix A

Appendix

A.1 Magnetic field map

For a cylindrically symmetric magnetic field, the vector potential is given by [Smy50]:

$$A_\phi(z,r) = \sum_{n=0}^{\infty} \frac{(-1)^n}{n!(n+1)!} \frac{\partial^{2n} B(z,r=0)}{\partial z^{2n}} \left(\frac{r}{2}\right)^{2n+1} \tag{A.1}$$

The rotational of this vector potential gives two magnetic field components:

$$B_z(z,r) = \frac{1}{r}\frac{\partial(rA_\phi)}{\partial r} = B_z(z,0) - \frac{\partial^2 B_z(z,0)}{\partial z^2}\frac{r^2}{4} + \ldots \tag{A.2}$$

$$B_r(z,r) = -\frac{\partial A_\phi}{\partial z} = -\frac{\partial B_z(z,0)}{\partial z}\frac{r}{2} + \frac{\partial B_z^3(z,0)}{\partial z^3}\frac{r^3}{16} + \ldots \tag{A.3}$$

For small values in r, only the first term of each component is important:

$$B_{z1}(z,r) = B_z(z,0) \tag{A.4}$$

$$B_{r1}(z,r) = -\frac{\partial B_z(z,0)}{\partial z}\frac{r}{2} \tag{A.5}$$

The off-axis axial magnetic field $B_z^{gen}(z,r)$ has been generated from the given on-axis field $B_z^{data}(z,r=0)$ using relation (A.4). The correctness of this approximation is verified by calculating the relative contribution of the higher order terms:

$$\text{diff}(B_z) = \frac{B_z^{data}(z,r=5\text{mm}) - B_z^{gen}(z,r=5\text{mm})}{max(B_z^{gen}(z,r=5\text{mm}))} \tag{A.6}$$

Figure A.1 shows that the higher order terms contributes to the axial magnetic field at $r = 5$ mm by at most 0.005 %, which is completely negligible. From (A.6), one see that the off-axis radial magnetic field component $B_r^{gen}(z,r)$ is proportional to the off-axis distance. This component is generated from the given off-axis field data $B_r^{data}(z,r=5mm)$ and using:

$$B_r^{gen}(z,r) = B_r^{data}(z,r=5\text{mm})\frac{r(\text{mm})}{5} \tag{A.7}$$

The contribution of the non-linear terms is verified by calculating the relative difference between the $r = 5$ mm off-axis field generated by equation (A.7) and the given magnetic field $B_r^{data}(z,r=5mm)$:

$$\text{diff}(B_r) = \frac{B_r^{data}(z,r=5\text{mm}) - B_{r1}(z,r=5mm)}{max(B_{r1}(z,r=5\text{mm}))} \tag{A.8}$$

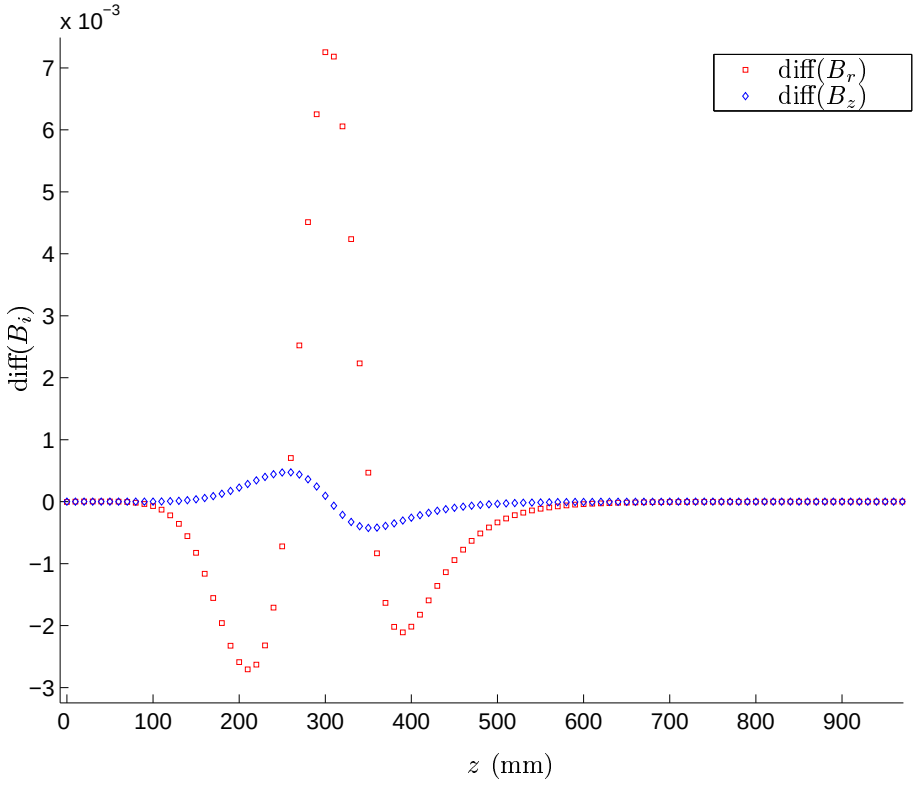

Figure A.1: Variation of the relative contribution diff(Bz) and diff(Br) of the higher order terms in (A.2) and (A.3) as a function of the axial position z.

As shown in Figure A.1, the contribution of the non-linear terms is of the order of 10^{-3} which is negligible. Therefore, the off-axis magnetic field depend only on the first order term of (A.2) and (A.3). The strong magnetic field present for $z < 500$ mm shown in Figure 1.10 puts constrain on the optimal position z_i of the Einzel lens. The particle trajectories in the strong field is mainly determined by the parallel field lines, making the presence of electrostatic focusing devices in that region useless. The next section shows how the focused beam is defined according to the initial variables f, d_i and z_i.

A.2 Beam definition

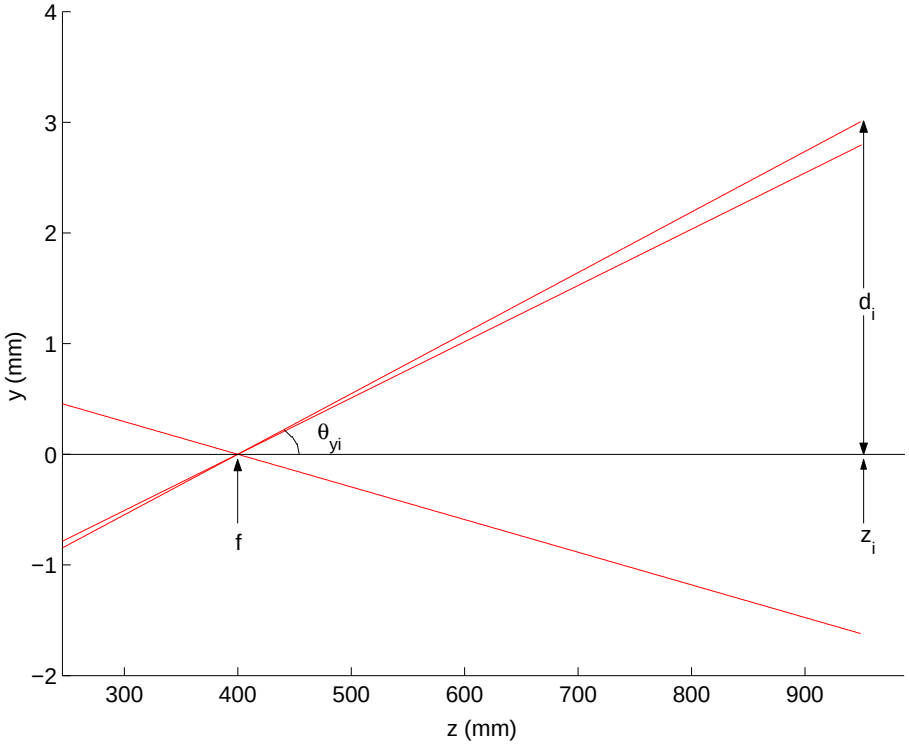

Figure A.2: Definition of the parameters f, z_i and d_i.

Figure A.2 shows how the initial variables f, d_i and z_i variables are defined. f is the distance from the trap center where a null-emittance beam would be focused, z_i is the place where the beam will start being focused by the Einzel lens and d_i is the beam diameter at the position z_i. The beam used for simulations has been generated by the following procedure. The emittance ellipse of a beam

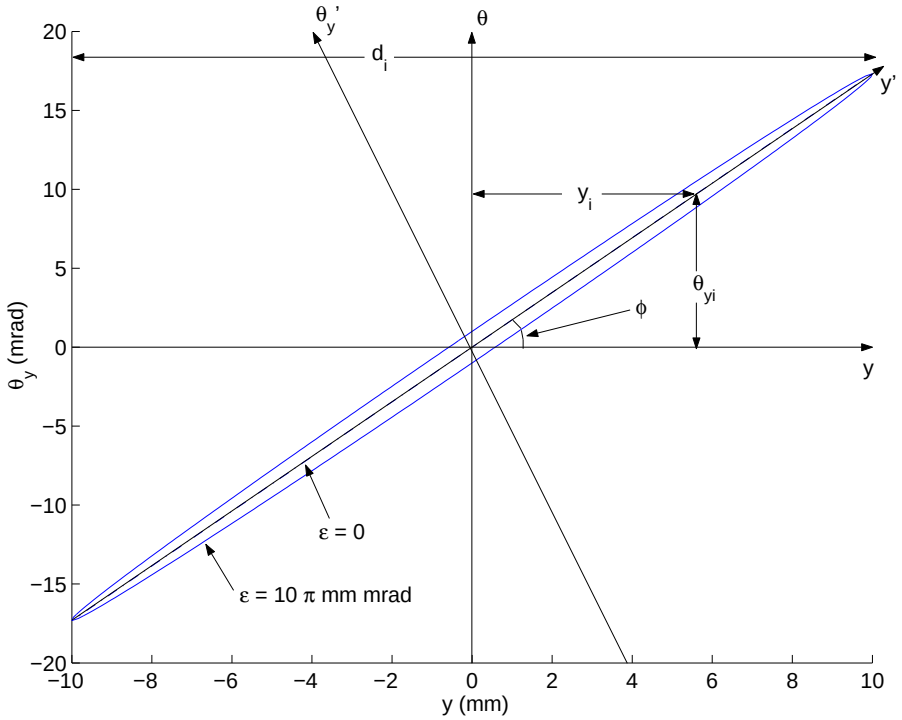

Figure A.3: Emittance plot in y-direction for a 10 π mm mrad beam with initial beam size of 20 mm.

focused by an Einzel lens presents an inclination ϕ with the radial coordinate as shown in Figure A.3. This angle depends on the focusing strength of the Einzel lens. For an ideal beam without any emittance, as shown in Figure A.2, all ions are focused at the same point f. In the phase-space diagram of Figure A.3, such a null-emittance focused beam is represented by a straight line of slope:

$$\tan\phi = \frac{\theta_{y_i}}{y_i}. \tag{A.9}$$

As shown in Figure A.2, the angle θ_{y_i} depends on the three variables f, z_i and d_i:

$$\theta_{y_i} = \arctan\left(\frac{d_i/2}{z_i - f}\right). \tag{A.10}$$

Therefore, from (A.9) and (A.10):

$$\phi = \arctan\left(\frac{\arctan\left(\frac{d_i/2}{z-f}\right)}{d_i/2}\right). \tag{A.11}$$

The radial position (x_i, y_i) and angular divergence $(\theta_{x_i}, \theta_{y_i})$ of the ions was randomly generated using a flat distribution within a circular cross section of diameter d_i and angular emittance $\varepsilon = ab\pi$. The angular emittance is define in the rotated frames (x', θ'_x) and (y', θ'_y). The axis of the ellipse along x' and y' is:

$$a = \frac{d_i/2}{\cos\phi}, \tag{A.12}$$

while its axis along θ'_x and θ'_y is:

$$b = \frac{\varepsilon}{a\pi}. \tag{A.13}$$

The two sets of coordinates (x'_i, θ'_{x_i}) and (y'_i, θ'_{y_i}) are generated within the ellipses:

$$\frac{(x'_i)^2}{a^2} + \frac{(\theta'_{xi})^2}{b^2} = 1 \tag{A.14}$$

$$\frac{(y'_i)^2}{a^2} + \frac{(\theta'_{yi})^2}{b^2} = 1. \tag{A.15}$$

Once rotated back into the (x, θ_x) and (y, θ_y) frames using the rotation matrix:

$$\begin{pmatrix} x_i \\ \theta_{x_i} \end{pmatrix} = \begin{pmatrix} \cos\phi & \sin\phi \\ -\sin\phi & \cos\phi \end{pmatrix} \begin{pmatrix} x'_i \\ \theta'_{x_i} \end{pmatrix}$$

The condition that the ions where generated inside the circular cross section of diameter d_i is verified:

$$x_i^2 + y_i^2 < (d_i^2/2)^2. \tag{A.16}$$

When the ion moves into the strong axial magnetic field region, it undergoes a helical motion of frequency:

$$\omega_c = \frac{qB}{m} \tag{A.17}$$

around the magnetic field lines. To reduce the uncertainty on the final beam size due to the phases of the different ions, the position of the ion's centroid of motion rather then its final position was considered.

The position of the centroid of motion has been calculated according to the wavelength of the helicoidal motion:

$$\lambda = \frac{2\pi}{qB}\sqrt{2mE_z} \tag{A.18}$$

The final position of the centroid of motion is found by taking the average between the final radial position of the ion and its radial position half a pitch before:

$$d_f = 2r_f = r(z=0) + r(z=\lambda/2) \tag{A.19}$$